HIGH-PRECISION WIDE-BANDWIDTH ISOLATED CURRENT MEASUREMENT IN NETWORKED DEVICES

Uroš Platiše

Doctoral Dissertation
Jožef Stefan International Postgraduate School
Ljubljana, Slovenia

Supervisor: Prof. Dr. Mihael Mohorčič, Jožef Stefan Institute, Slovenia

Evaluation Board:
Prof. Dr. Gorazd Kandus, Chair, Jožef Stefan International Postgraduate School, Slovenia
Prof. Dr. Iztok Humar, Member, Faculty of Electrical Engineering, University of Ljubljana, Slovenia
Prof. Dr. Radovan Zentner, Member, Faculty of Electrical Engineering and Computing, University of Zagreb, Croatia

MEDNARODNA PODIPLOMSKA ŠOLA JOŽEFA STEFANA
JOŽEF STEFAN INTERNATIONAL POSTGRADUATE SCHOOL

Uroš Platiše

HIGH-PRECISION WIDE-BANDWIDTH ISOLATED CURRENT MEASUREMENT IN NETWORKED DEVICES

Doctoral Dissertation

NATANČNO ŠIROKOPASOVNO IZOLIRANO MERJENJE TOKA V OMREŽENIH NAPRAVAH

Doktorska disertacija

Supervisor: Prof. Dr. Mihael Mohorčič

Ljubljana, Slovenia, November 2021

To the rebirth of the direct-current distribution grid system,
and future decentralized direct-current peer-to-peer energy.

Acknowledgments

Research and development of new technologies require long-lasting support to overcome all obstacles and reach a mature state of technology and the ability to create products.

I am grateful to all the people and companies that have contributed to my research and development activities in any way on this path: my cheerful and patient mentor Mihael Mohorčič from the Jožef Stefan Institute, Primož Bešter, and Bogo Miklavčič, who were the initiators of the project at Iskra Feriti (now Kolektor), Ludvik Kumar, and Marjan Drmota, who were chiefs for the Research and Development in the Kolektor Group, and Jure Knez from Dewesoft in the product development of the first high current sensors that have already been released to the market.

From the beginning of my research work, I regarded it as a project with the aim to actually develop a new technology. Along with the progress of this project, a great team began to assemble into a new entity, ISOTEL, which directly or indirectly contributed to my research and eventually this thesis. The key and perservering ISOTEL members to whom I am particularly grateful are: Tomaž Kanalec who had already joined at the early stage of the core technology development, Tine Kavčič in developing supporting test software for embedded real-time systems, Gregor Žigon, a highly experienced production CAD designer, and my precious wife, the love of my life, Dreja Novak, who is also a team member and contributed in many ways, in addition to my parents, father Andrej Platiše and mother Branimira Knez Platiše.

Numerous indirect contributors to this thesis are many co-workers from the above mentioned companies as well as open-source communities that have produced great open source tools, such as as Linux/Debian with the corresponding ecosystem, especially the ngspice, yosis, iverilog, gtkwave, python/jupyter, and countless others. Without these great tools, the development would not have been as enjoyable and smooth. Therefore, I was happy to contribute back to the open-source community as part of this thesis by providing an upgrade to the ngspice community, the mixed domain simulation ecosystem.

Abstract

With the increasing use of electricity powered devices and processes in our daily lives, the need for the precise measurement of electrical currents across more than 15 decades from below nA to tens or hundreds of kA has become inevitable both for billing and more optimal energy distribution purposes as well as for the operation and automatization of electrical devices.

A particularly noticeable increase in measurement demand can be observed in direct-current (DC) systems due to the massive deployment of renewable energy sources, such as wind and solar power plants and grid storage systems, and the transition of the automotive industry to electric mobility. Some of these systems may require high-voltage isolation and peak currents in excess of kA. The existing standard compact and lower cost current sensing solutions hardly ever achieve an overall measurement uncertainty below 1%, mainly due to offsets and hysteresis; their typical bandwidth is in the range of 250 kHz, and they may also be noisy.

The main goal of this doctoral dissertation was thus to design and characterize a new method and device for the high-precision wide-bandwidth isolated measurement of direct and alternating electric currents. A particular focus was on achieving key performance parameters, such as high accuracy, precision, sensitivity, wide bandwidth, low noise, and low temperature drift dependency by a simpler construction when compared to the current best state-of-the-art implementations, thus targeting the use of a single gap-less core, low power consumption, and small form factor also suitable for typical networked devices constituting the Internet of Things.

As part of this doctoral dissertation, we first conducted an overview of the widely used methods and principles of current measurement with their corresponding benefits and drawbacks, and developed the necessary models of magnetic circuits for the open-source ngspice simulation environment upgraded into a full co-simulation framework with Verilog and embedded firmware. This knowledge base and research environment were subsequently used to develop, simulate, and verify a new basic element for magnetic circuits with a current controlled variable reluctance (CCVR) used for changing the amplitude or the direction of the magnetic flux and thus making it measurable. This element consisting of a gap-less core and a specific winding combined with the control electronic circuitry constitutes the Platiše Flux Sensor. The new wiring and compact gap-less implementation deliver low offset and hysteresis, a bandwidth in the MHz range, low power consumption, and low noise operation.

Finally, we integrated the novel Platiše Flux Sensor in a functional prototype of a closed-loop zero-flux DC current transducer (CT). This prototype has been thoroughly tested, validated and characterized in a reference setup. We have shown that a 40 A range low current transducer based on the novel method achieved an overall superior performance compared to representative comparable devices based on alternative technologies. More recent research and developments using very high permeability and mechanically stronger materials for core extended such performance up to 2000 A.

Povzetek

Z vse bolj razširjeno uporabo naprav in procesov na električni pogon v našem vsakdanjem življenju je potreba po natančnem merjenju električnih tokov v razponu 15 dekad od nA do deset ali več sto kA neizogibna tako za obračunavanje in optimalnejšo distribucijo energije kot tudi za delovanje in avtomatizacijo električnih naprav.

Povečanje potreb po meritvah je še posebej izrazito pri enosmernih (DC) sistemih zaradi množičnega uvajanja obnovljivih virov energije, kot so vetrne in sončne elektrarne in omrežni shranjevalniki energije, ter zaradi prehoda avtomobilske industrije na električno mobilnost. Nekateri od teh sistemov potrebujejo visoko napetostno izolacijo in vrhnje tokove, ki presegajo kA. Obstoječe standardne, kompaktne in cenejše rešitve za merjenje enosmernih tokov skoraj nikoli ne dosegajo standardne merilne negotovosti pod 1%, predvsem zaradi napak odmika in histerez; njihova pasovna širina je običajno v razponu do 250 kHz, polega tega pa imajo takšni merilniki tudi težave s šumom.

Glavni cilj te doktorske disertacije je bil torej zasnovati in karakterizirati novo metodo za merjenje enosmernih in izmeničnih tokov v širokem frekvenčnem območju. Poseben poudarek je bil na doseganju ključnih parametrov delovanja, kot so visoka natančnost, preciznost, občutljivost, velika pasovna širina, nizka stopnja šuma in majhna temperaturna odvisnost, in sicer s preprostejšo konstrukcijo v primerjavi s trenutno najboljšimi izvedbami. V ta namen smo se osredotočili na uporabo enega samega magnetnega jedra brez zračne reže, z nizko porabo energije in majhnimi končnimi dimenzijami, ki je primeren tudi za omrežne naprave, ki tvorijo internet stvari.

V okviru doktorske disertacije smo najprej opravili pregled splošno uporabljanih metod in principov merjenja toka s pripadajočimi prednostmi in pomanjkljivostmi. Razvili smo potrebne modele magnetnih vezij za odprtokodno simulacijsko okolje ngspice, nadgrajeno z Verilogom in neposredno simulacijo programskih algoritmov, pisanih v programskem jeziku C. Na osnovi tega znanja in izpopolnjenih razvojnih orodij smo najprej zasnovali, simulirali in potrdili nov osnovni element za magnetna vezja s tokovno nadzorovano spremenljivo reluktanco CCVR (*ang. current controlled variable reluctance*), ki se uporablja za spreminjanje amplitude ali smeri magnetnega fluksa in tako omogoča njegovo merjenje. Ta element, sestavljen iz jedra brez zračne reže in posebnega navitja, v kombinaciji s krmilnim elektronskim vezjem, tvori Platišev senzor magnetnega pretoka (*ang. Platiše Flux Sensor*). Nov tip navitij in kompaktna izvedba zagotavljata majhne napake odmika in histerezo, pasovno širino v razponu MHz, nizko porabo energije in nizkošumno delovanje.

Predlagani Platišev senzor magnetnega pretoka smo integrirali v funkcionalni prototip, ki deluje po principu zaprto-zančne ničelne metode merjenja enosmernih tokov. Ta prototip smo nato temeljito preizkusili, potrdili in okarakterizirali v referenčni merilni postavitvi. Pokazali smo, da je nizkotokovni pretvornik z nazivnim dosegom 40 A izdelan na podlagi nove metode v splošnem izkazal boljše delovanje v primerjavi s primerljivimi napravami, ki temeljijo na alternativnih tehnologijah. Takšno delovanje smo z nadaljnjimi raziskavami in razvojem z uporabo visoko permeabilnih in mehansko trdnejših materialov razširili tudi na visoko zmogljive pretvornike z nazivnim dosegom do 2000 A.

Contents

List of Figures

List of Tables

Abbreviations

40A9R	The First Prototype incorporating PFS and ±40 A DC-CT Toroid Core
AC	Alternating Current
AMR	Anisotropic Magneto-Resistance
BFSL	Best fit straight line
BMS	Battery Management System
CCR	Current Controlled Reluctance
CCVR	Current Controlled Variable Reluctance
DAQ	Data Acquisition
DC	Direct-Current
DC/AC	Direct, Constant, and Alternating Current
DC-CT	Direct Current-Current Transducer (Transformer)
EMF	Electro-Magnetic Force
FOCS	Fiber Optic Current Sensor
HVDC	High-Voltage Direct Current, used in power transmission links
IDM	ISOTEL Device Manager
JSI	Jožef Stefan Institute
PFS	Platiše Flux Sensor
RTI	Referred to Input
TEG	Thermo-Electric Generator
SNR	Signal to Noise Ratio
ULP	Eagle CAD Schematics and PCB Software User Language Program

Symbols

H ... magnetic field strength in [A/m]

H_c ... coercivity at which $B = 0$ due to the hysteresis [A/m]

H_m ... dipole momentum magnetic field strength [A/m]

B ... magnetic flux density in [T]

B_s ... saturating flux density of ferrite core [T]

ϕ ... magnetic flux in [Vs]

Θ ... magneto-motive force in Ampere-turns [At]

S ... Sensitivity of Platiše Flux Sensor [V/m]

C ... Cross-talk between L_s and L_m

L_s ... CCVR stimulus windings inductance [H]

L_m ... measuring winding inductance [H]

L_c ... compensation winding inductance [H]

I_s ... CCVR stimulus current [A]

V_m ... voltage induced in the measuring winding L_m [V]

V_p ... residual flux in voltage as demodulated by the Platiše Flux Sensor [V]

U_m ... output of the DC-CT transducer [V]

I_p, I_1 . primary current [A]

I_c, I_2 . compensation or secondary current [A]

ΔI ... difference between the primary and secondary currents referred to input

ζ ... damping factor of a 2^{nd} order system

ω_0 ... resonant frequency of the PI regulator loop [rad/s]

K_p ... proportional part of the PI regulator

K_i ... integral part of the PI regulator [1/s]

N_p ... number of turns of primary winding

N_c ... number of turns of compensation winding

N_m ... number of turns of L_m measurement winding

$M(t)$. modulaton function of the Platiše Flux Sensor

Chapter 1

Introduction

Electric current transfers energy, creates magnetic fields, and when alternating it generates electromagnetic waves, which is the basis for radio communication systems. It is represented by a stream of charged particles Q, measured as a flow of electric charge through a surface dQ/dt, denoted by ampere [A]. The ampere is one of the seven base quantities in the International System of Units (SI) and as such the current measurement represents one of the most elementary and important measurements in the field of electrical engineering.

Electric current can either flow in one direction only and was originally referred to as Direct Current (DC) or the direction can change periodically, which led to this type being referred to as Alternating Current (AC), as known from the poly-phase 50/60 Hz power grid systems. However, the term DC is nowadays used in electrical engineering and in this thesis to represent a constant current, the constant part or the zero frequency component of the frequency spectrum A_0, compared to the original term, which signified one-way direction flow. According to the original meaning, one-way flow i.e., Direct Current, may of course vary over time, however, because the operational changes of devices supplied by DC currents create step responses and switching supplies and because motor controllers contain large amounts of switching frequency harmonics that should be filtered out. Therefore it is commonly referred as DC/AC to explicitly emphasize the existence of other frequency components besides the DC – the constant current. The range of the AC frequency components are expressed by the AC bandwidth.

In the early days of electric power transmission, no active power components existed yet, so AC current offered the only feasible way of transferring energy over long distances by transforming voltages via passive transformers to the AC loads, making it the worldwide standard. Due to the unprecedented progress in semiconductors, electronics, and microcomputers over recent decades, most of the lower power range of modern appliances are more or less supplied by DC currents via AC/DC switching power supplies from power grids. These degrade the power quality [1] of the transmission and distribution of existing power grids with an unwanted DC component and higher frequency components, which need to be monitored, as they reduce the overall power transmission efficiency, as well as the measurement (metering) accuracy [2].

The currents in our living environments typically range from nanoamperes (nA) in various sensors and wearable devices powered directly by batteries, solar-powered, thermoelectric generators (TEG), and other energy harvesting sources, and scale to tens of kiloamperes (kA) in widely deployed railway[1] systems, high-voltage direct-current[2] (HVDC) transmission systems, medical equipment, such as magnetic resonance imaging, research

---

[1] `http://www.wesemann.eu/documenten/nl/Catalogus%20Railway%20Current%20&%20Voltage%20Transducers.pdf`

[2] `https://en.wikipedia.org/wiki/List_of_HVDC_projects`

infrastructure, including particle accelerators (cyclotrons), synchrotrons, and fusion reactors[3], and up to the hundreds of kA needed for instance for the production of aluminium.

The principles of current measurement may be primarily divided into electrically non-isolated and isolated. Electrically isolated current sensors are used from the miliampere (mA) range up to and over kA, while non-isolated sensors are typically deployed in low-voltage and lower current systems rated from femtoamperes (fA) up to several hundreds of amperes of continuous measurement. Different techniques are used for non-isolated sensors to make them suitable for higher voltage measurements.

With respect to the current measurement, this thesis is focused on a new patented invention of an accurate and precise Direct-Current (DC) wide bandwidth (AC) method for isolated current sensing that can be readily used for mass deployments in various application areas, specifically for networked devices, such as the Internet of Things (IoT), renewable energy sources, and smart grids as well as in electric vehicles, industrial deployments, and research infrastructures.

1.1 Motivation and Hypotheses

The demand for accurate DC/AC sensing and metering is constantly growing, particularly in the new application domains of electrical vehicles and renewable energies. However, the market demands a lower-cost and more power-efficient technology that can bring the accuracy and performance currently known only to higher-end equipment to the more affordable lower-cost consumer market, ready for mass deployments, especially in the following emerging areas:

- the automotive industry in hybrid and pure electric vehicles [3], [4];
- smart grids with distributed renewable energy sources and new types of loads requiring precise power quality and consumption monitoring [5], [6];
- efficient DC micro-grids of renewable energy sources [7], [8] with predominantly DC elements and loads [9];
- direct 400V DC energy for more efficient data centers[4] [10];
- peer-to-peer energy distribution, for which the legislation and funding activities have already begun [11] within the Clean energy for all Europeans package[5] for Energy Communities[6], potentially supported with blockchain-based smart contracts[7];
- the increasingly ubiquitous IoT devices [12] in industrial and residential environments with DC current sensing being one of the basic principles for monitoring and controlling a variety of phenomena.

With such a diverse set of potential application areas, current sensors need to meet a number of different operational requirements, all of which formed the motivation for the development of a new accurate and precise DC current transducer method and device for isolated current sensing. The vast majority of affordable DC sensors for mass industrial and consumer use reach a total gain accuracy in the range from 0.5% to 2% and an offset

---

[3] `https://www.iter.org/newsline/-/2978`

[4] `https://blogs.intel.com/wp-content/mt-content/com/research/Direct%20400Vdc%202009-04-27.pdf`

[5] `https://ec.europa.eu/energy/topics/energy-strategy/clean-energy-all-europeans_en`

[6] `https://ec.europa.eu/energy/topics/markets-and-consumers/energy-communities_en`

[7] `https://www.weforum.org/agenda/2021/06/blockchain-can-help-us-beat-climate-change-heres-how`

accuracy from 0.1% to 1% of the full-scale measurement range. This is just barely enough for DC metering in household use.

There are numerous activities and projects in progress [13], [14] that deal with next generation smart grids, micro-grids, energy storage, and initiatives for conscious consumption. One of the key future demands is to enable local peer-to-peer energy exchange and trading to shorten the distance from the local generation to the nearest consumer in order to offload the distribution grids and improve the efficiency of the energy transfer. Emerging technologies, such as blockchain smart contracts, are considered to reward users for being environmentally aware, and novel, more accurate and reliable sensors are needed to support the concept. Namely, AC transmission may contain DC leakages, which are detectable, while a future micro peer-to-peer grid may return to medium voltage (kV) DC transmission as used in solar panels, thus improving the overall efficiency of the system for which accurate and precise DC/AC metering sensors are crucial.

In terms of battery management systems (BMS), accurate metering [15], [16] offers a more precise charge estimation integrated over a longer period of time and consisting of multiple charging and discharging cycles. The higher accuracy improves measurement uncertainty and thus reduces accumulated errors, especially in applications, such as electric vehicles with a designed peak (accelerating) power that is about 5 to 10 times higher compared to steady/continuous power during a normal drive.

High-current sensors are typically surrounded with the heat dissipated mostly from primary current conductors, surrounding electronics, and also from the current sensors themselves (especially from high-current shunts). Temperature rises of several tens of centigrade are normal, therefore the temperature drift of a sensor should be as low as possible.

Wide-bandwidth current measurements are needed due to the higher switching frequencies of contemporary inverters and DC/DC converters. Short reaction times are needed for safety reasons, as well as fast (emerging) pyro-DC fuses that protect the high-power high-voltage DC equipment from short-circuit hazards. Wide bandwidth implicitly calls for low-noise measurements to maximize the signal-to-noise ratio (SNR) over the entire bandwidth. Wide bandwidth and low-noise sensors also offer precise and fast sensorless servo-motor control.

The most accurate isolated high-current DC sensors available on the market today are based on a so-called closed-loop (null-method) flux-gate principle. There are single (magnetic) core implementations, which are bandwidth-limited, a bit noisy, and less accurate, and there are dual and tri-core implementations, which preserve the superb magnetic characteristics of a magnetic core by not introducing any air gap; however, due to their multi-core implementation, they are significantly more complex, costly, bulky, and consumptive.

The main challenge of this thesis was thus to design and characterize a new method and device for sensing direct and alternating electric currents with performances comparable to the currently known state-of-the-art closed-loop dual and tri-core flux-gate implementations. The key parameters include high accuracy, precision, sensitivity, wide bandwidth, and low temperature drift dependency; however, our aim was a simpler construction reduced to a single gapless core, lower power consumption, and reduced form factor. The new method also needed to be less noisy, as this is a prerequisite for a wide-bandwidth operation. The main hypotheses investigated in this doctoral dissertation were as follows:

H1 Based on a novel winding, it is possible to design a new kind of magnetic flux sensing principle that is integrated into a gapless magnetic circuit with the aim to preserve the original properties of a magnetic material.

H2 It is furthermore possible to develop a new zero-flux current sensing method, such that the resulting device for the isolated measurement of direct and alternating electric currents exhibits superior sensitivity and accuracy and low noise in the wide bandwidth and large measurement ranges.

1.2 Methodology

The proposed research started with a thorough analysis of related research work and practical solutions. This analytical work was followed by a theoretical design of windings that created a novel magnetic flux sensor for a DC/AC wide-bandwidth current measurement principle.

The theoretical work was based on the non-linear simplified properties of magnetic materials and non-homogeneous magnetic fields, a combination of modeling, computer simulations, and verification within the ngspice and FEMM simulation environments. In the first step, a proof-of-concept simulation was carried out, followed in the next step by the development of an open source ngspice simulation environment able to integrate a mixed signal domain simulation by including Verilog and C/C++ code as part of a complete system simulation.

The verified principle of operation was then implemented in a functional prototype device comprised of a ferrite core material and low-cost programmable logic with a micro-controller. The experimental evaluation included test benches for core and magnetic flux sensor verification as well as higher DC/AC current measurement verification. To ease the testing of the prototype device, we also developed a dedicated software test framework that interacts with the micro-controllers firmware in real-time.

1.3 Contributions

The key original contribution of this dissertation is the new patented [17] method for magnetic flux measurements inside a closed gapless core, named the Platiše Flux Sensor (PFS) after the inventor. The PFS was achieved with a novel concept of windings on a magnetic core, introducing a current-controlled variable reluctance (CCVR) functionality. CCVR acts as an active element (i.e., a transistor) inside the magnetic material capable of altering the paths of a magnetic flux. With the novel sensing winding, the flux changes can be captured, which can extract, along with the PFS modulation/demodulation scheme, the DC and AC amplitudes of the flux inside a magnetic core.

Using the PFS and the closed-loop (null) method, the device for the isolated measurement of electric currents has been demonstrated to perform with high sensitivity, accuracy, low noise, and wide bandwidth operation. It is targeted for use in emerging applications, such as renewable energy sources, electric vehicles, and Internet of Things (IoT) networked devices. The performance evaluation has shown that the new method delivers a single core solution, which outperforms the performances of single core flux-gate solutions and is comparable to the highest performance dual- and tri-core complex solutions, while overcoming some of their drawbacks.

In this dissertation, we achieved four main and two additional original scientific contributions. The main scientific contributions are:

C1 The theoretical design of a novel winding that forms current-controlled variable reluctance (CCVR) in a magnetic circuit.

C2 A novel zero-flux current sensing method based on CCVR.

C3 The practical design and implementation of a current sensing device for the isolated measurement of currents suitable for emerging IoT applications.

C4 A detailed performance analysis, characterization, and validation of the new method and device for the isolated measurement of electric currents in a representative testing environment.

Additional contributions important for the research field include:

C5 A comprehensive model of magnetic circuits and supporting electronics for simulation and validation in the ngspice simulation environment.

C6 A new open-source mixed signal domain simulation environment including Verilog and C/C++ code.

1.4 Organization of the Dissertation

This dissertation is logically structured into six main chapters. Following the Introduction, Chapter 2 provides a brief overview of some of the most popular current sensing methods and their main drawbacks, which motivated the research work presented in this thesis.

Chapter 3 describes the simulation and verification environment purposely developed by introducing a new xspice code model for a fast, simplified, non-linear ferrite core model and a new xspice code model for the simple integration of the actual firmware code for system simulation within the ngspice.

Chapter 4 introduces the basic concept and principle of operation of the key contribution, the Platiše Flux Sensor. This is followed by a description of a complete closed-loop (null method) zero-flux Direct Current-Current Transducer (DC-CT) in Chapter 5, as well as the details on its validation, testing, and performance evaluation of the new Platiše Flux Sensor in comparison with other technologies.

Finally, the Conclusions and the outlook of the thesis are drawn in Chapter 6.

Chapter 2

Overview of Current Measurements

Electric current is measured in amperes, named after French mathematician and physicist André-Marie Ampère, who was inspired by the magnetism discovered by Danish physicist Hans Christian Ørsted in 1820. Ørsted discovered that a current in a wire produces a magnetic field. Ampère further determined that if two wires are placed parallel to each other and a current is passed through them, the wires will either be attracted to or repelled by each other, depending on whether the currents flow in the same or opposite directions.

Until 2019, the SI definition followed this arrangement. If an experiment were to be set up under ideal conditions with two infinitely long straight wires exactly 1 meter apart, a current of 1 ampere would result in a force between the wires of $2 \cdot 10^{-7}$ newtons (N) per meter of length. On the 20^{th} May 2019, the 144^{th} anniversary of the Metre Convention, four of the seven SI base units – the kilogram, ampere, kelvin, and mole – were redefined by setting exact numerical values when expressed in SI units for the Planck constant (h), the elementary electric charge (e), the Boltzmann constant (k_B), and the Avogadro constant (N_A), respectively. Hence, the ampere has been redefined by taking the fixed numerical value of the elementary charge e to be $1.602176634 \cdot 10^{-19}$ when expressed in coulombs (A·s), where one coulomb is equal to about $6.241 \cdot 10^{18}$ electric charges (e). The ampere is thereby a measure of the amount of electric charge in motion per unit time, i.e., one ampere denotes the electric current in which one coulomb of charge travels across a given point in 1 second.

The first measuring devices for electrical current were galvanometers, which were based on the principle introduced by Ampère and developed by French physicist-physician Jacques-Arsène d'Arsonval in 1882. These devices consisted of a coil wrapped around an iron core, mounted between the poles of a permanent magnet. The current under measurement passed through the coil, creating a magnetic field opposing the magnetic field of the permanent magnet. The coil with the iron turned proportionally to the magnetic strength generated from the coil, which was further proportional to the DC current passing through the coil.

In 1827, German Georg Simon Ohm discovered the relationship between voltage and current in a conductor; paired with the Wheatstone bridge and numerous improvements, galvanometers were able to measure voltages and resistances accurately by 1888. The galvanometer had a typical range up to 100 μA for a full scale. A resistor, nowadays called a shunt (a low ohmic resistor used to measure current), was used to bypass the majority of the current to extend the range. The technology evolved over time, but shunts continue to be the most commonly used elements for measuring electric currents. Shunts are electrically coupled with the primary current, therefore such measurements are referred to as electrically non-isolated measurements.

An early AC transformer was built by English-Italian Sebastian Ziani de Ferranti around 1880–1882, and a closed-core design was suggested by Hungarian Ottó Bláthy, inventor of the induction electricity meter and co-inventor of the transformer who, along with Károly Zipernowsky and Miksa Déri, demonstrated the first such transformer in 1884. The first metal rectifiers (copper oxide or selenium oxide) enabled the measurement of the AC voltages and currents. The use of current transformers and a shunt (also called a burden resistor) on the secondary side also enabled higher currents to be measured.

Around 1912, German physicist Walter Rogowski proposed a so-called air-coil suitable only for measurements of AC currents. The current transformer and the special design of the air-coil by Rogowski indirectly measure currents through induction, therefore they represent an electrically isolated measurement. Nevertheless, they can only measure AC currents.

As early as in 1879, Edwin Hall discovered that when a conductor with a current flowing in one direction was introduced perpendicular to a magnetic field, a voltage could be measured perpendicular to the current path, which represents the basic principle of Hall sensors. The first useful Hall sensors of magnetic fields were introduced after the development of indium arsenide semiconductor technology in 1950, and larger deployments of such sensors started in the 1960s.

In 1856, William Thomson (aka Lord Kelvin) discovered the anisotropic magnetoresistance (AMR) effect. By using pieces of iron, he discovered that resistance increases when the current is in the same direction as the magnetic force and decreases when the current is at 90° to the magnetic force. Much later, only in 2007, Albert Fert and Peter Grünberg discovered the giant magnetoresistance principle, which offered an alternative technology to Hall sensors. With this principle, the current is measured indirectly via the induction of a magnetic field, meaning that such measurements are also electrically isolated and can be used to measure DC and AC currents.

In 1936, the fluxgate magnetometer was invented by Hans Aschenbrenner and Georg Goubau. It initially served as a detection device for submarines, however the principle of operation was adopted by so-called fluxgate transducers. The measurement method relies on the non-linear saturating characteristics of ferromagnetic materials. Like AC transformers, they use the core and are isolated from the primary current. With the help of electronics circuitry, fluxgate sensors are able to measure DC and AC in wide bandwidth. High-end implementations of fluxgate sensors represent the most accurate DC/AC current measurement devices on the market today.

Recent research and developments for very high voltage and very high DC/AC currents include fiber optic current sensors (FOCS), which utilize the magneto-optic, i.e., Faraday effect of the fiber. A polarized light is transmitted to a fiber and, with the presence of a magnetic field, this changes its polarization angle.

In addition to these key principles of current measurement, the MOSFET semiconductors technology is also worth mentioning, which offers the electrically non-isolated measurement of currents directly on transistors themselves using a method called a ratio-metric measurement. Higher power MOSFETs are composed of a number of parallel transistor cells. A parallel transistor cell called a sense transistor is used to mirror and scale-down the current, which is nearly proportional to the main current flow through the rest of the transistor cells. The mirrored and reduced current is then easily measurable. An alternative is to measure a voltage drop on the drain-source resistance (R_{DS}), however, due to the very large temperature dependency of the R_{DS}, such measurements are only useful for the detection of over-currents.

The current sensing principles briefly described above may be grouped into non-isolated and isolated methods, and also according to DC/AC capabilities as follows:

- Non-isolated DC/AC:

  - Shunt, and
  - MOSFET.

- Isolated AC only:
  - Current Transformer, and
  - Rogowski coil.
- Isolated DC/AC:
  - Hall,
  - Magneto-Resistance (AMR),
  - Fluxgate, and
  - Fiber Optic Current Sensors (FOCS).

The basic concepts for each of the above listed methods are described in more detail in the following subchapters.

2.1 Shunt

Initially, shunts were used to expand the range of an ampere meter placed in parallel with a coil with a typical full-scale current of about 100 μA. The term shunt stands for diverting or bypassing a current away from the primary circuit. Nowadays, with the electronic, voltage-sensed, current sensors, shunts are placed in series.

A shunt is in general a low-ohmic resistor with low temperature drifts that is also capable of withstanding higher stresses without being damaged. It can be described as:

$$V(i,T) = i \cdot R_{25}\big(1 + \sum TC_i \Delta T^i + \Delta(i, V, RH, t, g)\big) + L\frac{di}{dt} + V_{EMF}\Delta T \tag{2.1}$$

A voltage drop as per Eq. (2.1) on a shunt with a nominal resistance R_{25}, which is typically given at a nominal ambient temperature of around 25 °C, is affected mainly by the self-heating effects. Even though the resistance of a shunt is typically very low, the total losses can easily exceed over 50 W of power dissipation. The temperature stability is denoted by the TC_i vs. the temperature changes ΔT. The long-term stability of the resistance is also affected by various stresses, such as (peak) currents i, voltage V, humidity RH, aging t, and mechanical stresses g. Then, there is the undesired noticeable inductance L, which may at very low resistances R_{25} limit the bandwidth to as low as 10 kHz (R/L). The last, often neglected, but very important part is the thermal electromotive force (EMF) V_{EMF} reflected as an offset error.

Higher current resistors are typically in the range of around 50 $\mu\Omega$[1], with the resistance translating to 50 μV per one ampere. Such accurate and stable resistors with a low temperature drift are costly and they require space for cooling. Measuring low voltage drops requires amplification, provided by difference operational-amplifiers or instrumentation amplifiers, which add to (worsen) the total offset, noise, and gain accuracy of the overall measurement. In addition, very low voltages are more susceptible to external electromagnetic interference. The R/L constant together with the amplifiers also determines the overall AC bandwidth.

Shunt measurements are not electrically isolated and require additional electronics components to implement a transformer or opto-isolation, making the overall system solution

---

[1] `http://www.ohm-labs.com/precision-shunts/high-current-shunt.html`

more complex, bigger, and thus less suitable for higher voltages and powers, especially in in the fields of power generation and distribution grid applications and e-mobility. Therefore, shunts are preferably used as burden resistors [18] on the secondary, mirrored side of some other (isolated) principle that is capable of scaling down the higher primary current to a secondary low-current side. Shunts are used in such a manner in all of the methods described in the following subchapters.

2.2 MOSFET Ratio-Metric

A MOSFET consists of numerous (thousands) matched parallel transistor cells [19], [20] that reduce the common drain-source resistance, R_{DS}. Several cells out of many are connected to a separate measurement source called a sense or a mirror (pin). When the MOSFET is turned on, the current through the MOSFET splits inversely with respect to the two resistances in ratio-proportional way. Schematically, this looks like two parallel MOSFETs with a common gate and drain connections as shown in Figure 2.1.

The ratio of the source current to the load current is specified by the Current Mirror Ratio n:

$$I_{mirror} = I_{load}/n \tag{2.2}$$

and is typically around 1:1000, under the condition that both the source and the mirror are held at the same potential. The current is effectively distributed according to the resistances of the mirror source R_M and R_{SENSE}, the main current source R_S, and a bulk drain resistance common to the entire device denoted as R_D.

If the mirror pin is disconnected ($R_{SENSE} \to \infty$), the maximum output voltage that can appear at the mirror terminal is:

$$V_{mirror} = V_{DS}\frac{R_S}{R_S + R_D} = K_{MC} \tag{2.3}$$

Eq. (2.3) defines a so-called mirror compliance ratio K_{MC}, which is used to calculate $R_D = R_{DS} - R_S$. R_M is obtained by multiplying the R_S by the mirror ratio n. Knowing all these internal resistances and the external R_{SENSE}, the currents can be calculated using the usual resistor divider equations and the total V_{DS} drop caused by the current I_{load}.

When a resistor is placed between the mirror pin and the main source pin R_{SENSE}, then all of the primary load current I_{load} that flows through the drain effectively returns to the same source. In this way, the current measurement through the mirror pin introduces virtually no measurement losses. If low value resistances are used, the Current Mirror Ratio is more or less unaffected, however introducing a current sense resistor with a larger resistance effectively changes the total mirror resistance and thus alters the Current Mirror Ratio of Eq. (2.2).

The typical accuracy of the MOSFET ratio-metric method is around 5% and the mirroring current exhibits the same (very fast) response times as the main source, making this method suitable for per cycle current monitoring, limiting, and short circuit protection in switching applications.

This method is not meant for sensing any other primary currents than that of the switching devices themselves, however since current transducers are used to sense the (high) currents of such switching devices, this method provides the lowest cost and the lowest power replacement for applications in which higher accuracy is not needed.

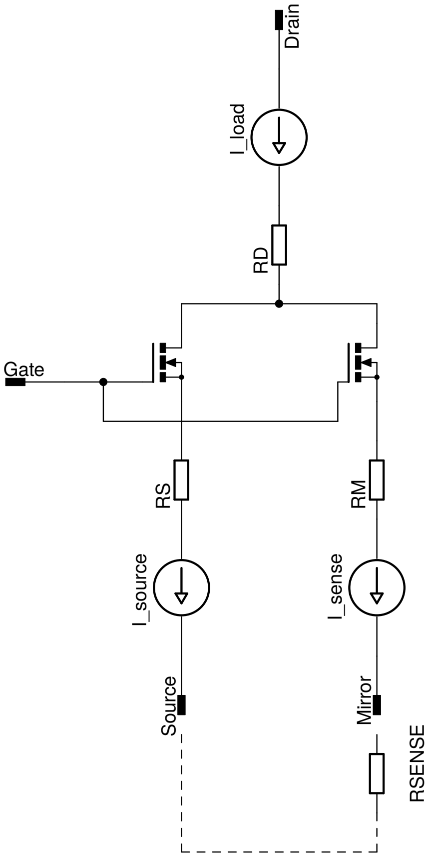

Figure 2.1: Ratio-metric MOSFET equivalent model.

2.3 Current Transformer

Current Transformers (CT) [21] are instruments similar to AC transformers of typically one primary turn and N secondary turns wound on a ferromagnetic core. Based on the induction principle, the primary current induces voltage in the secondary winding, terminated by a burden resistor R_B. The secondary winding therefore forms a closed circuit with a secondary current scaled down for a factor $1/N$ of the primary current.

A simplified equivalent model of a transformer referred to the secondary winding is shown in Figure 2.2, where I_p is the primary current, the I_s secondary current equal to I_p/N, Z'_m is the reflected core impedance, Z_s is the secondary core impedance, and R_B is the burden resistor.

The accuracy of CTs is affected by the magnetizing current, resulting in a secondary winding amplitude drop (i.e., error) as well as phase errors. The frequency response is further affected by leakage inductance Z_s, burden resistance R_B, and the core Z'_m, which together narrow the bandwidth of the transformer [22], [23]. At larger amplitudes, the transformer core, i.e. the ferromagnetic material approaches saturation limits which, besides the winding resistance, limits the maximum range of a current transformer.

To increase the range, improve accuracy, and extend the frequency response down to several tens of Hz, the winding resistance and burden resistor R_B should be as low ohmic as possible. A possible improvement for a current transformer with lower secondary currents is to use an operational amplifier (OPAMP) as a trans-impedance amplifier. Such an arrangement, also called a quasi zero-flux transformer, effectively reduces the burden resistance R_B down to zero, as shown in Figure 2.3.

The output voltage is proportional to the current, amplified by the feedback resistor R_F as per:

$$U_{Ip} = R_F I_p/N \tag{2.4}$$

Besides the listed advantages, this circuit also yields higher measurement sensitivity.

Back in the 1960s, H.G. Hereward already proposed another approach of an active flux compensation technique to further reduce the flux in the core down to zero. As shown in Figure 2.4, the concept proposed an additional compensation winding driven by the amplifier with an amplitude proportional to the sensed current, i.e. operating as a P-regulator. Under balanced conditions, the current in the compensation winding is a perfect mirror of the primary current, reducing the magnetizing current down to zero. This principle is also called the zero-flux principle and represents the basic concept of modern closed-loop DC-CTs.

The magnetizing current represents the largest contributor to the errors, however, the flatness of the frequency response is also affected by the stray capacitance of the compensation winding, which may also be compensated with an active circuitry [24]. Current transformers may therefore be used to measure kA and over hundreds of MHz[2].

---

[2] `https://www.magnelab.com/products/ac-current-transformer-broad-frequency-response-hfct/`

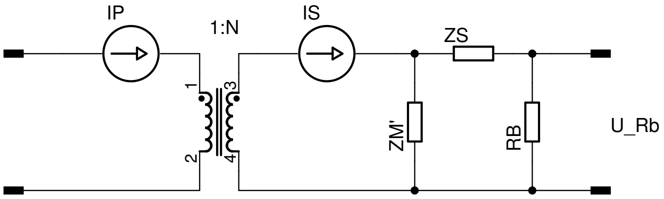

Figure 2.2: Simplified model of a current transformer.

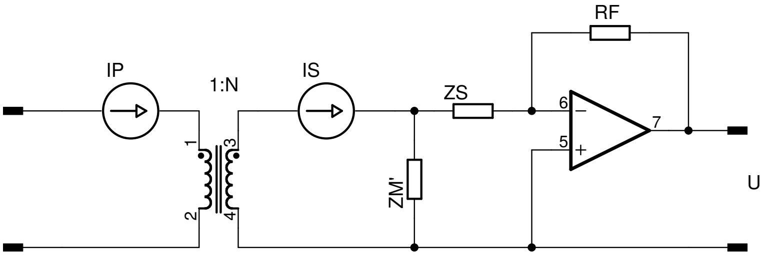

Figure 2.3: Improved frequency response and accuracy with quasi zero-ohm R_B.

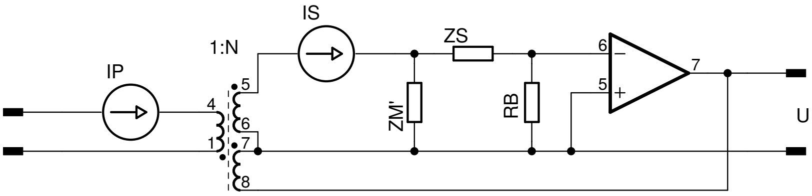

Figure 2.4: Hereward active zero-flux transformer.

2.4 Rogowski Coil

A Rogowski coil [25] as shown in Figure 2.5, named after Walter Rogowski, is an air coil suitable for measuring very wide bandwidth AC currents, from a hertz (Hz) to over 20 MHz. Originally made as helical and toroid coils, they are wrapped around the primary conductor whose current is to be measured. The most recent implementations include PCB planar coils used for measuring high-speed transients in switching applications directly around Insulated Gate Bipolar Transistors (IGBT) and Silicon Carbide (SiC) MOSFETs [26].

Rogowski coils are implemented as flexible or rigid coils and have numerous advantages over the CT in the AC domain. Without the need for a ferromagnetic core, they feature zero-hysteresis, no saturation, no "core" losses, and are safer to use in high-voltage high current systems, as the air coil does not accumulate energy that would be discharged with a sudden disconnection. Therefore, they represent very linear measurement devices capable of measuring currents up to and over 100 kA at an achievable uncalibrated accuracy of around below 0.5%[3], while the typical calibrated accuracy class is between 0.1% and 0.5%. High performance coils can even meet the accuracy class 0.1% suitable for metering and protective relaying in power grid systems.

The principle of operation relies on Faraday's induction law, according to which the total electromagnetic force (EMF) that is induced in a closed circuit is proportional to the change of the total magnetic flux in time:

$$v(t) = -\frac{AN\mu_0}{l}\frac{dI(t)}{dt} \tag{2.5}$$

where A is the area of one turn of the Rogowski coil, N is the number of turns of the Rogowski coil, l is the length of the winding (ring), and $\frac{dI(t)}{dt}$ is the current change in time. The current is obtained by integrating the output of the coil with a lossy integrator.

DC currents can be measured by physically moving the Rogowski coil over a constant magnetic (DC current) field. In the scope of this thesis, the Rogowski coil is not a direct competitor to the newly presented principle of operation, but due to our interest in high bandwidth DC-CT, it is suitable for the bandwidth verification of very high currents.

---

[3] `https://www.ti.com/lit/ug/tidubv4a/tidubv4a.pdf`

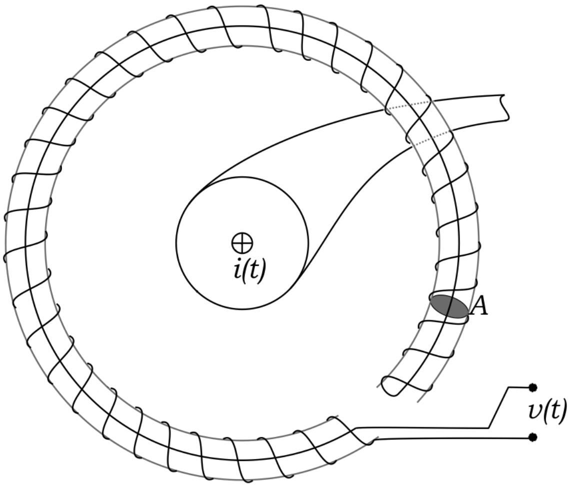

Figure 2.5: Rogowski coil.

2.5 Hall Sensor

The Hall effect sensor [27] is based on a principle of deflecting the charge carriers in a strip under the presence of a magnetic field, caused by the primary current to be measured, which is perpendicular to the direction of the charge carriers – bias electric current of the sensor. The more electron mobility a material has, the higher the sensitivity. Examples of such a suitable material are gallium arsenide (GaAs), indium antimonide (InSb), indium arsenide (InAs), and the latest material of interest, graphene.

The deflected carriers produce a voltage difference measured between the two sides of a strip. The voltage difference is proportional to the cross product of current I and magnetic field strength B, as shown in Figure 2.6, and largely influenced by the temperature:

$$V(I,B,T) = S(I,B) \cdot B + \beta \Delta T \pm V_{off} \tag{2.6}$$

The sensitivity $S(I,B)$ of the sensors (without a pre-amplifier) varies from a few mV to 100 mV per one tesla and is linear in the limited range of a magnetic field B. The higher the sensitivity, the higher the temperature instability β, which typically ranges from 50 ppm/K to 1000 ppm/K[4], and equivalently the offset voltage V_{off} in the range from 1 to

---

[4] `https://www.lakeshore.com/products/categories/magnetic-products/hall-(magnetic)-sensors`

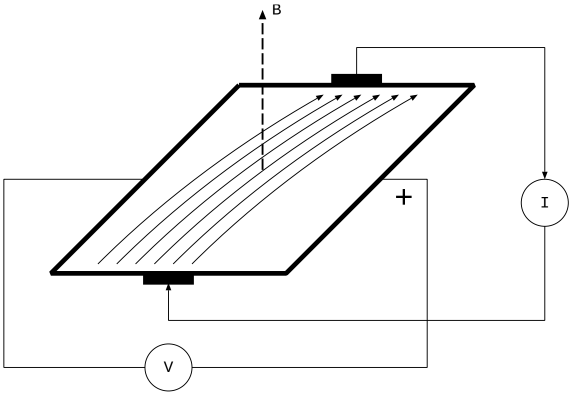

Figure 2.6: Principle of a Hall sensor.

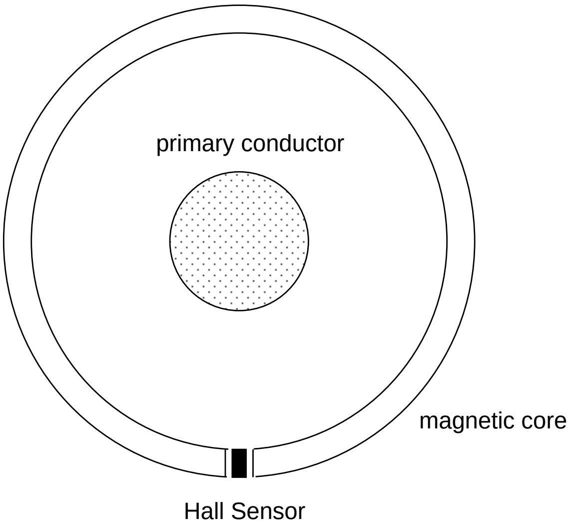

Figure 2.7: Open-loop Hall sensor with a soft magnetic core and a primary conductor of a single turn.

10 mT. The typical bandwidth of Hall sensors is between 10 and 100 kHz.

2.5.1 DC/AC Current Measurement Applications

In DC/AC current measurement applications, Hall sensors are typically used in two arrangements:

1. Open-air, in which a current passes by one Hall sensor or two Hall sensors operating in differential mode [28]. This method is typically used for higher currents above 100 A.

2. Using a soft magnetic material with an air-gap into which a Hall sensor is placed. This method is suitable in a wider range of applications from several A up to kA and offers higher sensitivity due to the gain of the magnetic circuitry [29].

The first method is largely used in bus sensing and inverter switching applications, whenever there is a need for a compact and low-power solution. To improve the accuracy of the Hall output voltage $V(I, B, T)$, modern integrated sensors feature temperature compensation, which is the primary source of error. Using two sensors in differential manner greatly improves rejection to external (disturbances) magnetic fields. Such systems typically reach an accuracy of about $\pm 2.5\%$.

The performance of Hall sensors is further greatly improved by using soft-magnetic cores, which work as magnetic amplifiers, with an air-gap into which a Hall sensor is placed, as shown in Figure 2.7. The magnetic amplification and correlating sensitivity largely depend on the air-gap length. The final soft-core permeability resulting in a so-called effective permeability μ_e is:

$$\mu_e = \frac{\mu_r}{1 + \mu_r \cdot l_g / l_e} \tag{2.7}$$

A typical sensor with an air-gap of $l_g = 1$ mm, sufficiently large to insert a Hall sensor, an effective length of $l_e = 1$ dm, and a relative permeability of $\mu_r = 5000$ yields an effective relative permeability (amplification) of around 98. The air-gap is relatively large, which means a significantly increased magnetic core permeability, i.e., to $\mu_r = 50$ k, increases

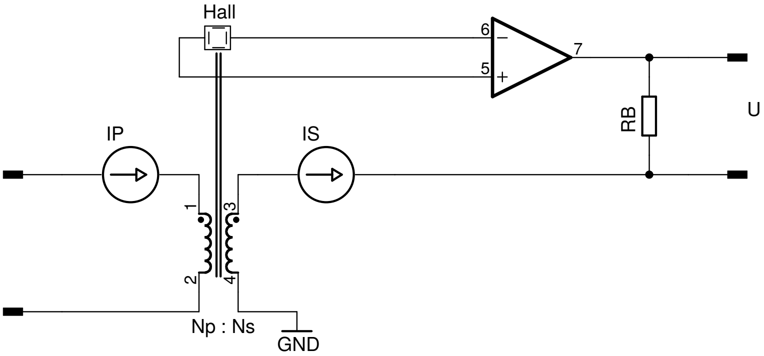

Figure 2.8: Closed loop Hall-based current sensor.

the relative effective permeability μ_e by a negligible amount, only to about 100. Since soft-magnetic materials themselves add an additional offset and hysteresis errors, besides the mentioned contribution from Hall sensors, the preferred way to increase sensitivity and consequently reduce the magnetic offsets and hysteresis anomalies of the soft-core material is therefore to reduce the air-gap length l_g to the minimum possible. The other option is to increase the number of primary turns N_p.

To compensate for the large temperature dependency, the non-linearity of the Hall sensor and the soft magnetic cores, and to further extend the measurement range of such a current transducer, the Hall sensor can be placed in a closed-loop configuration. This principle was already introduced by H.G. Hereward (see Chapter 2.3) and is shown in Figure 2.8. In such a zero-flux configuration, a Hall sensor serves as a flux null detector, driving a feedback OPAMP (operating as PI regulator). The feedback OPAMP drives back the secondary winding of N_s turns with the current equal to $-I_p\frac{N_p}{N_s}$, whose current is sensed on a burden resistor R_B. The non-linearities are mostly compensated and the main sources of errors that remain are:

- the offset of the Hall sensor,
- the offset of the magnetic circuit with hysteresis,
- conductor position error, and
- non-linearity arising from the non-homogeneous magnetic field distribution and non-homogeneous materials in the system.

The total accuracy of such a sensor is about 1% within the industrial temperature range [30] with the magnetic material continuing to be the main contributor to the total error, however, this is mostly due to the reduced effective permeability introduced by the air-gap. The secondary compensation winding notably also provides a direct AC path, thus extending the AC bandwidth to at least 250 kHz and higher at small signal amplitudes. A high performance implementation may use an additional winding for the AC path, separated from the compensation winding, with less turns to reduce the leakage inductance. A similar concept of combining the best of the Hall and CT is shown in [31].

2.6 Magnetoresistance Sensor

Alongside the Hall effect, the development of magnetic sensors evolved further with Anisotropic Magnetoresistance (AMR), Giant Magnetoresistance (GMR), and the latest similar tech-

Table 2.1: Comparison of Magnetoresistance vs. Hall Technologies.

Technology	**Hall Effect**	**AMR**	**GMR**	**TMR**	**Unit**
Power Consumption	5..20	1..10	1..10	0.001 .. 0.01	mA
Die Size	1 x 1	1 x 1	1 x 2	0.5 x 0.5	mm^2
Sensitivity	≈ 0.5	≈ 1	≈ 3	≈ 100	mV/V/mT
Noise Level	>10	0.1 .. 10	1 .. 10	0.1 .. 10	$nT/\sqrt{Hz}$
Dynamic Range	≈ 1000	≈ 1	≈ 10	≈ 100	mT
Temperature Range	<150	<150	<150	<200	°C

nology that was initially described by the GMR theory called Magnetic Tunnel Junctions (MTJ) or Tunnel Magnetoresistance (TMR) structures [32].

Magnetoresistance (MR) sensors are based on resistance changes according to the angle between the directions of the magnetization of adjacent magnetic layers due to an external magnetic field. There are two types of material in which a GMR effect can occur: granular systems and discontinuous multi-layer materials. A multi-layer material consisting of two layers of an Fe-Co-Ni alloy, such as permalloy, separated by a non-magnetic conductive layer, changes the angle of parallel magnetization to anti-parallel alignments under the magnetic field exposure, effectively reducing the free path of electrons between the upper and lower layer of the magnetic material, which can be observed as a change in resistance $\Delta R/R$. As the change of resistance cannot detect the direction of an external magnetic field, the output is considered as unipolar. A solution to that is to bias the sensor and thus to virtually convert it to a bipolar output.

Recent TMR structures are composed of a multi-layer film material and exhibit a greater change in resistance compared to AMR and GMR. GMR is typically arranged in a Wheatstone bridge to compensate for the high temperature dependency. Compared to the Hall sensor, GMRs have a higher sensitivity, a much wider frequency range, a smaller size, and lower power consumption. The TMR structures, relative to GMR, have a better temperature stability, an even higher sensitivity, and a wider linear range. In addition to the fact that GMR production is more costly compared to CMOS integrated Hall sensors together with OPAMPs, GMR also features non-linearity, a lower range, a noticeable hysteresis, and unipolar output, which requires biasing to convert the sensor to a bipolar output. A comparison of different MR technologies is outlined in Table 2.1. Even though the TMR sensitivity is very high, when used in a closed loop arrangement with a soft-magnetic core, it still requires an air-gap into which a sensor is placed, thus reducing the overall performance of the current sensor.

2.7 Fluxgate - Saturating Core

Although initially developed for submarine detection and magnetic compasses, fluxgate [33] still represents the most widely spread principle for accurate DC/AC current measurements on the market. The concept is based on the non-linear, saturating property of soft ferromagnetic materials used as a sensor element and the use of zero-flux feedback compensation as already introduced by H.G. Hereward (see Chapter 2.3) to compensate for the non-linearity, the temperature dependency, and to extend the measurement range. The principle of operation is straight-forward and involves exposing a magnetic material to some external magnetic field H_e caused by a primary winding of one turn and a current I_p. To reach the saturation point to the maximum $H_{max} = H_e + H_{xp}$, an additional excitation into positive direction is needed H_{xp}, whereas to reach the minimum saturation point $H_{min} = H_e + H_{xn}$, an additional excitation into negative direction is needed H_{xn}.

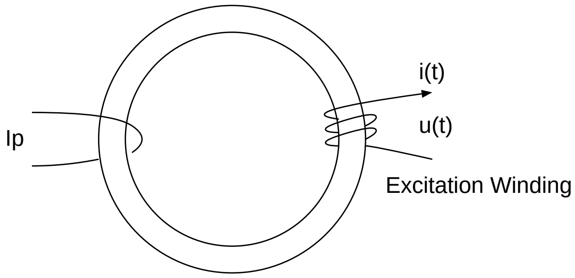

(**a**) Fluxgate Core.

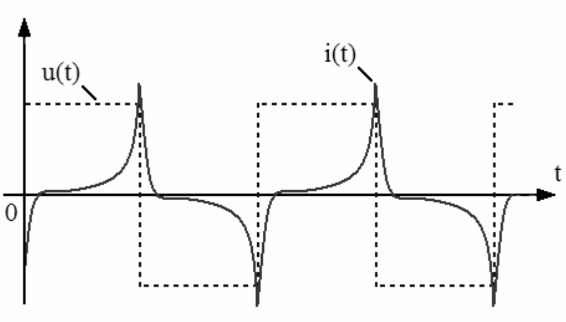

(**b**) Primary Current $I_p = 0$ A.

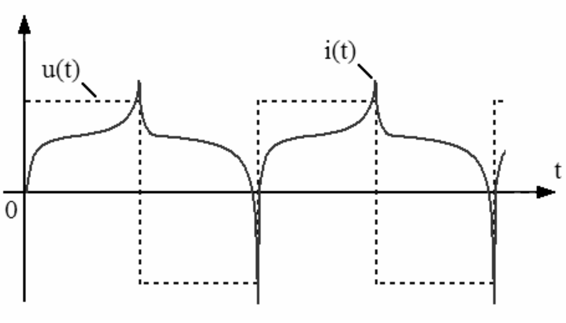

(**c**) Primary Current $I_p \neq 0$ A.

Figure 2.9: Fluxgate principle: the basic construction, voltage, and current waveforms of a fluxgate excitation winding.

The principle relies on the fact that magnetic material is symmetric and saturation points are equal in both directions $H_{max} = -H_{min}$, even though the absolute values are changing with respect to temperature and other variables. Therefore, for positive current I_p we obtain $H_e > 0$, and the field needed to reach the negative saturation point is greater than to reach the positive saturation point, i.e. $H_{xn} > H_{xp}$.

The principle of operation is shown in Figures 2.9, where Figure 2.9a shows the basic construction consisting of a primary winding and current I_p representing H_e, and addi-

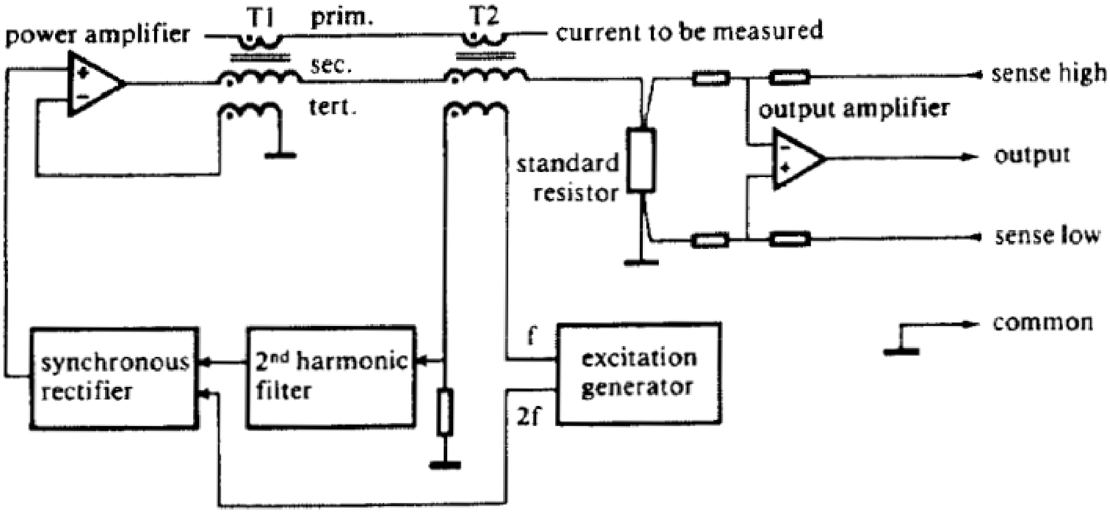

Figure 2.10: CERN: block diagram of zero-flux DCCT. T1 as AC transformer, T2 as zero-flux sensor, prim. as primary current to be measured, and voltage output.
©1977 IEEE. Reprinted with permission from [34].

tional excitation winding with voltage and currents $v(t), i(t)$ representing H_{xp} and H_{xn}. Waveforms, for a square wave voltage stimulus $v(t)$ of a balanced system when $I_p = 0$ A and under some current $I_p \neq 0$ A, are shown in Figures 2.9b and 2.9c respectively, where the shape of the current $i(t)$ is distorted with the presence of the primary current I_p.

The zero-flux compensation principle adds another compensation winding of N_{comp} turns, with a compensation current I_{comp}, which adds a generated compensation field H_{comp} to the external field H_e, i.e. $H_e + H_{comp}$. The system is in balance when $H_e + H_{comp} = 0$, meaning that the zero-flux compensation current I_{comp} is a perfect mirror of a primary current $I_{comp} = \frac{1}{N_{comp}} I_p$. Under these balanced condition, the hysteresis of the magnetic material in the positive and negative directions is equal and is thus fully cancelled.

One of the first gapless and wide-bandwidth zero-flux solutions based on this principle with a block diagram as shown in Figure 2.10 was introduced at CERN in 1976 [34]. There, the first transformer T1 serves as an AC path, while T2 operates as a zero-flux sensor. The operation is the same as explained at Figures 2.9. The excitation generator is constantly sweeping the current across the entire range from the minimum to the maximum saturation point, thus canceling out the magnetic offsets. If the flux is non-zero, the excitation current becomes asymmetrical, which is observable as the second harmonic distortion, a phase representing the sign and magnitude of the distance from zero balance. It is filtered out and demodulated to drive the compensation power amplifier to compensate the DC offsets. The small signal bandwidth obtained with this solution was 10 kHz, a gain accuracy of 100 ppm, a linearity of 5 ppm, an offset error of only 10 ppm, and temperature drifts of 1 ppm/K.

The excitation winding of T2 injects noise into the output, as well as into the primary conductor. The improved version therefore consists of three cores, with the additional T2' being added to operate in the opposite direction (180° phase shifted), as shown in Figure 2.11 [35]. When the excitation ampere-turns (At) between them, T2 and T2' are in perfect balance, the noise introduced by the excitation generator is canceled out. Sensors based on this zero-flux method are typically bigger-format high-performance instruments that are also consumptive and costly, making them overall unsuitable for mass market

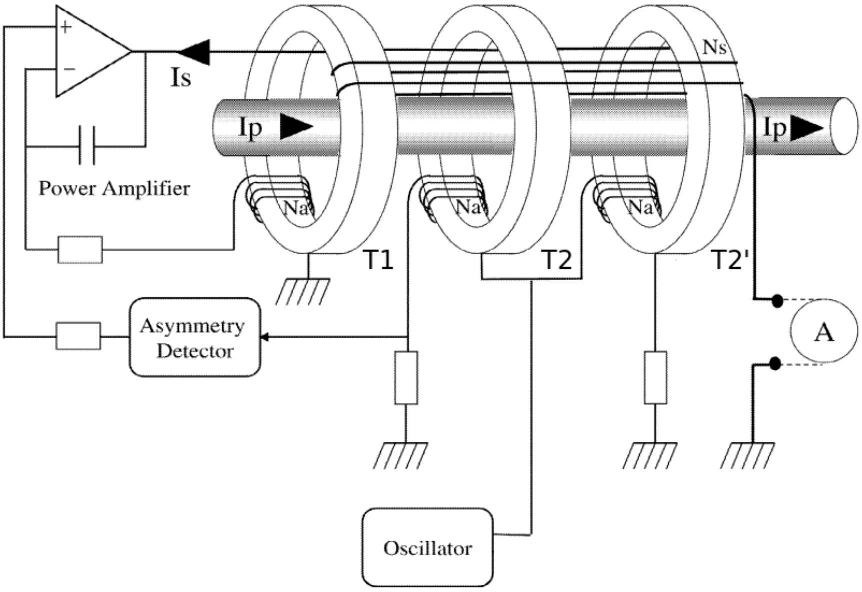

Figure 2.11: Block diagram of MACC zero-flux DCCT [34]. T1 as AC transformer, T2 and T2' as balanced zero-flux sensor, I_p as primary current to be measured, and A as current output. ©2002 IEEE. Reprinted with permission from [35].

use. Products based on this solution include MACC [36], LEM IT [30], and many others. Another approach to isolating the noise produced by the excitation cores is to embed this core inside another core. This concept has been successfully used by Hioki [37].

High sensitivity and low offset have increased the popularity of flux-gate sensors in various configurations: as a magnetic compass, an open-loop and differential current sensor, as a general purpose magnetic sensor, implemented as a cost-effective replacement alternative to Hall sensors on chip (e.g. DRV425[5]), and many others. They have even been printed on flex boards [38].

2.8 Fiber Optic Current Sensors

Fiber Optic Current Sensors (FOCS) rely on the Faraday effect in optics as shown in Figure 2.12. When a polarized light beam E passes through a glass medium in a magnetic field, its polarization vector θ rotates proportionally to the magnetic field strength B, described by the Verdet constant V [rad/A]:

$$\theta = VNI_p \tag{2.8}$$

where N is the number of turns around the primary conductor of current I_p, and θ is the angle of Faraday rotation.

The typical value of standard silica fibers have a Verdet constant of 1 μrad/A at 1300 nm [39], which requires hundreds of meters to reach a suitable sensitivity. Due to the known disadvantage, the so-called birefringence within the sensing fiber, which attenuates the measured signal and thus the sensitivity of the sensor, long fibres came out with very little signal and thus resolution. The typical resolution of a high performance system is in the range of 100 .. 200 ppm[6].

---

[5] `https://www.ti.com/product/DRV425`

[6] `https://new.abb.com/power-electronics/focs/faq`

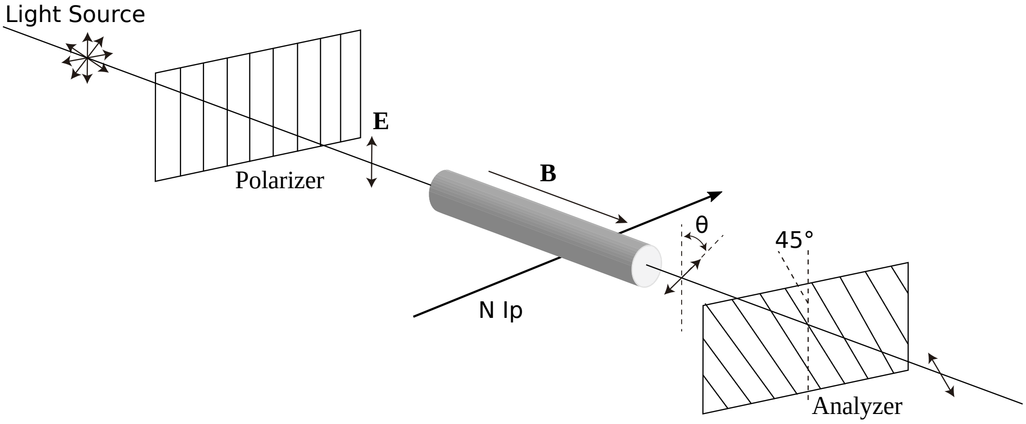

Figure 2.12: FOCS - Principle of operation with Faraday rotation effect.

Thermally annealed fibers, twisted fibers, and spun fibers have been developed to suppress the linear birefringence at the cost of a weaker mechanical strength. An alternative method to increase sensitivity is to add rare earth materials, such as terbium (Tb). This effectively increases the Verdet constant up to 40 μrad/A at 1064 nm, which is equivalent to 50.3 rad/T/m.

A typical FOCS system consists of a polarized light source, transmission fiber, Faraday sensor head (fiber), and an analyzer that is splitting the light into two orthogonal vectors, whose intensity is captured by the photo detectors [40]. The highest sensitivity can be obtained with the so-called Sagnac-based detection [41], [42], which uses an interferometer to measure the interference between the two counter-propagating paths. This architecture has been extensively studied and used in high sensitivity fiber optic gyroscopes [43] besides the FOCS. Another alternative method of interest similar to the zero-flux compensating current is using an additional Faraday modulator to create a negative rotational change. By creating a closed-loop system, in which a Faraday modulator driven by a secondary compensating coil I_{comp} perfectly compensates the angle from the sensing coil, then I_{comp} reflects the scaled down "mirrored" current of I_p [44].

The significant advantages of FOCS over other mentioned current sensing methods include a very high current range, ranging over 600 kA with negligible saturation effects, the electrical isolation (de-coupling) of a sensor element from the voltage line, its suitability for very high voltage (grid) systems, and very fast response times.

2.9 Summary

A wide range of diverse application areas with differing requirements and tolerances regarding the performance of current sensors has given rise to various methods and types of sensors being developed. These utilize different underlying physical principles, from ohmic resistance (e.g., shunt) and induction (e.g., Rogowski transformer, current transformer), to the magnetic field (e.g., Hall-effect sensors, fluxgate transformer, magnetoresistance materials), and the Faraday effect (e.g., fiber-optic current sensors) [45], each with its particular advantages and drawbacks. Table 2.2 outlines the key characteristics of the listed current sensing principles along with the desired, expected, target characteristics of the new sensor, based on the motivation from Chapter 1.1.

Applications, such as massive solar power plants, battery storage systems, and e-mobility, require compact and cost-effective current sensors with a large nominal measurement range from a few A up to several kA. The wide dynamic range is needed for an

Table 2.2: Summary of Technologies for High Current Measurements and target features for the new desired sensor.

Method	**Isolated**	**Range**	**Bandwidth**	**Linearity**	**Offset**	**Drift**	**Consumption**
Shunt	No	kA	MHz	<10 ppm	Low	Medium	Very High[1]
MOSFET	No	kA	>MHz	1%	Low	High	Very Low
AC Transformer	Yes	kA	>MHz	0.1%	-	-	Low
AC Rogowski Coil	Yes	MA	>MHz	0.1%	-	-	Low
Hall Closed-Loop	Yes	kA	<MHz	0.5%	High[2]	High	Medium
Magneto-Resistance Closed-Loop	Yes	kA	<MHz	0.5%	High[2]	Medium	Medium
High-end Fluxgate	Yes	kA	MHz	<10 ppm	Very Low	Low	High[3]
Fiber Optic (FOCS)	Yes	MA	>MHz	0.1%	Low	Low	High[3]
New Sensor	Yes	kA	MHz	<100 ppm	Low	Low	Medium

1. Considering higher currents >300 A
2. Includes offset of a magnetic material
3. High power considered when >10 W

accurate acquisition of short temporary currents of several orders of magnitude above the nominal average (e.g., e-vehicle acceleration, in-rush currents in battery storage, etc.). The identified missing gap on the market are low-cost sensors with a measurement uncertainty of 3σ ranging from 0.01% to 0.1%. Such sensors require linearity that is at least 5 times better, low offset, and very low temperature drift over an extended industrial temperature range (i.e. -40 .. 105°C). The emerging high frequency switching applications require a bandwidth in the MHz range. The competitive DC technologies are shunt, closed-loop Hall and MR transducers, and the flux-gate.

Shunts perform very well in the low-current domain, whereas at medium to high currents, they exhibit high power losses, which turn into a pure and undesirable heat dissipation. They show high sensitivity to temperature drifts, consequently derated accuracy, and may have limited withstanding overloading characteristics at inrush current surges and voltages. A high quality shunt measurement at the end leads to higher-quality material requirements and more expensive production. The shunt measurement circuitry needs to support low-drift and accurate analog electronics, may require high voltage isolation, which adds up in costs and the final size of the measurement module.

Hall closed-loop sensors are the lowest cost high current transducers, however their accuracy is limited to around 1% over a wider temperature range. This is mainly because Hall sensors are inserted into the magnetic circuit with an air gap, which reduces sensitivity, immunity to external fields, and increases offset. TMR magnetoresistance sensors significantly outperform Hall sensors, however similar to Hall sensors, they add an air gap to a magnetic circuit, which reduces the overall performance.

That is why the gapless flux-gate sensors have shown to have many real world implementations. The most accurate and costly zero-flux flux-gate implementation with a magnetic core can reach absolute accuracy at the level of < 10 ppm of the measuring current range, typically valid in the range between 300 A and 2 kA. A typical flux-gate sensor is bandwidth limited. Further advancements proposed dual-core and tri-core implementations to extend their dynamic range and noise performances. The overall drawbacks are their size and power consumption, making them predominantly suitable for use in special applications, such as accelerators (cyclotrons, synchrotrons), test and measurement devices, medical devices, such as magnetic resonance, and so on. Such solutions are costly, complex, bigger, and operate at a high quiescent current.

A flux-gate sensor is quasi-independent of thermal drifts. Its benefits have led to lower cost implementations, as is the LEM CASR, and consist of a single higher permeability main core into which a ferrite material is inserted, operating as a flux-gate sensor. The sensor magnetizes the lower portion of the material and thus operates at a lower power consumption. However, such sensors are just slightly better than the Hall sensors, because:

1. the overall core permeability cannot reach the initial main core permeability due to the two-part structure design,
2. temperature drift is still largely present due to the main core itself,
3. flux-gate modulation produces a lot of noise,
4. the relatively slow sampling frequency of about 450 kHz does not make this sensor really usable above 100 kHz.

In the light of these challenges, this dissertation focuses on a design of a transducer based on the:

- zero-flux principle to retain and improve the superb performance in terms of the linearity, and

- gapless core to maximize sensitivity, immunity at lowest DC offsets, similar to the one achieved with the fluxgate principle.

The zero-flux (null) method also offers the widest frequency bandwidth at a modest power consumption, as known to AC current transformers. The main challenge of the research presented in this dissertation was therefore:

> *to invent a new type of DC/AC flux sensor that can be embodied into a compact, single, gapless core.*

The research led to an innovation, the Platiše Flux Sensor (PFS)[17], described in the following chapters.

Chapter 3

Modelling Magnetic Circuits for Mixed Signal Simulation

In this chapter, methods and models are developed to perform a system simulation of a newly designed magnetic flux sensor and a complete DC-CT. A simplified and fast simulation of magnetic circuits with a current transformer are represented in Chapters 3.1 and 3.2, followed by an integration and a co-simulation of Verilog digital circuits in Chapter 3.3, and a co-simulation of firmware written in C in Chapter 3.4.

The system verification is based on an advanced, free, and open-source spice simulation software named ngspice[1], which has been upgraded in the scope of this research into a full co-simulation framework with Verilog and embedded firmware[2], to enable us to simulate closed loops with digital controllers and filters. The spice macro models with a simulation of magnetic fluxes in newly designed magnetic cores were designed in a freely available FEM simulator[3].

Due to the relatively high tolerances (over ±25%) of soft-magnetic materials, the absolute accuracy of magnetic models are not of the greatest importance, but rather their typical characteristics, simplicity, and stable convergence. Having this in mind, the developed methods and control loops should not be too sensitive in order to guarantee operation in a wide temperature range and under various ambient conditions.

3.1 Magnetic Circuits

3.1.1 Non-Linear Model of a Ferrite Material

Ferromagnetic materials are characterised by a large susceptibility to an external magnetic field (high permeability); they saturate at a certain maximum flux density and retain a portion of it after the external field is relaxed, which is called retentivity or residual flux density B_r. To clear the residual flux down to zero, an opposite magnetic force is to be applied of the value H_c named coercivity.

Jiles and Atherton [46], [47] developed a theory of ferromagnetic hysteresis as early as in 1983-1986 by separately describing the reversible (anhysteretic) and irreversible functions and their base theory is still claimed to be the most accurate for soft ferrites [48]. Variations of their model have been implemented in commercial simulators and have been further improved to also include frequency dependency [49]. Other widely known models include

---

[1] `http://ngspice.org`

[2] `http://isotel.org/mixedsim`

[3] `http://femm.info`

the Rayleigh Loop Model, Preisach [50]–[52], Chan-Vladirimescu [53], and Hodgdon [54], [55].

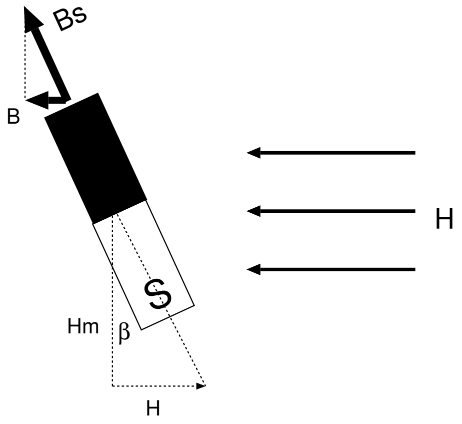

Figure 3.1: Macro model of a ferrite material in which an external magnetic field H, perpendicular to a dipole momentum field H_m, exercises torque to a magnetic dipole with the magnetic flux density B_s and yields a total magnetic flux density of B.

However, a modelling of the entire hysteresis loop was not really needed within the scope of this research, only the central value of the non-linear characteristics of the core. An approximate and fast macro model was derived intuitively as depicted in Figure 3.1.

Let us consider a hypothetical material where a set of numerous dipoles with a total magnetic flux density B_d [T] are all aligned perpendicularly to the core by a magnetic field strength H_m to which an external magnetic field H [A/m] is applied. The magnetic field H creates a momentum with each dipole trying to turn it around away from H_m, whose angle can be described with $\beta = \arctan(H/H_m)$. As the dipole turns towards the H axis, it adds to the magnetic flux density as $B = B_s \sin(\beta)$ in parallel to the magnetic flux density of an empty space $B = \mu_0 H$. This yields the following relation for the vector $\overrightarrow{B}$ in the direction of $\overrightarrow{H}$:

$$B(H) = B_s \cdot \sin\left(\arctan\frac{H}{H_m}\right) + \mu_0 H \tag{3.1}$$

B(H) is a continuous function that may further be simplified to a simple and much faster computed[4] non-trigonometric function. Furthermore, under the assumption that $\mu_r > 1000$, the tiny contribution of an empty space μ_0 may also be neglected:

$$B(H) = H \cdot \left(\frac{B_s}{\sqrt{H^2 + H_m^2}} + \mu_0\right) \approx B_s \cdot \frac{H}{\sqrt{H^2 + H_m^2}} \tag{3.2}$$

The resulting function is smooth with a continuous first (and further) derivative, which ensures convergence within the ngspice numerical simulation.

$$\frac{dB(H)}{dH} = B_s \cdot \frac{H_m^3\sqrt{H^2/H_m^2 + 1}}{(H^2 + H_m^2)^2} \tag{3.3}$$

For $H_m > 0$, Eq. (3.3) can be modified to:

$$\frac{dB(H)}{dH} = B_s \cdot \frac{H_m^2\sqrt{H^2 + H_m^2}}{(H^2 + H_m^2)^2} \tag{3.4}$$

---

[4] `https://latkin.org/blog/2014/11/09/a-simple-benchmark-of-various-math-operations`

which simplifies the actual implementation due to common terms with Eq. (3.2).

The characteristics of ferromagnetic material 26G from Iskra Feriti is shown in Figure 3.2a for which a non-linear curve fitting was applied, by using the python `scipy.curve_fit()`, for approximating the center values between the upper and the lower hysteresis loop. The result is shown in Figure 3.2b. The model has also been successfully verified on materials 15G, 22G, 45G, and others from Iskra Feriti.

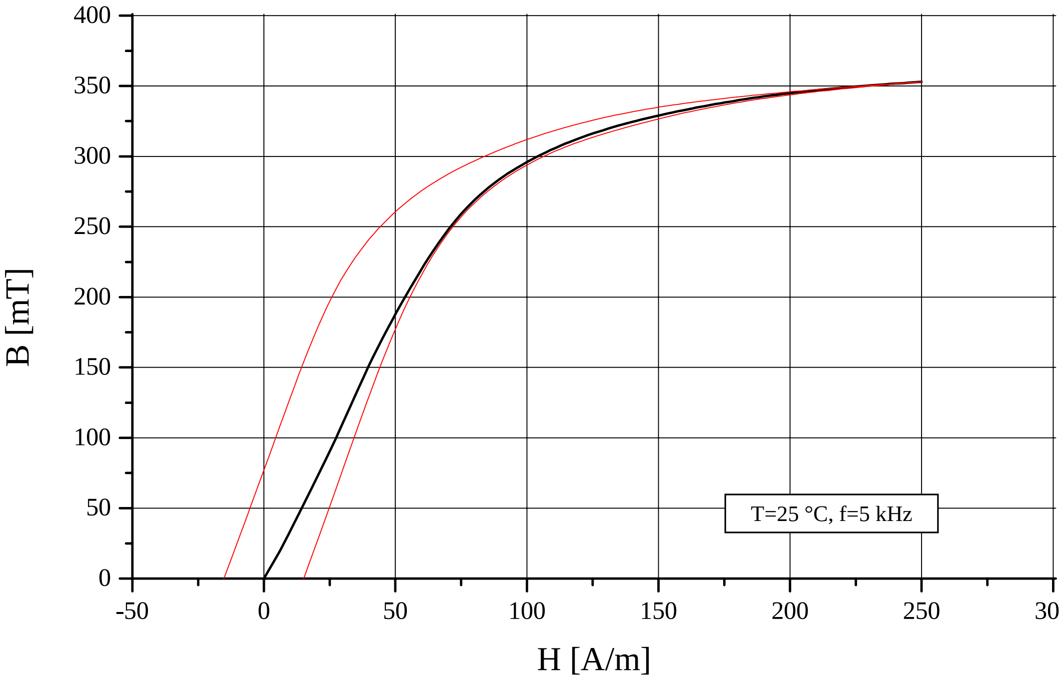

(**a**) Magnetization curve from the 26G data-sheet.

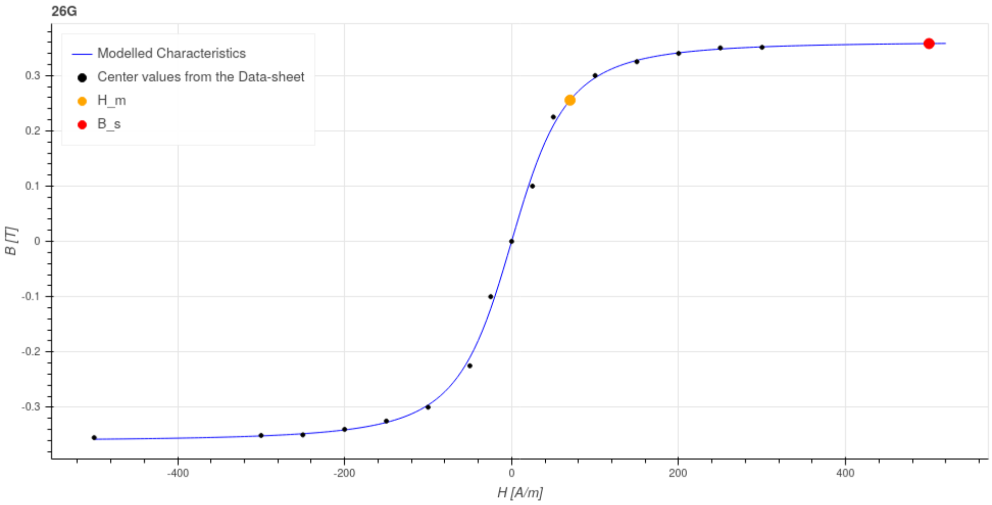

(**b**) Modelled 26G ferrite, $H_m = 70$ A/m, $B_s = 0.361$ T at $T = 25°\text{C}$, $f = 5$ kHz.

Figure 3.2: Quasistatic magnetization curve of the Iskra Feriti 26G material.

This (new) simple macro model has the following properties:

- good fit for non-hysteresis loops,
- fast and simple continuous function with continuous derivatives, thus it converges

easily, and

- easy to tune with the two parameters that can only be directly read out from the data-sheet chart of the material where B_s represents a quasi-saturation point and H_m a magnetic field strength at about $0.71B_s$, which denotes a dipole mid-angle $\beta = 45°$.

To this macro model a hysteresis may be introduced as an angle deformation of the H_m due to H, temperature dependency by providing the temperature T dependency characteristics to the parameter $B_s(T)$, and frequency dependency by providing a pole. However, for the development of the zero-flux DC-CT principle, as represented in this dissertation, further complications are unnecessary.

3.1.2 Equivalent Electric Model

Magnetic circuits may be simulated using standard electric circuit simulators, such as ngspice and others. By replacing the magnetic flux ϕ and magneto-motive force Θ, with I as current and V as voltage, a ferrite material may be described as a resistor with a non-linear transfer function derived from Eq. (3.2):

$$\phi = A_f \cdot B(\frac{\Theta_f}{l_f}) = R_f^{-1}(\Theta_f) \tag{3.5}$$

where R_f is an equivalent non-linear resistance of the ferrite material with a cross-sectional area A_f and effective length l_f. The Θ_f represents a magnetic voltage along the l_f. Similarly, an air gap may be represented by a simple linear resistor:

$$\phi = \frac{A_g}{l_g}\mu_0\Theta_g = R_g^{-1}\Theta_g \tag{3.6}$$

where A_g is a cross-sectional area of an air-gap with the length l_g, but it is not needed in the following since the newly developed method is based on a gapless core. The coils link magnetic and electric circuits by the following relations:

$$v = -N\frac{d\phi}{dt} = L\frac{di}{dt} \tag{3.7}$$

$$\Theta = iN \tag{3.8}$$

The first relation describes voltage v induced in the electric circuit due to the flux ϕ change in a magnetic circuit and the second relation creates a magneto-motive force due to the electric current i in a coil with N turns.

3.1.3 ngSpice Models

3.1.3.1 Core Implementations and the Xspice Code Model: Core

The non-linear resistor from Eq. (3.5) was implemented in four ways:

1. As a sub-circuit with trigonometric functions.
2. As a sub-circuit with a root-square.
3. As an open-source ngspice code-model; actually, the existing xspice `core` model has been upgraded with the third mode option PLATISE (3) besides the existing PWL (1) and HYST (2) modes, by implementing Eq. (3.2) and Eq. (3.4).

4. Compared with the existing ngspice PWL linear segment approximation mode.

Options 1, 2, and 4 were implemented as shown in Listing 3.1 together with a simple benchmark code. The xspice code model implementation of option 3 is shown in Appendix A. The benchmarks are shown in Table 3.1. The code-model in PWL and PLATISE mode runs the fastest while PLATISE mode offers smooth derivatives and the fastest way to model a new material. The simulation results of the PWL and the PLATISE modes are shown in Figure 3.3.

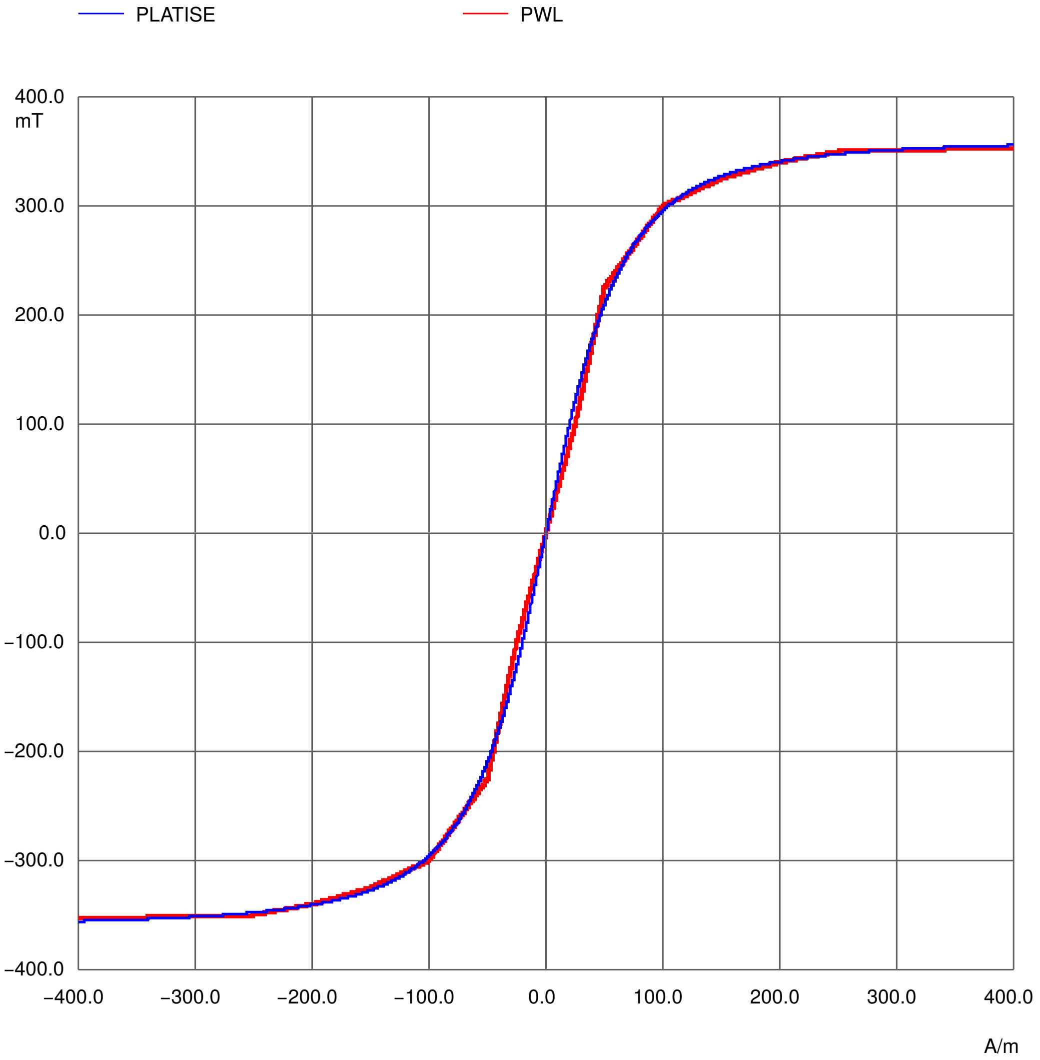

Figure 3.3: Comparison of the PLATISE and PWL core modes for the Iskra Feriti 26G material within the ngspice simulator.

3.1.3.2 Coil Implementation

Coil Eqs. (3.7) and (3.8) are implemented within the ngspice in the `lcouple` code model and an alternative implementation as a sub-circuit is shown in Listing 3.2. The sub-circuit implementation executes about 5% faster than the code-model, as it is using the basic

Listing 3.1: ngspice ferrite core models with a test circuit.

```
Iskra Feriti 26G B-H Models

.param A   = 2.3u
.param len = 1

****************** OPTION 1 ******************

* fcore dc-ct model <uros@isotel.org>, March 2016
* Ferite Core, where A is cross sectional area [m2], l length [m],
*               Hm [A/m] and Bs [T] are model parameters.
.subckt fcore 1 2 A=1 l=1 Hm=70 Bs=0.361
B1 1 2 I = A*Bs*sin(atan( (v(1,2))/Hm/l ))
.ends

****************** OPTION 2 ******************

.subckt fcore2 1 2 A=1 l=1 Hm=70 Bs=0.361
.param Hm2 = pow(Hm*l,2)
.param phi = A*Bs
B1 1 2 I = phi*v(1,2)/sqrt(pow(v(1,2),2)+Hm2)
.ends

****************** OPTION 3 ******************

.model if26g core (H_array=[70] B_array=[0.361] area={A} length={len})

****************** OPTION 4 ******************

.model if26gtbl core (
+   H_array = [-1000 -500 -300 -250 -200 -150 -100 -50 -25 0
+              25   50  100  150  200  250  300 500 1000]
+   B_array = [-0.357 -0.355 -0.351 -0.35 -0.34 -0.325 -0.3 -0.225
+     -0.1 0 0.1  0.225  0.3  0.325  0.34  0.35  0.351  0.355  0.357]
+              area={A} length={len})

****************** TEST CASE ******************

A1 (1 0) if26gtbl
V1 1 0 PULSE(-400 400 0 0.8ms 1ms)

A2 (2 0) if26g
V2 2 0 PULSE(-400 400 0 0.8ms 1ms)

X3 3 0 fcore A=A l=len
V3 3 0 PULSE(-400 400 0 0.8ms 1ms)

.control
    tran 1ns 0.8ms
.endc
.end
```

Table 3.1: Performance Benchmark in ngspice simulation and various implementations of the Ferrite Core as per Eq. 3.2 normalized to ngspice transient analysis without any circuit.

Implementation	**Execution Time [s]**	**Relative**
Sub-circuit `fcore` with triangular functions	6.5	1.86
Sub-circuit `fcore2` with root-square	7.0	2.00
Core Code-Model in PLATISE mode	4.1	1.17
Core Code-Model in PWL mode	4.1	1.17
Simulation time without any circuit (transient only)	3.5	1.00

Listing 3.2: ngspice coil model.

```
* mmfcoil MMF Coil of N Turns, <uros@isotel.eu>, August 2012, March 2016
*
* flux currents are denoted by C (core) pins and
* electrical currents denoted with L (inductance) pins.
*
*                    L+L-C+C- number of turns
.subckt mmfcoil      1 2 3 4  N=1
Ec 1 2 11 0 1
Hc 3 4 Ec {N}
Lc 11 0 1
Rp 11 0 1e7
Fc 11 0 Hc {N}
.ends
```

elements of the spice, and it provides additional low-pass filtering to smooth high speed transients that would otherwise cause convergence problems in switching applications. The implementation includes the following spice elements:

- `Hc` current-controlled (MMF) voltage source implements $\Theta = iN$, which reflects the current through `L` terminals to magnetic flux (current),
- `Ec` voltage-controlled voltage source maps the induced flux change to a voltage on electric terminals `L`,
- `Fc` current-controlled current source reflects the flux passing through the `Hc`,
- `Fc` current drives inductance `Lc`, where its voltage represents the first derivative, and
- the additional parallel (parasitic) resistance `Rp` provides leakage that limits excessive $d\phi/dt$ changes that would otherwise cause a divergence of the simulator. Effectively, `Rp` limits a bandwidth of coupling with the core.

3.2 Current Transformer

A closed-loop DC-CT is a *DC corrected* zero-flux AC transformer. Hence, we started by modeling the DC-CT from the design of a very simplified low-frequency current transformer model [22], [23] with one primary and one secondary winding N_1 and N_2, with primary and secondary currents i_1 and i_2, terminated by a shunt resistance R on the secondary side, as shown in Figure 3.4. The series resistance of the secondary winding R_s may be added to this same R. The magnetizing current, and thus inductance L, is considered to be the key part of the transformer and is therefore not drawn separately.

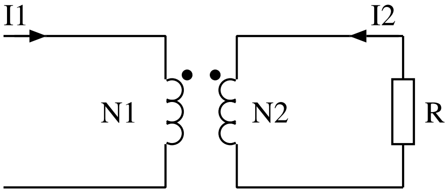

Figure 3.4: Simplified model of a current transformer.

The two transfer functions which are of our interest for modeling are the magnetic flux vs. input current $\phi(i_1)$ and the output current vs. input current $i_2(i_1)$. With the former, we gain insights in the ferrite core to understand its basic limitations, and the latter provides an input vs. output transfer function.

3.2.1 Simplified Model

The magnetomotive force (MMF) balance for the basic model above is given as:

$$\phi\frac{l}{A\mu} = i_1 + i_2 N \tag{3.9}$$

Traditional transformers need an air-gap to prevent the core from saturation. Herein, we may assume it is already taken into account within the effective permeability μ. The parameter l represents the effective length and A the cross section area of the core. For the primary winding, a single turn is assumed and the secondary winding has N turns.

The input is fed by the current source i_1. The output is terminated by effective resistance R, which includes the winding resistance and the meter input resistance for the sake of simplicity. The voltage at the second winding equals:

$$u_2 = -N\frac{d\phi}{dt} \tag{3.10}$$

and the current loop:

$$i_2 = \frac{u_2}{R} \tag{3.11}$$

Substituting these expressions into Eq. (3.9) and applying *Laplace* transformation, we get:

$$\Phi(s) = I_1(s)\left(\frac{l}{A\mu} + s\frac{N^2}{R}\right)^{-1} \tag{3.12}$$

Replacing the $N^2\frac{A\mu}{l}$ with inductance L, the impulse response of the circuit is:

$$\Phi(s) = I_1(s)\frac{R}{N^2}\left(\frac{R}{L} + s\right)^{-1} \tag{3.13}$$

The solution to this equation for unit response is:

$$\phi(t) = I_{U1}\frac{L}{N^2}\left[1 - e^{-\frac{t}{L/R}}\right] = I_{U1}\frac{A\mu}{l}\left[1 - e^{-\frac{t}{L/R}}\right] \tag{3.14}$$

For AC transformers, Eq. (3.13) could be simply rearranged by replacing s with $j\omega$:

$$\Phi(j\omega) = I_1(j\omega)\frac{R}{N^2}\left(\frac{R}{L} + j\omega\right)^{-1} \tag{3.15}$$

Replacing the inductance L with $L = A_L N^2$, which are given in the core data-sheets, the absolute value of the flux is:

$$\Phi = I_1 \frac{R/N^2}{\sqrt{(R/L)^2 + \omega^2}} = I_1 \frac{R/N^2}{\sqrt{(R/A_L)^2/N^4 + \omega^2}} \tag{3.16}$$

To prevent the core from saturation, the magnetic flux density $B = \Phi/A$ must be within the ferrite core limits across the entire temperature range. Note that the saturation value decreases significantly at higher temperatures[5]. The higher the A_L factor (permeability) and the number of turns N at the lowest possible series resistance R, the lower the frequencies a transformer can measure correctly.

3.2.2 Input vs. Output Response

The input vs. output transfer function is obtained in a similar way by substituting Eq. (3.9) into Eq. (3.10), and the result into Eq. (3.11):

$$I_2(s) = -I_1(s)\frac{s/N}{R/L + s} \tag{3.17}$$

Response to the unit pulse in the time domain is given by:

$$i_2(t) = -i_1(t)\frac{1}{N}e^{-\frac{t}{L/R}} \tag{3.18}$$

3.2.3 Bandwidth

Both transfer functions, the $\Phi(s)$ and the $I_2(s)$, imply the same time constant $\tau = L/R$, which makes the current transformer act like a high-pass filter. Increasing the time constant (moving the pole toward zero) increases the lower part of the bandwidth of the transformer. A theoretical DC current transformer would require $\tau \to \infty$. The transfer function in Eq. (3.17) and its unit response in time domain would then become:

$$I_2(s) = -I_1(s)\frac{1}{N} \tag{3.19}$$

However, since this is not practically possible, an additional mechanism is required to extended the lower bandwidth down to 0 Hz. The bandwidth of the current transformer therefore ranges between the lower cut-off frequency, defined by the R/L, and the upper cut-off frequency limited by the winding leakage inductance, stray capacitance, and the ferrite material itself as shown in Figure 3.5 for material 26G. The core limitations can be simply modeled with the inductance L serially in an electric equivalent of the magnetic circuit. The models used in the simulation should have a lower bandwidth than the time step interval (even though it reduces automatically) to avoid convergence issues. Leakage inductance and capacitance introduce additional zeros and poles, which alter the flatness of the $i_2(i_1)$ transfer function.

---

[5] `https://product.tdk.com/en/products/ferrite/ferrite/ferrite-core/index.html`

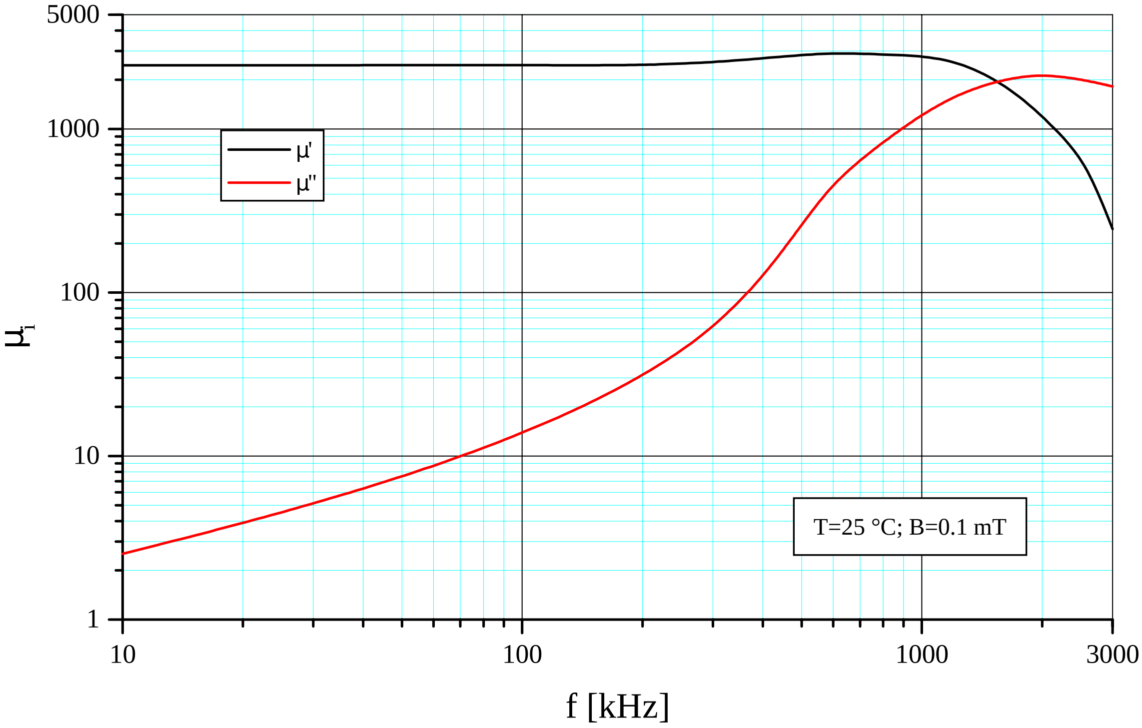

Figure 3.5: Complex permeability vs. frequency of the Iskra Feriti 26G Material.

3.2.4 Quasi-Zero Field Transformers

Wire resistance R_s is proportional to the physical dimensions of the coil, such as the wire width and total length, while the termination resistance, also called a burden resistor, is typically chosen for the best resolution at the output at a minimal distortion of the core.

The termination resistance R, which is composed of a series resistance of the secondary winding and the shunt resistance, has another important impact: decreasing its value not only increases the time constant but also decreases the flux at some frequency $\omega > 0$ as seen in Eq. (3.16). The quasi-zero field transformer concept as introduced in Section 2.3 reduces the termination resistor down to nearly 0 Ω by using an OPAMP as shown in Figure 3.6 and earlier in Figure 2.3. Having virtually removed the termination resistance, the only resistance that remains is of the winding, which may also be very low, resulting in near zero-flux AC operation while amplifying the output voltage, and thus increasing sensitivity, proportionally to the R_F. The output voltage is given by:

$$U_O = i_2 R_F \tag{3.20}$$

A quasi-zero field transformer concept extends the dynamic range of transformers in terms of current and bandwidth. It prevents premature saturation, especially on smaller sized cores with high permeability.

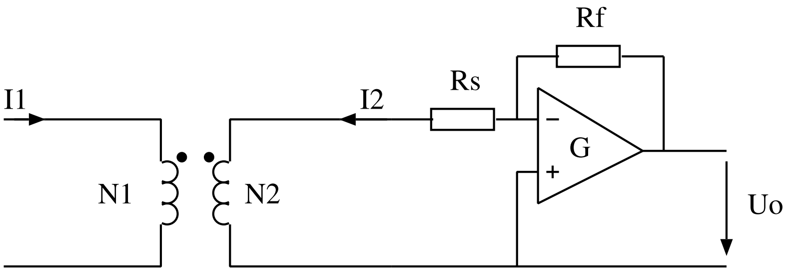

Figure 3.6: Concept of a Quasi-Zero Field Current Transformer.

3.3 Mixed Signal Simulation with Digital Circuits

For the performance evaluation and verification of the proposed design, the ngspice simulation environment was used. Ngspice is a general-purpose circuit simulation program for nonlinear and linear analyses with mixed-level circuit extensions:

- XSPICE, powerful analog and event-based mixed-signal simulation,
- CIDER, a mixed-level circuit and device simulator, and
- Verilog-A.

Xspice provides numerous additional analog, digital and hybrid models and introduced an additional 12 digital node types: 0s, 1s, Us, 0r, 1r, Ur, 0z, 1z, Uz, 0u, 1u, Uu. Within the scope of this research and for the possible development of integrated circuitry, an additional tool Yosys[6] for Verilog synthesis was incorporated into the process flow to ease the digital design. The implementation of this integration includes the xspice technology library, which maps the primitives from the Yosys synthesis to the ngspice event-based digital circuit elements. In this way, the direct support of a relatively fast Verilog co-simulation with analog circuitry has been introduced to the ngspice environment and published as open source[7].

The motivation for using open-source tools over other commercial packages is as follows:

- evolution of good software builds a strong community and thus the development practically never ends, keeping the software up to date with the latest needs,
- as the community grows, so does the support, forums, irc channels, etc.,
- the software can be extended and have bugs fixed by its more experienced users,
- it leverages the knowledge of the entire community, for common good, especially when software is non-proprietary licensed with either GNU, FreeBSD, Apache, and other licenses of this type[8].

3.3.1 Tools and Process Flow

Figure 3.7 represents the process flow and the tools used in addition to the ngspice:

- Yosys package, providing Verilog to digital primitive cells synthesis,

---

[6] `http://www.clifford.at/yosys/`

[7] `http://isotel.org/mixedsim`

[8] `https://opensource.org/licenses`

- Mixedsim ISOTEL Library, a technology mapping library for the Yosys and ngspice,
- Iverilog, a Verilog verification (simulator) tool,
- gtkwave, a Verilog waveform viewer,
- graphviz, used to display the synthesised net-list graphically.

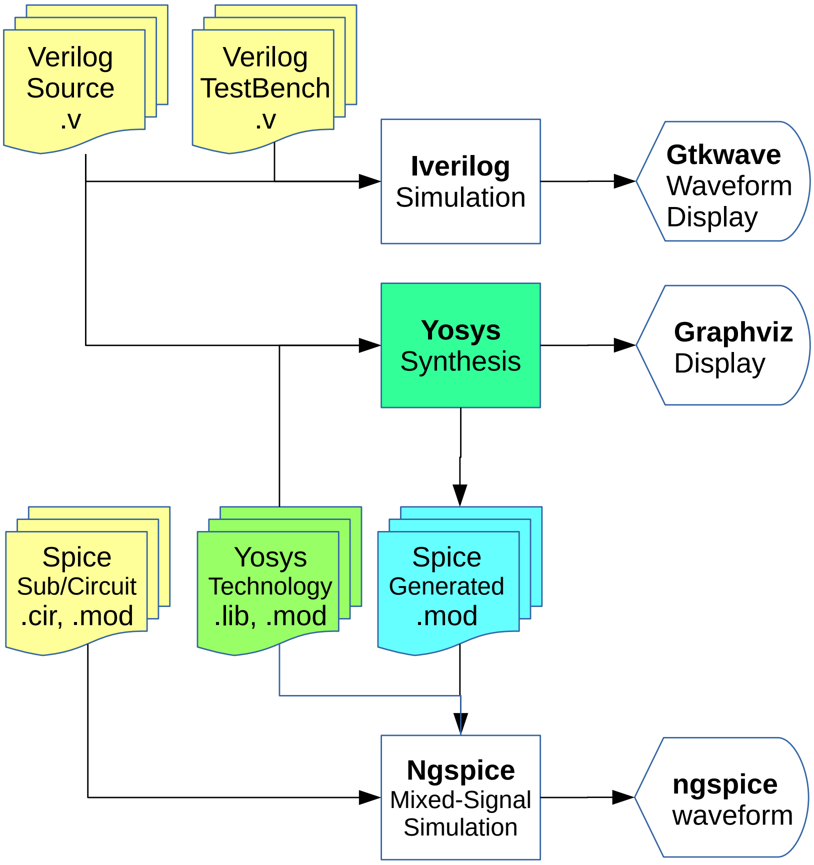

Figure 3.7: Process flow of the Verilog co-simulation within the mixed signal ngspice.

3.3.2 Example

For a simple Verilog pseudo-random generator with a compare function for use with the ngspice shown in Listing 3.3, the compilation procedure from Listing 3.4 generates a stand-alone ngspice sub-circuit module `prsgen8_ngspice.mod`. The example of instantiated generated sub-circuit is shown in Listing 3.5.

Listing 3.3: prsgen8.v: 8-bit pseudo random generator with compare in Verilog.

```
module prsgen8 (clk, rst, compare, out);
    input clk, rst;
    input [8:1] compare;
    output reg out;
    reg [8:1] sr;
    always @(posedge clk)
    begin
        if (rst) begin
            sr  <= 8'b10101010;
            out <= 0;
        end
        else begin
            sr[8:2] <= sr[7:1];
            sr[1]   <= sr[4] ^ sr[5] ^ sr[6] ^ sr[8];
            out     <= (compare >= sr);
        end
    end
endmodule
```

Listing 3.4: Yosys synthesis generates ngspice module.

```
read_verilog prsgen8.v
read_verilog -lib ../../yosys/prim_cells.v
proc;; memory;; techmap;;
dfflibmap -liberty ../../yosys/prim_cells.lib
abc -liberty ../../yosys/prim_cells.lib;;
write_verilog prsgen8_syn.v
write_spice -neg d_low -pos d_high prsgen8_ngspice.mod
```

Listing 3.5: Usage of Yosys generated netlist within the ngspice.

```
.include ../../yosys/prim_cells_ngspice.mod
.include prsgen8_ngspice.mod

* PRS with Compare Generator
Xprs dclk drst s0 s1 s2 s3 s4 s5 s6 s7 dprsout prsgen8

...
```

3.4 Embedded Firmware

Another advancement introduced to the ngspice is the direct co-simulation of a firmware written in C, also published as open-source, to allow the direct verification of digital filters and control loops implemented in micro-controllers. In contrast to the widely known SystemC simulation, the idea was to reuse exactly the same code as would finally run inside the micro-controller and with ease. For this purpose, an Xspice code-model was introduced named `d_process`.

3.4.1 Xspice Code Model: d_process

Firmware can be represented as a synchronous state-machine with an arbitrary number of digital inputs, outputs, a system reset and a system clock, as shown in Figure 3.8. This is essentially the d_process, a code-model with:

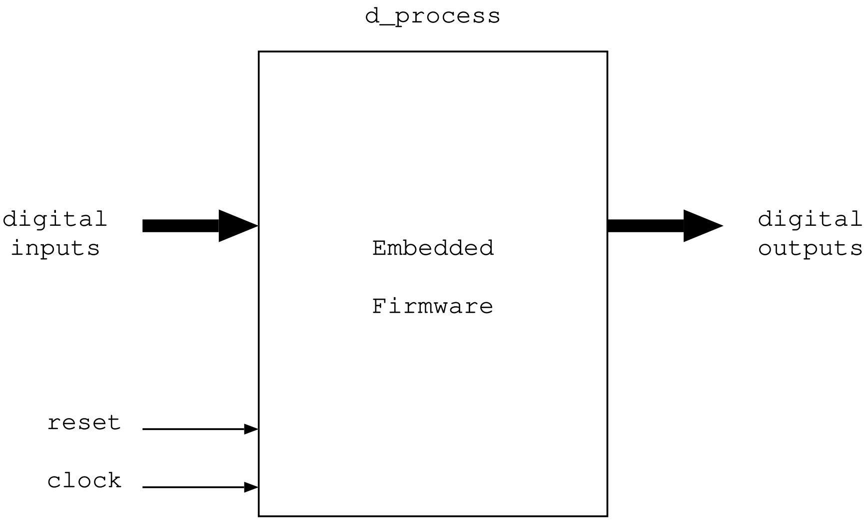

Figure 3.8: Xspice code model: d_process.

- a variable number of digital inputs and outputs,
- an optional digital synchronous reset input, and
- a mandatory digital clock input.

Upon every rising edge of the clock, all the inputs are sampled and transferred to an external process through the pipe, whose process must in return provide new output states. If the actual target platform is an ARM embedded system, one may use the ARM cross-compiling toolchain, the qemu as an ARM emulator with the GDB to run and/or debug the code in an actual ARM environment.

3.4.2 Example

An example of a C-controller with a 12-bit digital input (i.e. ADC) and an 8-bit output (PRS/PWM output) is shown in Listing 3.6 together with the `main()` function compiled

Listing 3.6: The controller function in C.

```
#include <string.h>
#include <stdlib.h>
#include <fcntl.h>
#include "d_process.h"

#define DIGITAL_IN      12      // 12-bit input from A/D
#define DIGITAL_OUT     8       // 8-bit output to PWM.width

uint8_t controller(uint32_t sample, int32_t Kp, int32_t Ki,
                   uint8_t reset) {
    ...
    return result;
}

int main(int argc, char *argv[]) {
    struct in_s {
        double time;
        uint8_t din[D_PROCESS_DLEN(DIGITAL_IN)];
    } __attribute__((packed)) in;

    struct out_s {
        uint8_t dout[D_PROCESS_DLEN(DIGITAL_OUT)];
    } __attribute__((packed)) out;

    for (int i=0; i<argc; i++) {
        if (strcmp(argv[i],"kp")==0 && i+1 < argc) {
            Kp = strtod(argv[++i], NULL);
        }
        if (strcmp(argv[i],"ki")==0 && i+1 < argc) {
            Ki = strtod(argv[++i], NULL);
        }
    }
    fprintf(stderr, "%s(Kp=%i,␣Ki=%i)\n", argv[0], Kp, Ki);

    if (d_process_init(pipein, pipeout, DIGITAL_IN, DIGITAL_OUT) ) {
         while(read(pipein, &in, sizeof(in)) == sizeof(in)) {
             /* create a 16-bit value from 12-bits packed in 2 bytes
              * negative time denotes d_process.reset=1
              */
             out.dout[0] = controller(
                 ((uint16_t)(in.din[1])<<8) + (uint16_t)in.din[0],
                 Kp, Ki, in.time < 0);

             write(pipeout, &out, sizeof(out));
         }
         return 0;
     }
     return -1;
}
```

Listing 3.7: Instantiation of the d_process code model within the ngspice.

```
.model firmware d_process (process_file="controller_ngut"
   process_params=["Kp=10", "Ki=2"])
Acontrol [di0 di1 di2 di3 di4 di5 di6 di7 di8 di9 di10 di11]
+ clk rst [do0 do1 do2 do3 do4 do5 do6 do7] firmware
```

into the `controller_ngut`, and an example of ngspice instantiation in Listing 3.7. Optional parameters `Kp` and `Ki` are passed as command line arguments, parsed at the beginning of the `main()` followed by the `while()` loop, which receives data on every rising edge of the clock `clk`, calls the `controller()` function, and returns the result on the same rising edge. The call to the `controller()` function may be equivalent for an ADC interrupt or event from a scheduler, post-processing, filtering the ADC input, and feeding a control loop to return a result.

3.5 Eagle Support

Hand written text files of large spice circuits are generally hard to read and visualize and are often erroneous. To this end, the Eagle[9] tool, a cross-platform high quality EDA software, can be utilized, whose functionality can be extended by writing User Language Programs (ULP).

In this respect, the ngspice ULP extension was developed with the aim to be able to annotate schematics using Eagle Schematics attributes, from which a valid spice circuit and sub-circuits are generated. In addition, an ngspice library, as shown in Figure 3.9, was developed with a collection of spice3f4 and xspice analog, digital, hybrid and real-value based components, as well as extensions to external sub-modules, such as Verilog and embedded C firmware code described earlier in this chapter.

---

[9] `https://www.autodesk.com/products/eagle`

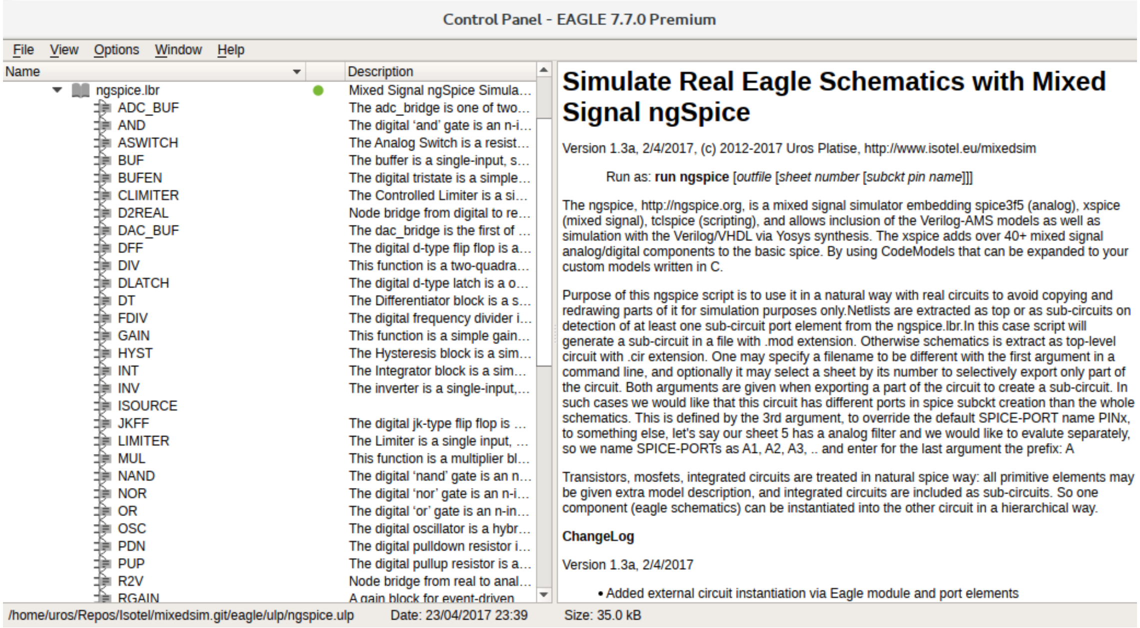

Name	Description
ngspice.lbr	Mixed Signal ngSpice Simula…
ADC_BUF	The adc_bridge is one of two…
AND	The digital ‘and’ gate is an n-i…
ASWITCH	The Analog Switch is a resist…
BUF	The buffer is a single-input, s…
BUFEN	The digital tristate is a simple…
CLIMITER	The Controlled Limiter is a si…
D2REAL	Node bridge from digital to re…
DAC_BUF	The dac_bridge is the first of …
DFF	The digital d-type flip flop is a…
DIV	This function is a two-quadra…
DLATCH	The digital d-type latch is a o…
DT	The Differentiator block is a s…
FDIV	The digital frequency divider i…
GAIN	This function is a simple gain…
HYST	The Hysteresis block is a sim…
INT	The Integrator block is a sim…
INV	The inverter is a single-input,…
ISOURCE	
JKFF	The digital jk-type flip flop is …
LIMITER	The Limiter is a single input, …
MUL	This function is a multiplier bl…
NAND	The digital ‘nand’ gate is an n…
NOR	The digital ‘nor’ gate is an n-i…
OR	The digital ‘or’ gate is an n-in…
OSC	The digital oscillator is a hybr…
PDN	The digital pulldown resistor i…
PUP	The digital pullup resistor is a…
R2V	Node bridge from real to anal…
RGAIN	A gain block for event-driven

Simulate Real Eagle Schematics with Mixed Signal ngSpice

Version 1.3a, 2/4/2017, (c) 2012-2017 Uros Platise, http://www.isotel.eu/mixedsim

Run as: **run ngspice** [*outfile* [*sheet number* [*subckt pin name*]]]

The ngspice, http://ngspice.org, is a mixed signal simulator embedding spice3f5 (analog), xspice (mixed signal), tclspice (scripting), and allows inclusion of the Verilog-AMS models as well as simulation with the Verilog/VHDL via Yosys synthesis. The xspice adds over 40+ mixed signal analog/digital components to the basic spice. By using CodeModels that can be expanded to your custom models written in C.

Purpose of this ngspice script is to use it in a natural way with real circuits to avoid copying and redrawing parts of it for simulation purposes only.Netlists are extracted as top or as sub-circuits on detection of at least one sub-circuit port element from the ngspice.lbr.In this case script will generate a sub-circuit in a file with .mod extension. Otherwise schematics is extract as top-level circuit with .cir extension. One may specify a filename to be different with the first argument in a command line, and optionally it may select a sheet by its number to selectively export only part of the circuit. Both arguments are given when exporting a part of the circuit to create a sub-circuit. In such cases we would like that this circuit has different ports in spice subckt creation than the whole schematics. This is defined by the 3rd argument, to override the default SPICE-PORT name PINx, to something else, let's say our sheet 5 has a analog filter and we would like to evalute separately, so we name SPICE-PORTs as A1, A2, A3, .. and enter for the last argument the prefix: A

Transistors, mosfets, integrated circuits are treated in natural spice way: all primitive elements may be given extra model description, and integrated circuits are included as sub-circuits. So one component (eagle schematics) can be instantiated into the other circuit in a hierarchical way.

ChangeLog

Version 1.3a, 2/4/2017

- Added external circuit instantiation via Eagle module and port elements

/home/uros/Repos/Isotel/mixedsim.git/eagle/ulp/ngspice.ulp Date: 23/04/2017 23:39 Size: 35.0 kB

Figure 3.9: Eagle ngspice library provides a collection of xspice elements.

3.6 Summary

This chapter represents the base elements that have been purposely designed and used in the development of the new method, providing the following contributions to the open-source community:

- a new, simple PLATISE model, incorporated into the ngspice, and a slightly faster implementation of the coil with a bandwidth controllable parameter,
- integration of Verilog code via Yosys, and implementation of the supporting library,
- implementation of an ngspice code model for seamless firmware (C/C++) integration, and
- implementation of an advanced Eagle User Language Program (ULP) script with almost complete ngspice mixed signal library.

Further information with detailed examples are available at `http://isotel.org/mixedsim`.

Chapter 4

Platiše Flux Sensor

To date, no known element has been discovered that could directly measure a constant magnetic voltage drop on a magnetic material (resistance). So far, the only known method to observe the magnetic flux in a magnetic material is to make it non-constant by changing its amplitude or direction. In this respect, an active element analogous to a transistor in an electronic circuit would be required, capable of redirecting the fluxes inside a magnetic circuit, whereupon the resulting flux changes could be easily captured with a winding.

In this chapter, an innovative, patented [17] principle based on a flux redirection method is presented. Chapter 4.1 begins with the basic principle of operation. This is followed in Chapter 4.2 by the key active element, a so-called current controlled variable reluctance that completes the Platiše Flux Sensor in Chapter 4.3. Finally, Chapter 4.4 provides the principle of extracting DC/AC signals by means of the modulation and demodulation of the sensing signals. When describing the operation, we refer to a core with realistic parameters that was later built and evaluated. To this end, the same 26G material was used for building a core as described in Chapter 3.1.

4.1 The Concept of Flux Measurement

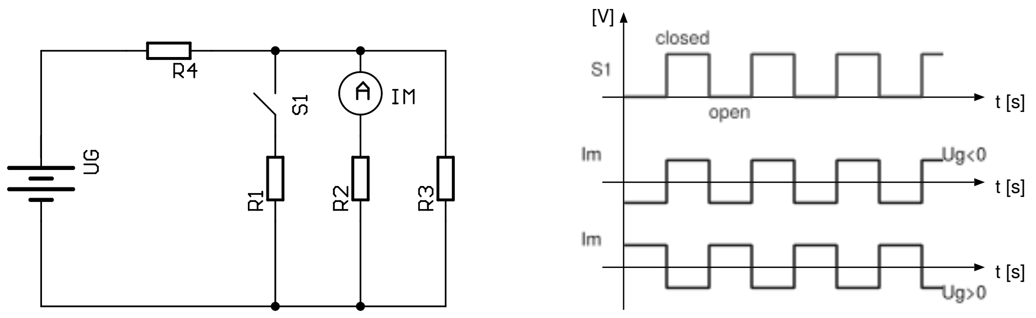

(**a**) Block diagram.

(**b**) Conceptual waveform.

Figure 4.1: The basic principle of constant (DC) magnetic flux measurement.

The working principle of the magnetic flux measurement is shown in Figure 4.1. The U_G generates magnetic flux via a “primary” path denoted by R_4 to the newly designed flux sensor represented by three branches, resistances R_1 and R_2, and some of the leaked flux, which is depicted by R_3. By altering the path of R_1, the flux through R_1 changes, as it does through R_2 and R_3. The resulting change of flux I_m can be observed as induced voltage $N\frac{\delta\phi}{\delta t}$ flowing through R_2. If the polarity of the incoming current and thus the flux changes, so does the output phase, as depicted by I_m in the chart.

The challenge therefore lies in creating a new basic element S_1 for magnetic circuits with a current controlled variable reluctance (CCVR). To avoid any ambiguity, it is important to note that variable reluctance has up to date been referred to motors and sensors, where the reluctance changes due to the mechanical movement of a part of a magnetic circuit. This is not the case with CCVR, where the reluctance is controlled by an electric current.

4.2 Current Controlled Variable Reluctance (CCVR)

Soft-magnetic materials $B(H)$ have non-linear characteristics and saturation properties, which is why an externally driven current may induce a magnetic force and drive the core into the region of saturation, close to or into points a or b as shown in Figure 4.2a. In these two final saturated points, the relative permeability is reduced down to $\mu_r \to 1$.

By using this non-linear property, the goal was to design an element that would create a self-closed magnetic loop $B(I_s)$ and would not leak away and interfere with the measured flux B_{dc} as shown in Figure 4.2b, which represents the first part of contribution C1.

CCVR is formed by opening a section in a magnetic material, creating a self-closed magnetic loop $B(I_s)$ that is excited by a balanced winding L_s (which produces equal electromotive forces) on both branches of the opening section. Such a winding L_s can be wired as an infinity sign or as two independent windings. By adding an electric current I_s into L_s in a symmetrically balanced core (with an ideal opening exactly in the center of the homogeneous magnetic material), the left and right branches of that magnetic material are actively being pushed closer to the saturation points a or b. Now, let us consider the following two cases to see how the CCVR element behaves:

- Non-excitated Core, in which $B_{dc} = 0$, with the effects of imbalanced magnetic structures and wiring.
- Excited Core, in which $B_{dc} \neq 0$, with the CCVR characteristics as a switch.

An illustration of magnetic flux distributions inside the CCVR for the above cases is represented by using a finite element method (FEM) simulation in the freely available tool FEMM[1]. We considered the same 26G material from Figure 3.2b and a toroid shape with an inner diameter of 13.2 mm, an outer diameter of 18.3 mm, a depth of 2.6 mm, an opening section of the diameter of 1.2 mm, I_s wires on the left and right sides of the core with direction in, and inside the opening with the direction out. The CCVR section of a described magnetic core is shown in Figure 4.3. As the target use of the CCVR is in a DC-CT transducer, the characteristics are described in relation to primary current I_p in ampere-turns [At], which induces B_{dc} and the controlling current I_s also in [At] of the (complete) winding L_s, which induces $B(I_s)$.

4.2.1 Magnetic Flux Distribution in a Non-Excitated Core

First, the behavior of the CCVR must be examined in the case of a non-excitated core with $I_p = 0$ A so $B_{dc} = 0$ and $I_s = 100$ mAt (mA-turns). Figure 4.4 represents the flux distribution of a perfectly balanced (symmetrical) structure. Such a balanced structure minimizes $B(I_s)$ leaking into the core, which in this particular case accounts 0.4 mT or 2.4 nWb compared to the flux density on the side branches of the CCVR of 160 mT or

---

[1] `http://www.femm.info`

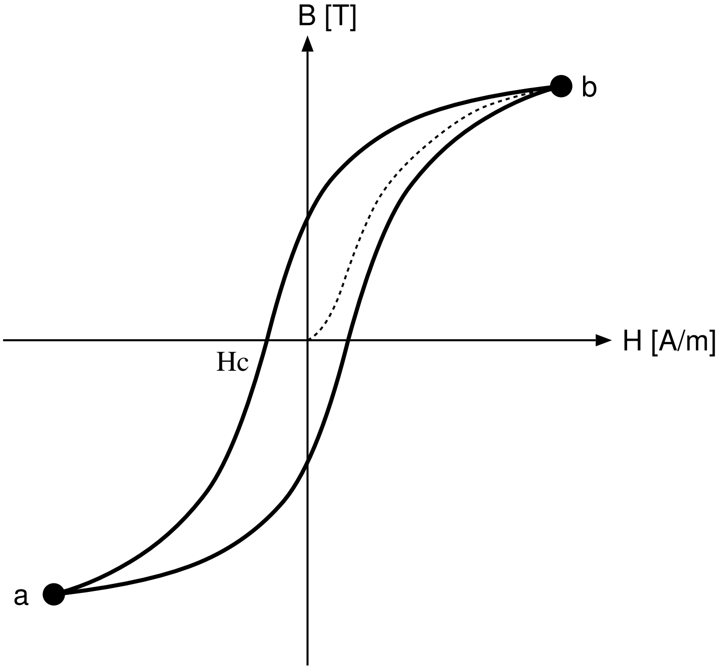

(**a**) Typical $B(H)$ hysteresis loop.

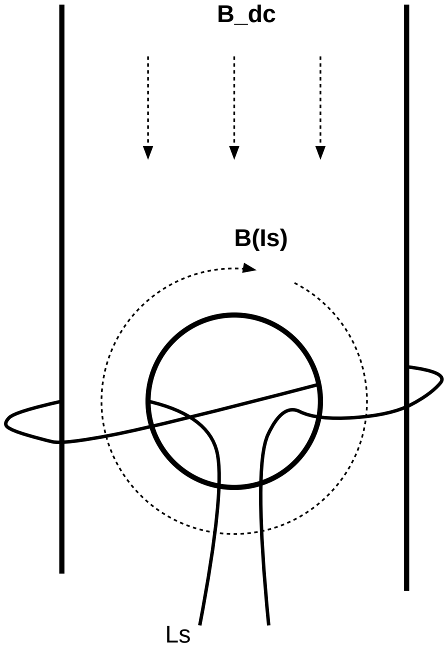

(**b**) Platiše CCVR "∞" winding.

Figure 4.2: Current controlled variable reluctance magnetic element.

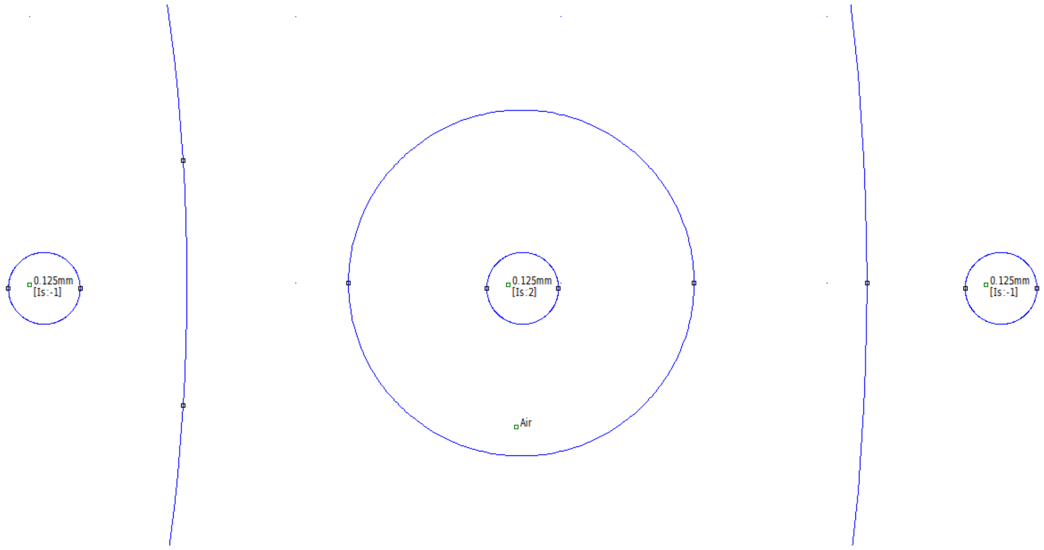

Figure 4.3: CCVR section on the right side of the toroid core as seen in Figure 4.4.

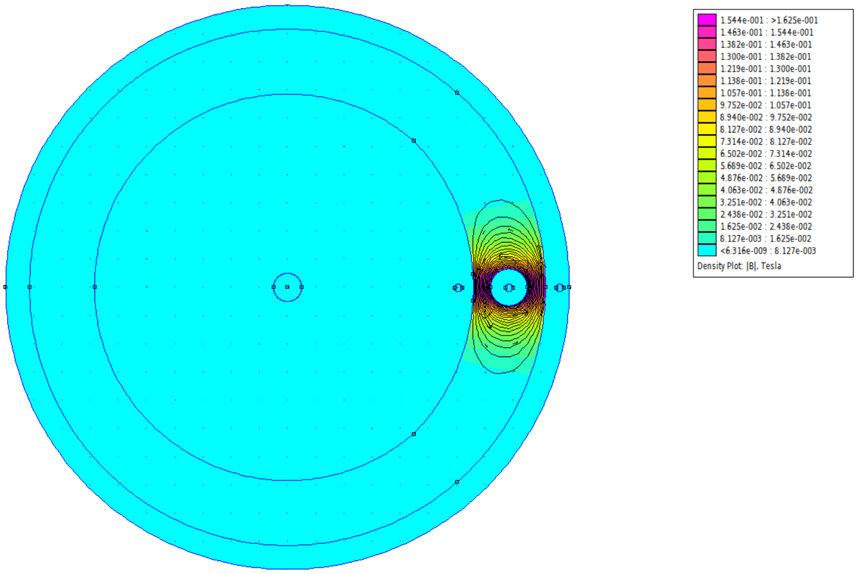

Figure 4.4: Magnetic flux densities around CCVR in a non-excitated core.

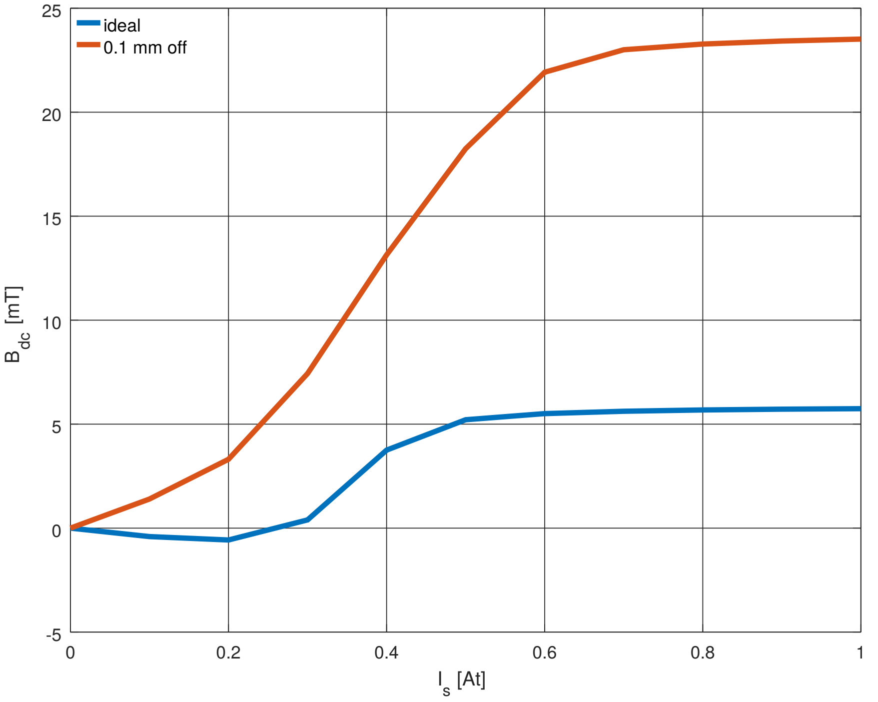

Figure 4.5: CCVR cross-talk (leak) from I_s to B_{dc} for a symmetrical core and with a 0.1 mm opening section displacement.

275 nWb. This shows that CCVR current I_s has a low impact on the primary and also compensation winding of a final DC-CT transducer.

CCVR is also prone to over-driving by excessive I_s currents, but even in such a case, $B(I_s)$ does not significantly leak into the core, as long as the CCVR is balanced.

Similarly, primary and secondary currents are basically invisible to the L_s winding. The characteristics of this leak, which is seen at the end in a DC-CT transducer as a cross-talk between the CCVR stimulus current I_s and the induced B_{dc}, appearing as unwanted noise at the output of the transducer, is shown in Figure 4.5. Figure 4.5 represents the most typical imbalance effect caused by the opening section displacement from the sides. For example, a 0.1 mm of opening displacement would produce approximately 8.6 nWb or 1.4 mT of leak to the core at $I_s = 100$ mAt, which would equal about 20 mA of a primary current. As shown in the same figure, what we consider fully symmetrically positioned openings in the toroidal core actually shows the characteristics of minor displacement due to the ratio between the inner and the outer diameter of the toroid, which is 72%. The effect can be compensated by intentionally displacing the opening section towards the outer diameter.

The second noticeable imbalance is caused by imperfect winding, especially at a low number of L_s turns. A higher number of turns that is manually imbalanced may, on the other hand, compensate for the anomalies caused either by the opening displacements or those arising from a non-homogeneous material structure, shape deformations during production, and micro-cracks that affect (reduce) permeability in parts of the material. Once the production capabilities have been determined, these parameters can be varied and simulated to understand the practical limits.

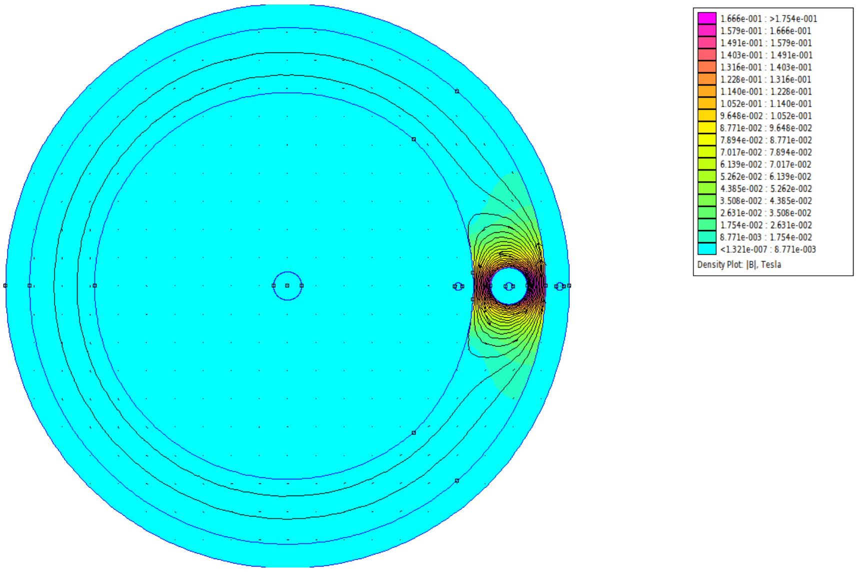

Figure 4.6: Magnetic flux densities around CCVR in an excitated core.

4.2.2 Magnetic Flux Distribution in an Excitated Core

Let us take a closer look at the behavior of the CCVR in the case of an excitated core assuming a constant primary current of $I_p = 100$ mA, which together with stimulus current $I_s = 100$ mAt in the center of the toroid, produces a magnetic flux of $\phi_{dc} = 44$ nWb or a magnetic flux density of $B_{dc} = 7$ mT. Assuming a symmetric structure, this flux halves to $\frac{\phi_{dc}}{2}$ to both sides of the CCVR and on one side of the opening, it adds up to 297 nWb or 0.175 T, while on the other, it subtracts to the 252 nWb or 0.125 T. The simulation results for this case are shown in Figure 4.6.

The effect of adding magnetic fluxes on one side keeps the path closed, but on the other side, the area in which magnetic fluxes are subtracting causes the CCVR to behave like a switch with a characteristic $B_{dc}(I_p, I_s)$ for a given simulation model shown in Figure 4.7. With the increasing primary current, all curves converge into the saturation point.

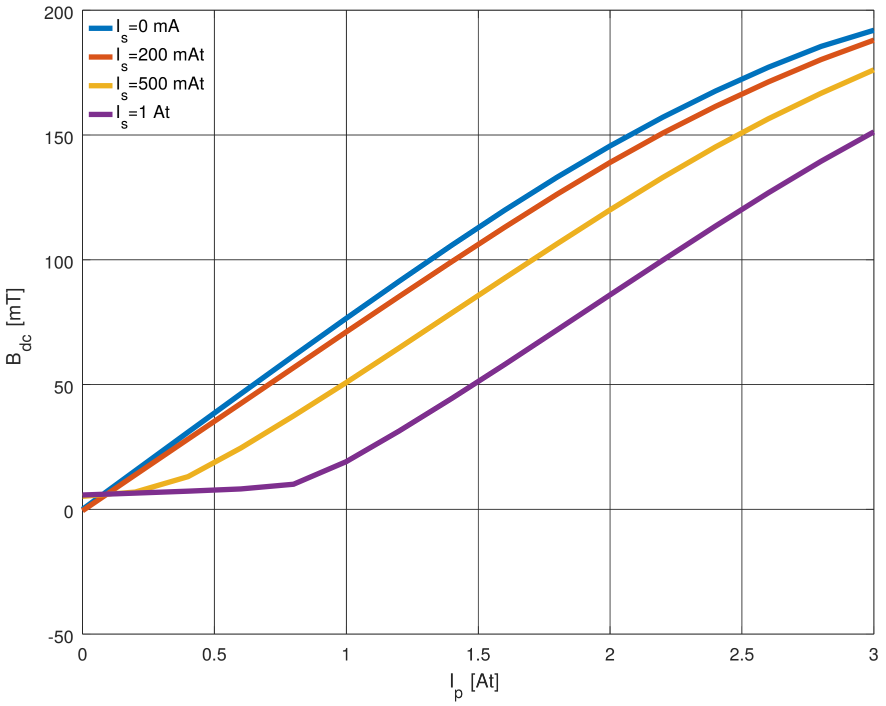

Figure 4.7: CCVR characteristic $B_{dc}(I_p, I_s)$ obtained with the FEMM simulator.

4.3 Complete Platiše Flux Sensor

Applying the functional CCVR as described in Chapter 4.2, we can now complete the core structure of the Platiše Flux Sensor as proposed in Chapter 4.1. A path R_2 as per Figure 4.9 was created to the gapless toroid core, shown in Figure 4.8, of practically the same dimensions as considered in Chapter 4.2. In particular, to create a new path for the R_2, an additional opening has been created with an additional winding L_m and magnetic flux (current I_m) in the center branch of the two openings, as shown in Figure 4.9. Due to the small dimensions of the ferrite core, the area was symmetrically enlarged and L_s, representing the path R_1 as per Figure 4.1, symmetrically placed on the side branches of the two openings. Figure 4.9 shows a completed core with a primary conductor and current I_p in the center and a zoom-in of the Platiše Flux Sensor L_s and L_m winding.

4.3.1 CCVR Characteristics

Figure 4.10 shows the CCVR cross-talk induced by the CCVR I_s to B_{dc} in the rest of the core, represented in Figure 4.1 as R_4. The impact is reduced compared to the CCVR only implementation shown in Figure 4.5 with a single opening due to the newly added bypass path R_2 between the two openings. In addition, simulations have also been performed for negative stimulus currents I_s to illustrate the symmetry of operation of the CCVR, as well as for a 0.1 mm displacement of one of the openings.

The CCVR characteristics for different CCVR stimulus currents I_s are shown in Figure 4.11. The B_{dc} generated by the primary current I_p is now squeezed by the CCVR from the R_1 path to the R_2. Therefore, the impact on B_{dc} vs. I_p at different CCVR stimulus levels I_s is reduced and almost negligible compared to the CCVR-only implementation shown in Figure 4.7. In addition, the simulations were also carried out for negative primary

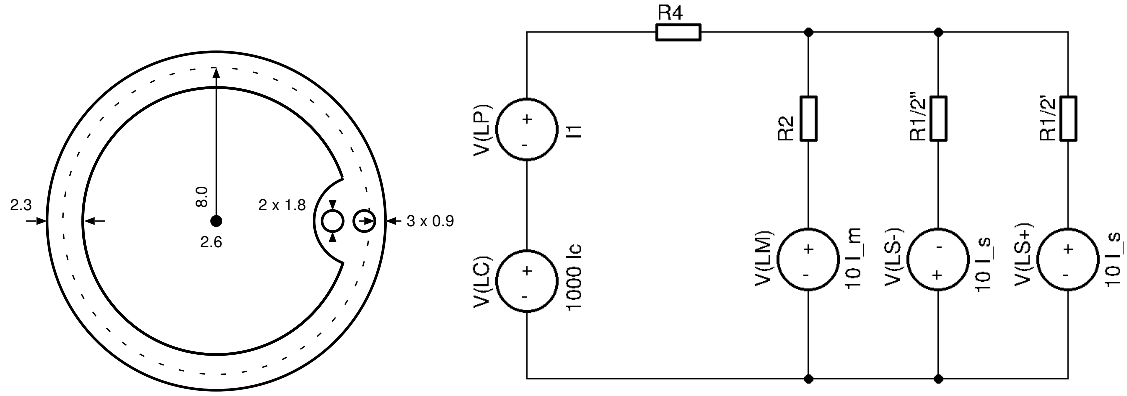

Figure 4.8: Platiše Flux Sensor on a toroid core and block diagram of windings L_s split into two branches R_1 and the new measuring winding L_m in the R_2.

currents I_p to illustrate the symmetry of the operation.

The low impact of the CCVR operation on the B_{dc} ensures the low noise operation of the DC-CT transducer.

4.3.2 Sensor Characteristics and Sensitivity

The key parameter of interest for a detailed characterisation of the Platiše Flux Sensor is the flux density in the measuring path R_2 at different CCVR stimulus currents I_s and primary currents I_p. By alternating the I_s current, depicted by a symbolical switch S1 in Figure 4.1, the flux density in the measuring path R_2 alters. These changes are easily captured by a measurement winding $V_m = N_m \frac{\delta\phi_m}{\delta t}$, where V_m is an induced voltage due to the changing flux $\delta\phi_m$ through the measuring branch R_2 or area enclosed by L_m, and N_m is the number of turns of the L_m, also referred to as a gain factor of the measurement winding. The sensitivity of the sensor is therefore:

$$S = \frac{1}{I_p} N_m \frac{d\phi_m(I_p, I_s)}{dt}|_{I_s=M(t)} \text{ [V/A]} \tag{4.1}$$

where I_s is following an arbitrary modulation function $M(t)$. The sensitivity S is therefore proportional to the switching speed, or period T_s of the $M(t)$, the CCVR stimulus current I_s, gain N_m, and naturally dependent of the core material, design, and implementation. The $\phi_m(I_p, I_s)$ flux is in a non-linear relationship to I_p over the entire range, however DC-CT typically operates in a null method in which the limited area sensitivity can be seen as quasi-linear.

The two flux arrangements with slightly higher currents (for illustration purposes) $I_p = 1$ A and $I_s = 0.2$ A and $I_s = -0.2$ A are shown in Figure 4.12. As per the simulation, given this particular core construction with the openings and L_s positioned aside, a portion of flux closes through the inner segment, the L_m. It creates a so-called cross talk C between the L_s and the L_m:

$$C = \frac{1}{I_s} N_m \frac{d\phi_m^{+|-}(I_p, I_s)}{dt}|_{I_s=M(t)} \text{ [V/A]} \tag{4.2}$$

The cross-talk C, even-though it may appear small, it does typically induce a higher signal at the L_m compared to the I_p redirected either with a positive ϕ_m^+ or negative ϕ_m^- change. A Signal to Noise Ratio (SNR) defines the required dynamic range of the demodulator and is given as $SNR = (S/C)^2$ or $SNR = 20\log_{10}(S/C)$ in dB.

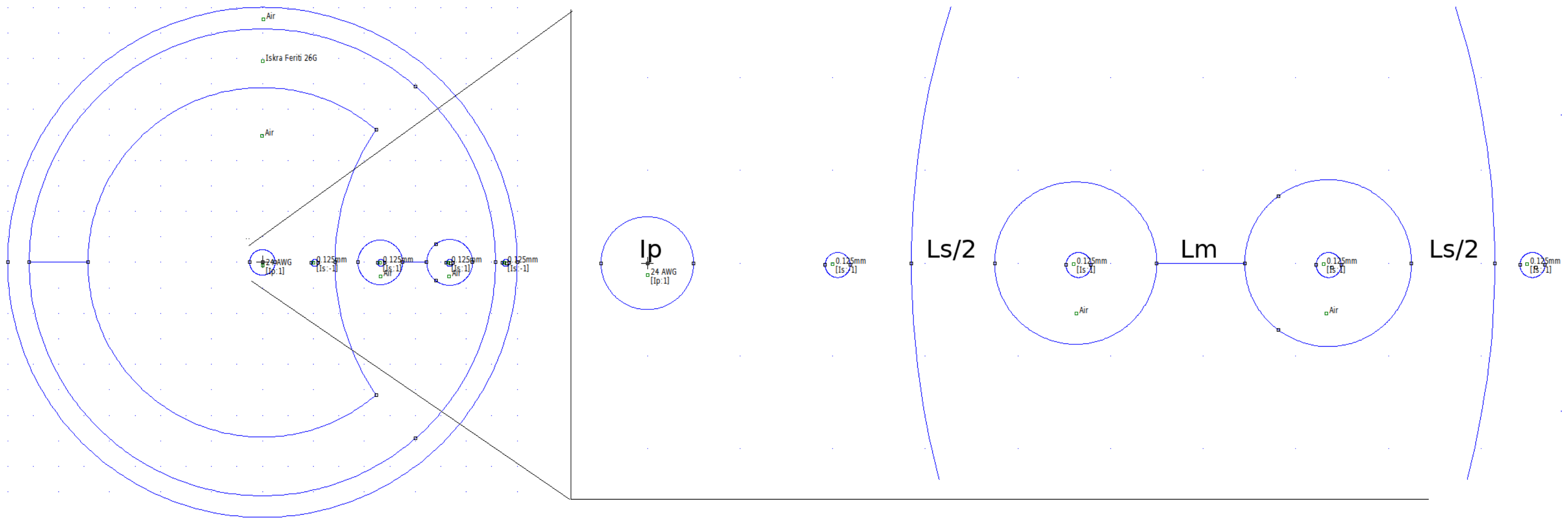

Figure 4.9: Platiše Flux Sensor on a toroid core from Figure 4.8 with CCVR L_s, measuring L_m and primary current I_p.

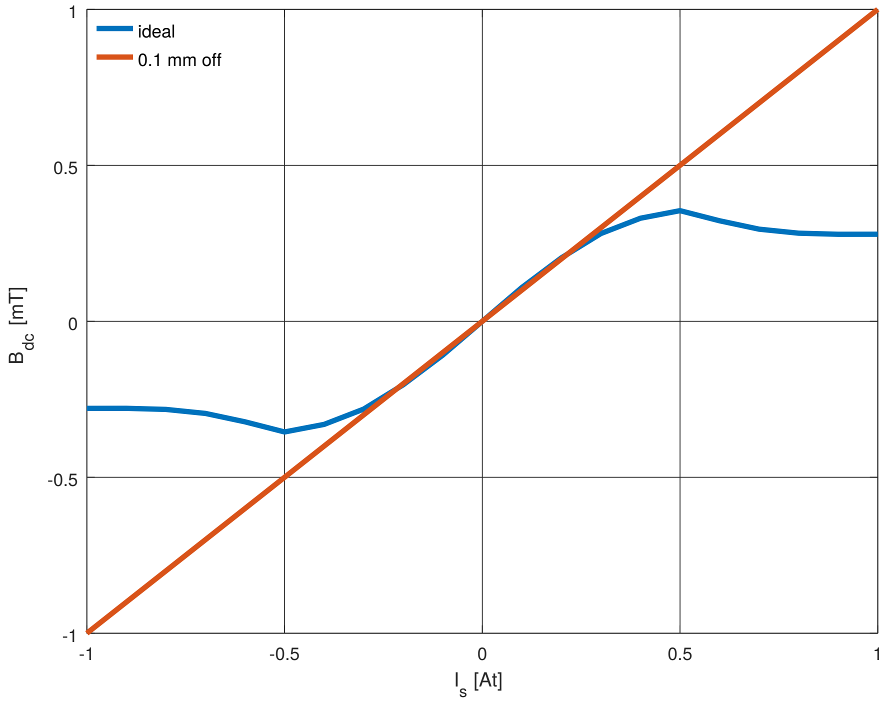

Figure 4.10: CCVR cross-talk (leak) of a quasi symmetric (balanced) structure in I_s to B_{dc} from the Platiše Flux Sensor and with 0.1 mm of one opening section displacement (asymmetry).

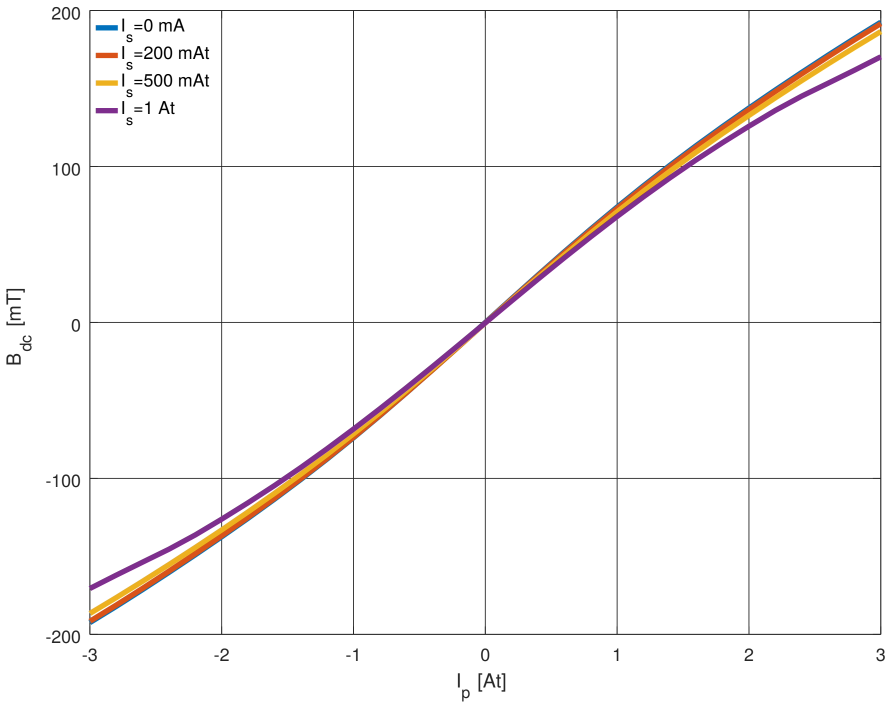

Figure 4.11: CCVR Characteristics $B_{dc}(I_p, I_s)$ in a core with a Platiše Flux Sensor.

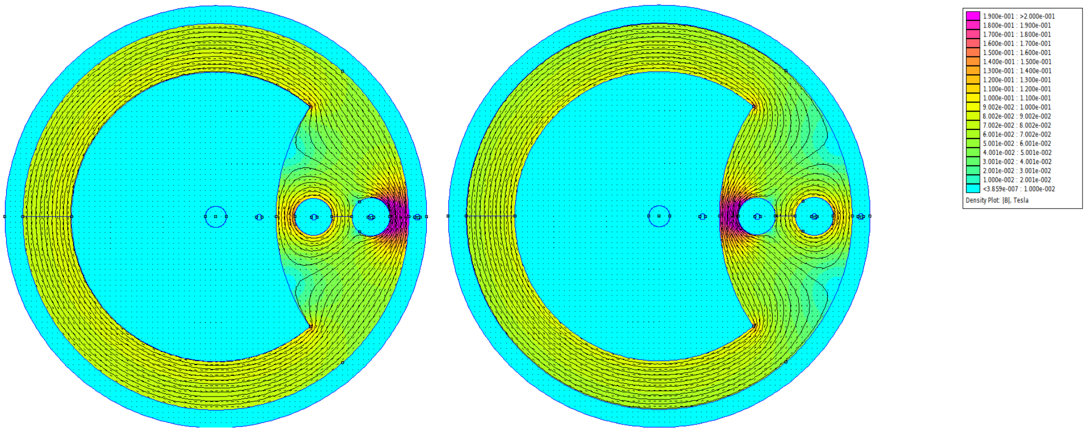

Figure 4.12: Flux distribution inside the Platiše Flux Sensor at $I_p = 1$ A and $I_s = \pm 200$ mAt.

The characteristics of magnetic flux ϕ_m obtained with the FEM simulation for a limited range of $I_p = \pm 0.5$ A and $I_s = \pm 0..300$ mAt are shown in Figure 4.13a for positive and Figure 4.13b for negative I_s currents. Higher currents are not of practical interest for DC-CT operating in a null method. Looking at $I_p = 0$ At and various I_s currents, a cross-talk is clearly observed that is positive for $I_s > 0$ and negative for $I_s < 0$. Additionally, dead points at about $I_p = \pm 100$ mA are observed in either direction, at which point the magnetic flux generated by the I_s cross-talk and the I_p cancels. These severe effects can be easily canceled by alternating the current $\pm I_s$, which subtracts the cross-talk C and doubles the sensitivity of the sensor S.

4.3.2.1 An example of sensitivity and cross-talk calculation

The following subchapter presents an example of sensitivity and cross-talk calculation (estimation) as per Eqs. (4.1) and (4.2), the characteristics of ϕ_m from the simulation plots shown in Figures 4.13a and 4.13b, and the readings at $I_s = \pm 50$ mAt (10 turns on each side with 5 mA stimulus):

- $\phi_m^0(I_p = 10 \text{ mAt}, I_s = 0 \text{ mAt}) = 1.909$ nWb
- $\phi_m^+(I_p = 10 \text{ mAt}, I_s = 50 \text{ mAt}) = 2.865$ nWb
- $\phi_m^-(I_p = 10 \text{ mAt}, I_s = -50 \text{ mAt}) = 0.997$ nWb

then:

- flux change in the positive $d\phi_m^+$ direction is $\phi_m^+ - \phi_m^0 = 0.956$ nWb
- flux change $d\phi_m^-$ in the negative direction is $\phi_m^- - \phi_m^0 = -0.912$ nWb
- combined flux change: $d\phi_m^+ + d\phi_m^- = 44.6$ pWb

At $N_m = 10$, a CCVR driven by a triangular modulation signal with rising and falling edges of $dt = 2$ μs and a period of 250 kHz results in the sensitivity:

$$S(I_p) = N_m(d\phi_m^+ + d\phi_m^-)/dt/I_p = 22 \text{ mV/At} \tag{4.3}$$

The cross-talk calculated in the worst positive direction is:

$$C(I_s) = N_m d\phi_m^+/dt/Is = 95 \text{ mV/At} \tag{4.4}$$

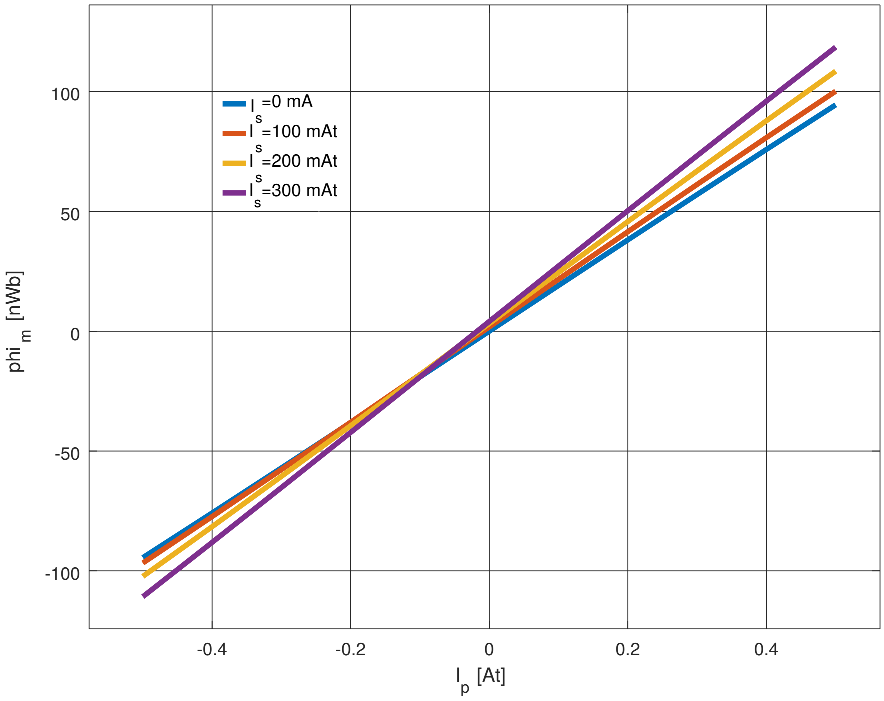

(**a**) $I_s \geq 0$

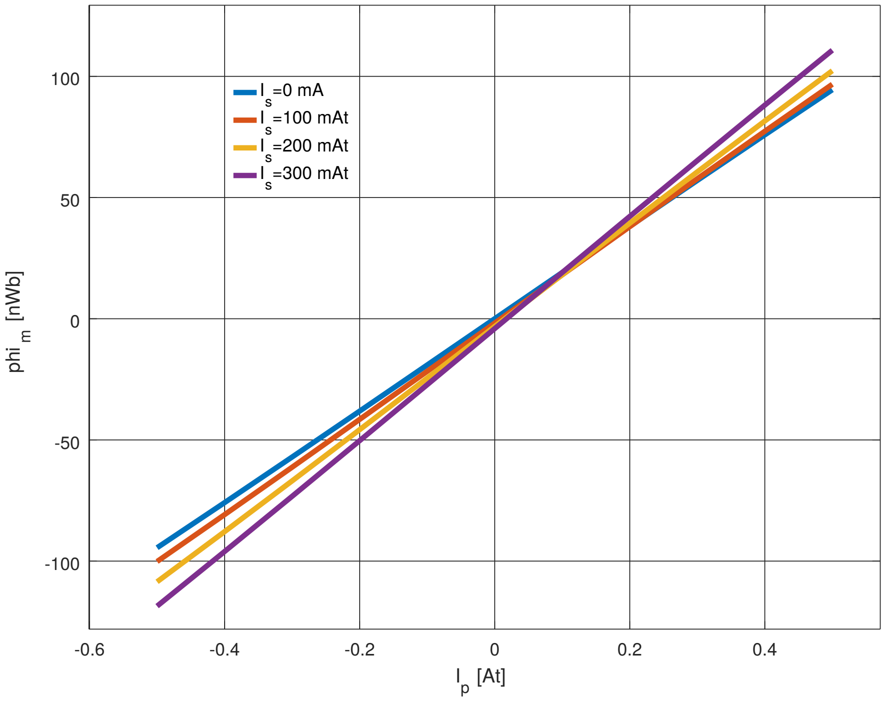

(**b**) $I_s \leq 0$

Figure 4.13: Platiše Flux Sensor characteristics for $\phi_m(I_p, I_s)$.

A triangular modulation signal provides a constant first derivative $d\phi/dt$ and thus easy calculation of the sensitivity. Low-pass filtered square-waves can be used equally well in the most simple implementations, besides a sine wave for the lowest noise performance.

4.3.3 Hysteresis Errors and Degaussing

So far, the hysteresis of a magnetic material has been ignored in the discussions and derivations. It does not significantly impact the performance of the CCVR and the sensor, however it does significantly impact the offset error, and it remains in the core after the core has been magnetized. Magnetisation may arise from the non-homogeneous distribution of the primary conductor magnetic fields due to the non-ideal conductor position, and from surrounding objects that disturb the distribution of a magnetic field around the primary conductor, or it may occur due to transients responses in which a zero-flux feedback loop responds too slowly, or due to overloads in which a zero-flux closed-loop is unable to compensate the excessively high primary currents. Overloads typically represent the highest stress on the magnetic material.

A simple worst-case estimation of measurement error due to the hysteresis effects can be obtained from the coercivity parameter H_c for a given material and the effective length l_e of a gapless core and the number of primary turns N_p:

$$I_{offset} = \frac{1}{N_p} \cdot H_c \cdot l_e \tag{4.5}$$

For material 26G by Iskra Feriti, the data-sheet specifies that $H_c \approx 12$ A/m; for the given core with an effective length $l_e = 50$ mm, and $N_p = 1$, this yields a theoretical maximum offset of 0.6 A. However, due to the opening sections and narrower paths, these saturate before the rest of the core, effectively reducing the worst case offset. By using high permeability materials, H_c reduces down or below 1 A/m, effectively reducing the worst case possible offset in the range of and below 50 mA referred to input (RTI). Note that as permeability is affected by the temperature, so is the H_c and the worst case corresponding offset. Lower amp sensors may use several primary turns N_p for additional reduction of the offset.

Degaussing is an approach to resetting the core remnant magnetic field. One possible solution is to apply a current of the form $\sin(\omega t) \cdot e^{-\frac{t}{\tau}}$ to the core, typically through the compensation winding and triggered on start-up or upon the detection of core overloading. Such a technique effectively reduces offsets down to the level of mA RTI.

4.4 Modulator and Demodulator

In sensitivity Eq. 4.1, it has been noted that the stimulus current I_s can be modulated with an arbitrary modulation function $M(t)$ that carries the B_{dc}, i.e., its DC and also AC magnetic flux information. Modulation and demodulation can be best described on a square wave signal as in Chapter 4.4.3 below, however practical implementations may use rise-time limited or low-pass filtered square waves, triangular, sine wave, and other shapes.

4.4.1 Principle of Operation

For small primary and stimulus currents $I_p, I_s < 100$ mAt, the Platiše Flux Sensor can be assumed to be quasi-inear. For the modulation $M(t)$ being a periodic function with the period of T_s, the induced voltage V_m on the measuring winding L_m is produced by combining Eq. 4.1 and Eq. 4.2:

$$V_m(t) = S \cdot I_p(t) \cdot |M(t)|' + C \cdot I_s \cdot M(t)' \tag{4.6}$$

This is a kind of amplitude modulation (AM), a superposition of the $I_p(t)$ modulated by an absolute value of the first derivative of the absolute value $|M(t)|'$, due to the characteristics shown in Figure 4.13, and a cross-talk between the I_s and ϕ_m proportional to the amplitude of the I_s.

We are interested in the auto-correlation function between the stimulus and the response given by:

$$R_{xx}(V_m(t), |M(t+t_{dly})|') \tag{4.7}$$

and particularly in the time instance t_{dly} where the R_{xx} reaches its maximum. The t_{dly} accounts for various delays along the path and non-ideal coupling with the core. The optimal demodulation then equals:

$$V_p(t) = V_m(t) \cdot |M(t+t_{dly})|' \tag{4.8}$$

For a symmetrical function, the $M(t)$ signs for $M(t)'$ and $|M(t)|'$ differ when $M(t) < 0$, which results in cancelling the cross-talk C in Eq. (4.6) over the exact multiples of period T_s. What remains is the left signal part only:

$$V_p(t) = S \cdot \Bigg(I_p(t) \cdot |M(t)|' \Bigg) \cdot |M(t+t_{dly})|' \tag{4.9}$$

Simplified demodulators may have reduced multiplication to a simple +/- operator denoted by a sign:

$$V_p(t) = S \cdot \Bigg(I_p(t) \cdot |M(t)|' \Bigg) \cdot \operatorname{sign}\Bigg(|M(t+t_{dly})|' \Bigg) \tag{4.10}$$

For a symmetric and periodic function $M(t)$, whose derivative has a single maximum and minimum, demodulation simplifies to a simple square wave of frequency $2f_s$:

$$V_p(n) = \int_{t=(n-1)T_s}^{nT_s} V_m(t) \cdot \operatorname{sign}(\sin(4\pi f_s(t+t_{dly})) = G_m \cdot S \cdot I_p(nT_s) \tag{4.11}$$

where n is the sample count of sample period T_s. The response of a demodulated voltage output is therefore directly proportional to the primary current I_p and the gain of the modulating function $M(t)$ integrated over the interval T_s is denoted by G_m.

4.4.2 Resonant Frequency

The T_s and f_s are the period and the frequency of the modulation function $M(t)$. They also denote the sample interval, or mixer frequency with which $I_p(t)$ is mixed. Therefore, the resulting $V_p(t)$ contains mixer products of the $\sin(2\pi f_p t)\sin(2\pi f_s \cdot t)$ for each frequency f_p in the set of spectrum of the primary current I_p. The mixer therefore generates output frequencies of $f_s \pm f_p$, with down conversion $|f_s - f_p|$ assuming that the $V_m(t)$ is low-pass filtered. When f_p is approaching f_s from either side, $f_p > f_s$ or $f_p < f_s$, it begins to produce a very low frequency demodulated signal which may interfere with the DC-CT compensation regulator. When f_p equals f_s, the output is theoretically a constant and it represents a resonant frequency of the sensor. If $V_m(t)$ is not low-pass filtered, higher frequency products exist that lead to the same condition. For a symmetrical function $M(t)$ of a period T_s, the absolute operator $|M(t)|$ effectively doubles the sampling frequency to $2f_s$.

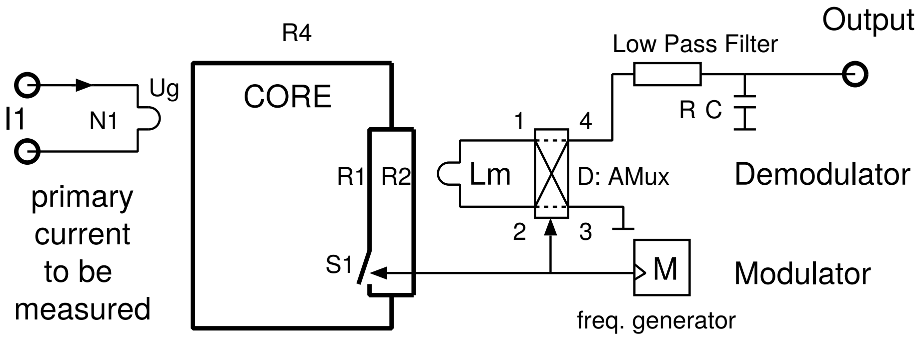

(**a**) Block diagram

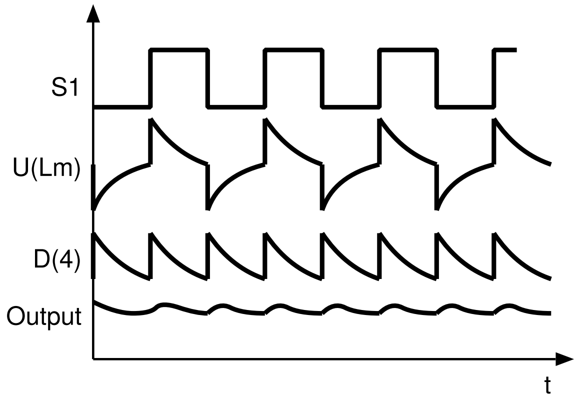

(**b**) Waveform diagram

Figure 4.14: Concept of the Platiše Flux Sensor DC measurement.

4.4.3 Minimal Control Circuitry

Figure 4.14a shows a block diagram of the hypothetical minimal control circuitry required for the operation of the Platiše Flux Sensor consisting of:

- a modulator M in the form of a simple digital clock generator of a duty cycle 50%:50% providing asymmetric modulation function $M(t)$ where $I_s \geq 0$ is driving L_s,
- an analogue multiplexer AMux as demodulator D synchronized to the modulator, in which two states with pairs (1–4, 2–3) and (1–3, 2–4) operate as a ± 1 sign mixer,
- a low pass filter with a time constant larger or at least equal to T_s used to remove glitches and transients sensed by L_m and demodulated by D.

Let us review the operation of the circuitry together with the core assuming a conceptual waveform as shown in Figure 4.14b, with an output voltage directly proportional to the primary current of interest I_1. For the sake of simplicity, let us consider that a primary current I_1 is generating a constant flux in the core. The CCVR denoted in Figure 4.14a as S_1 then redistributes this constant flux among paths R_1 and R_2 so that its changes get captured by L_m and demodulated. R_1 and R_2 are typically significantly smaller than R_4 and since R_2 does not change, the alteration of the resistance in the R_1 path does not significantly impact the flux magnitude changes in R_4. A low-noise operation is ensured by the parallel branch R_2, the closed magnetic loop path of the CCVR in R_1, and a bandwidth-controlled variable reluctance control current driver. Changing the direction (sign) of I_1 produces a 180 degree phase shifted $U(L_m)$, but of an equal signal pattern, and the resulting output at $D(4)$ is rectified as negative in the amplitude. The practical modulator and demodulator frequencies in such control circuitry can go up to $T_s = 500$ kHz or more.

4.5 Verification

4.5.1 Core Design

The flux distributions and the theoretical characteristics of the CCVR and the Platiše Flux Sensor have been obtained by using the FEM simulation. However, a FEM simulation is rather slow and therefore unsuitable for further verification of the principle of operation and development of DC-CT. For this purpose, an ngspice model of said core design was built by using the magnetic circuits and models derived in Chapter 3. In the following verification, we consider material 26G by Iskra Feriti. According to the geometry shown in Figure 4.8 and Figure 4.9, a simplified electrical model has been built as shown in Figure 4.15 and the generated ngspice circuit in Listing B.1.

The dashed lines represent a simplified magnetic equivalent circuit and the solid lines the electric connections with the windings, the I_p and I_s test current generators and termination resistors. The model follows the concept from the basic principle of the DC flux measurement depicted in Figure 4.1, where R1 is split among the paths with magnetic resistances A1A[2] and A1B, R2 is represented by A2, R4 by A4, and R3 is simply neglected. In this simplified model, a cross-talk is simulated by a slight displacement of one branch, the A1B, by 0.2 mm.

Figures 4.17 and 4.19 show the flux through the L_m under the same conditions as in the example in Chapter 4.3.2.1 for primary current $I_p = 10$ mAt DC and triangular stimulus current $I_s = \pm 50$ mAt of period 250 kHz, shown in Figure 4.16.

Figure 4.17a shows the flux of an ideal core without theoretical cross-talk. Comparing this simulation to the example from Chapter 4.3.2.1, whose readings were done only for two extreme points, the simulation also shows a non-linear relationship between the stimulus current and the flux, shaping it into a quasi half-sine wave. The maximum flux change can be directly read out from the plot. The first readout is considered as a positive change $d\phi^+$, the rising edge of the I_s between the first 1 μs until 2 μs, and yields about 23 pWb. The second negative change $d\phi^-$ on the falling edge of the I_s between 3 μs until 4 μs yields the same amount. Comparing the sum of 46 pWb with the FEM simulation from Chapter 4.3.2.1, whose combined flux change summed to 44.6 pWb, the models sufficiently match. Figures 4.17b and 4.18 show the voltage induced by the flux in the L_m winding, measured on R5, for positive and negative $I_p = \pm 10$ mA, representing how the sign of the I_p is encoded into the phase of the induced voltage in the L_m winding.

In Figure 4.19a, a displacement of 0.2 mm is used to compensate for the asymmetry of quasi-symmetrical openings on a toroid core. The simulation yields a cross-talk of about the same amplitude as obtained with the FEM simulation in Chapter 4.3.2.1. Due to the relatively low SNR, the signal cannot be visually detectable from this plot. However it can be noticed in Figure 4.19b showing the voltage induced in the L_m winding, where it is loaded on the top of the I_s cross-talk carrier signal. This same cross-talk is also induced in primary winding according to the ratio of turns between the primary and the L_m winding, reduced by the area of the magnetic core of the winding L_m compared to primary winding L_p, in this case for approximately a factor of 3. For this reason, having symmetrically positioned openings is one of the key parameters in achieving high performance implementations.

---

[2] The first A stands for Xspice Core Code Model.

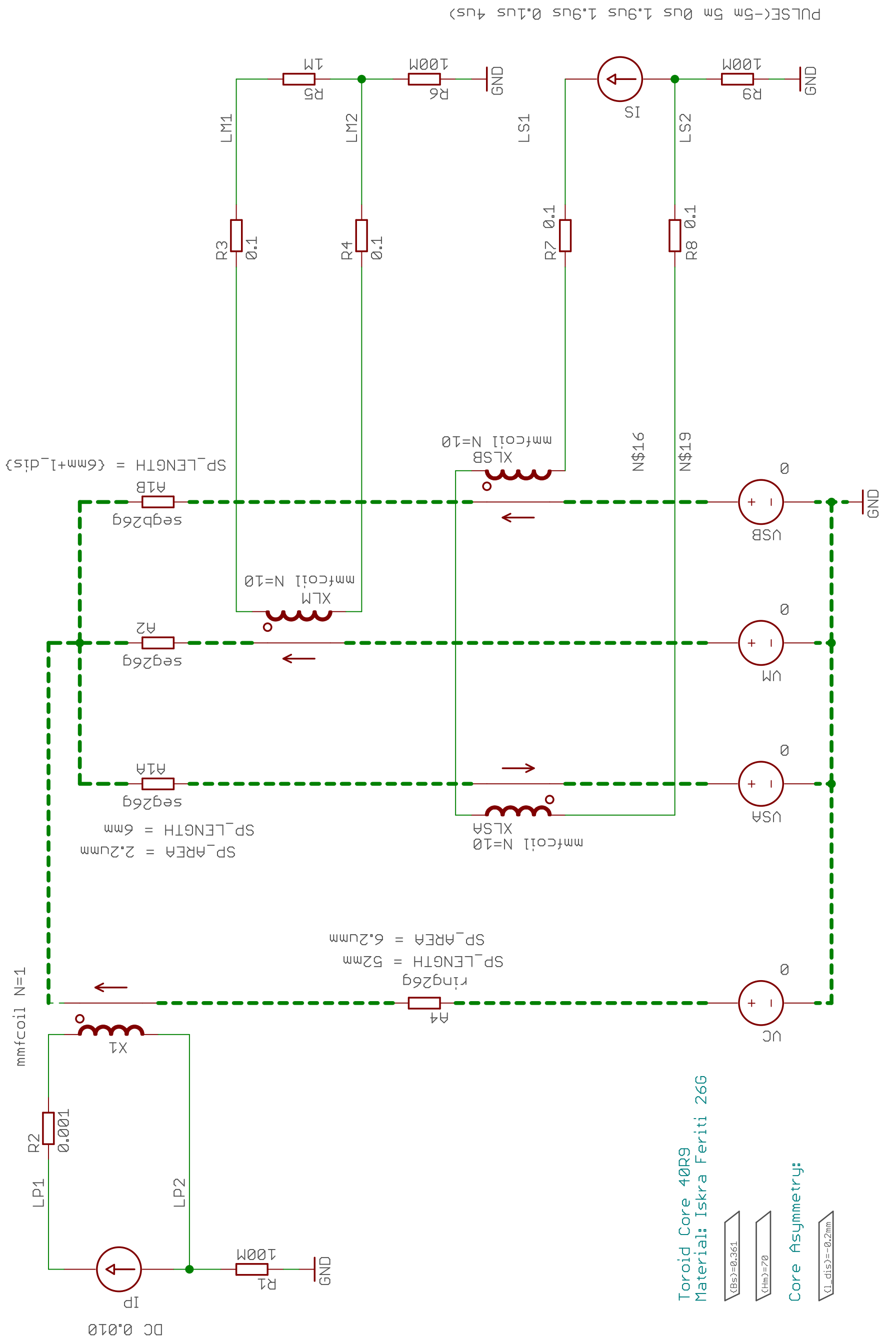

Figure 4.15: Electrical model of the Platiše Flux Sensor on a toroid core, see Listing B.1.

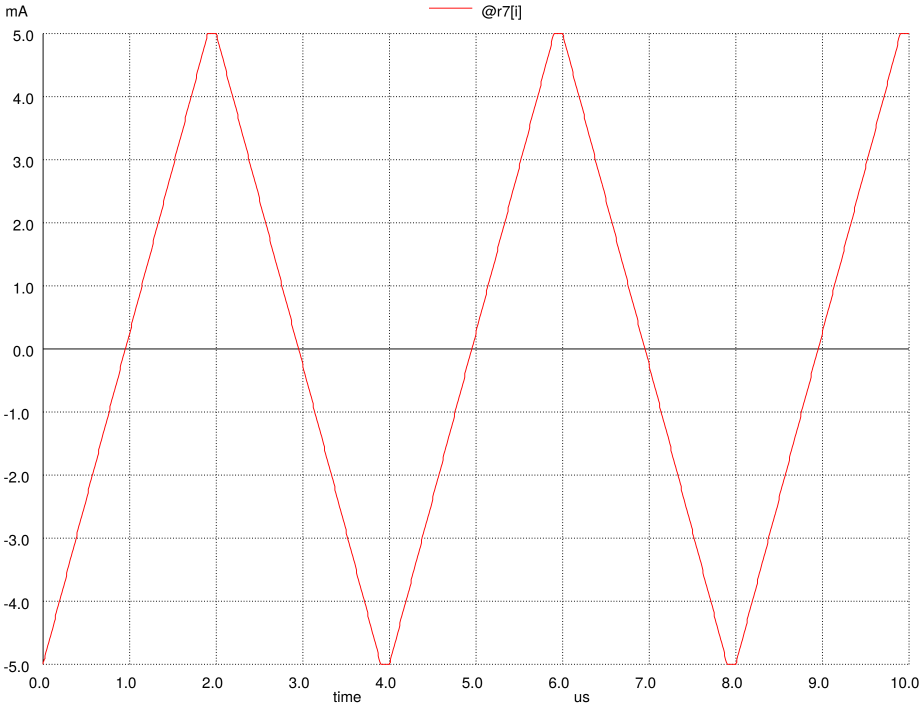

Figure 4.16: Stimulus current I_s, measured on R7.

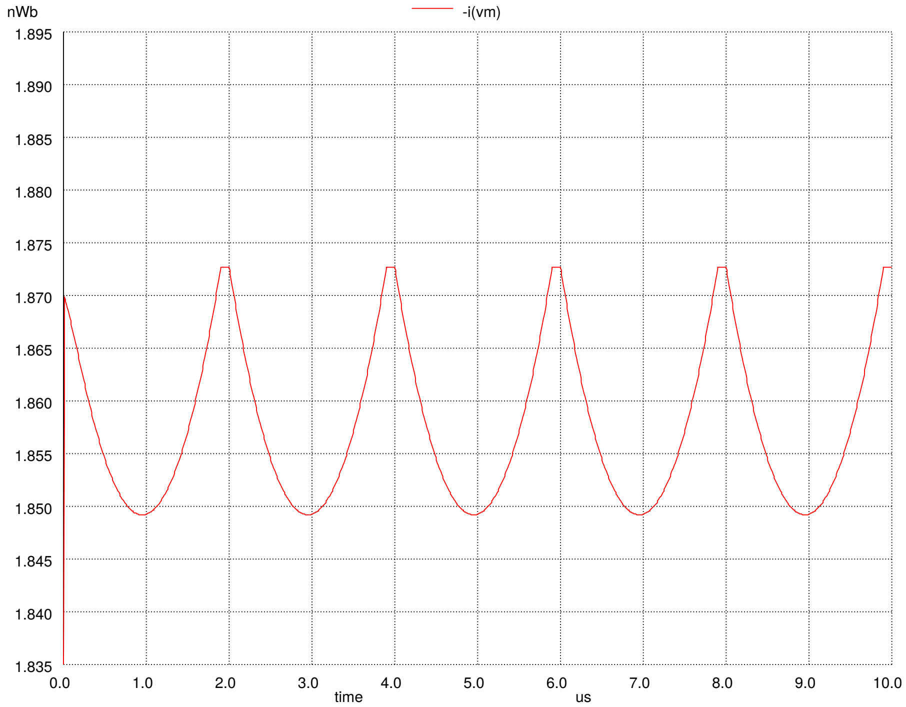

(**a**) L_m flux, measured on Vm.

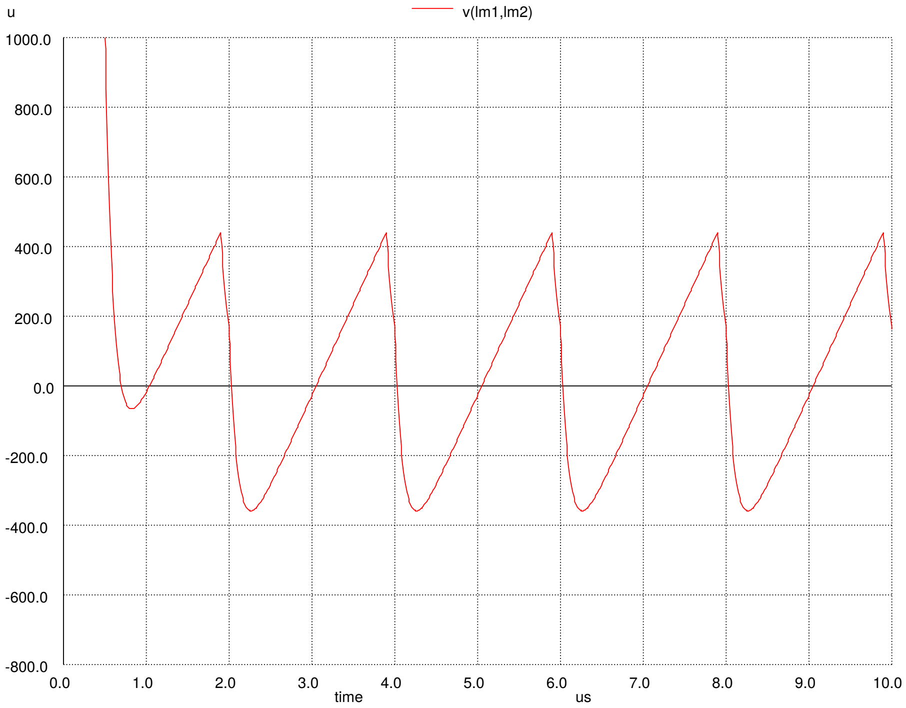

(**b**) $V(Lm1, Lm2)$ voltage, measured on R5.

Figure 4.17: Simulation Results of the Platiše Flux Sensor Core Model from Figure 4.15 and ideal symmetrical openings without crosstalk.

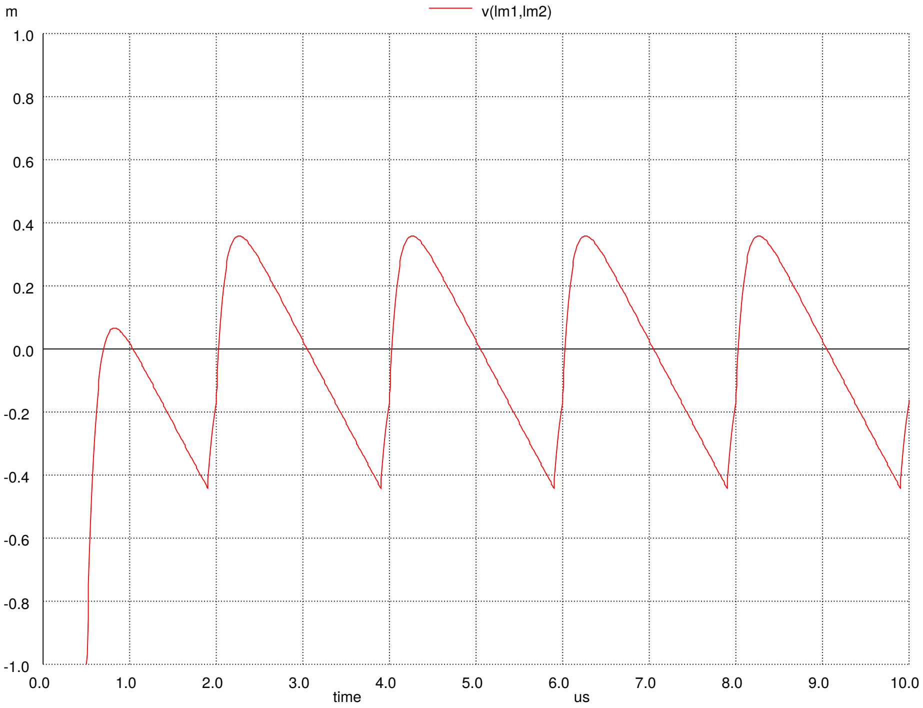

Figure 4.18: $V(Lm1, Lm2)$ voltage, measured on R5 for negative I_p.

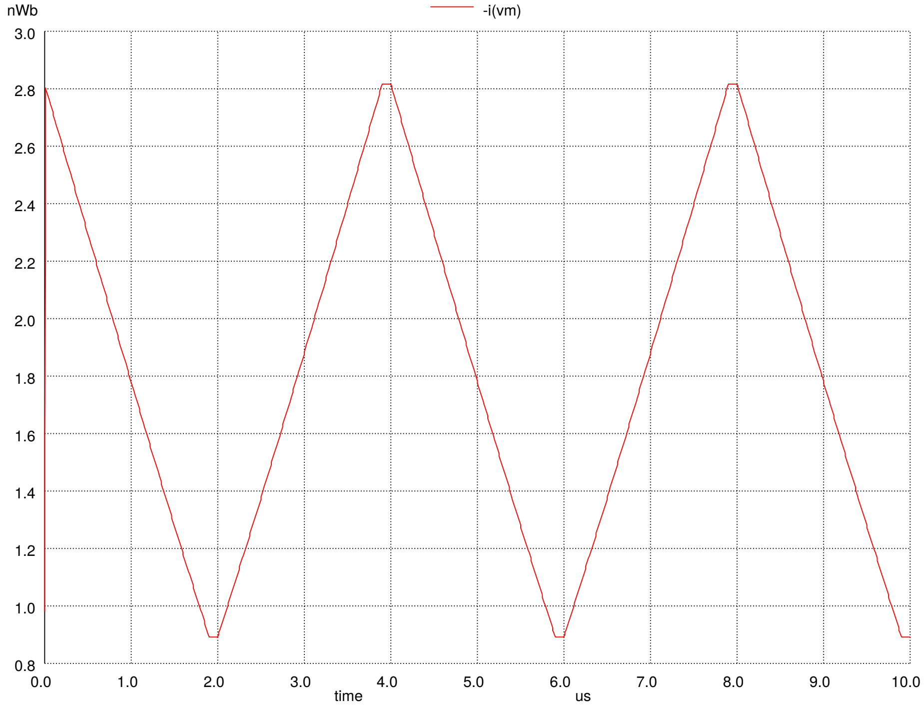

(**a**) L_m flux, measured on Vm.

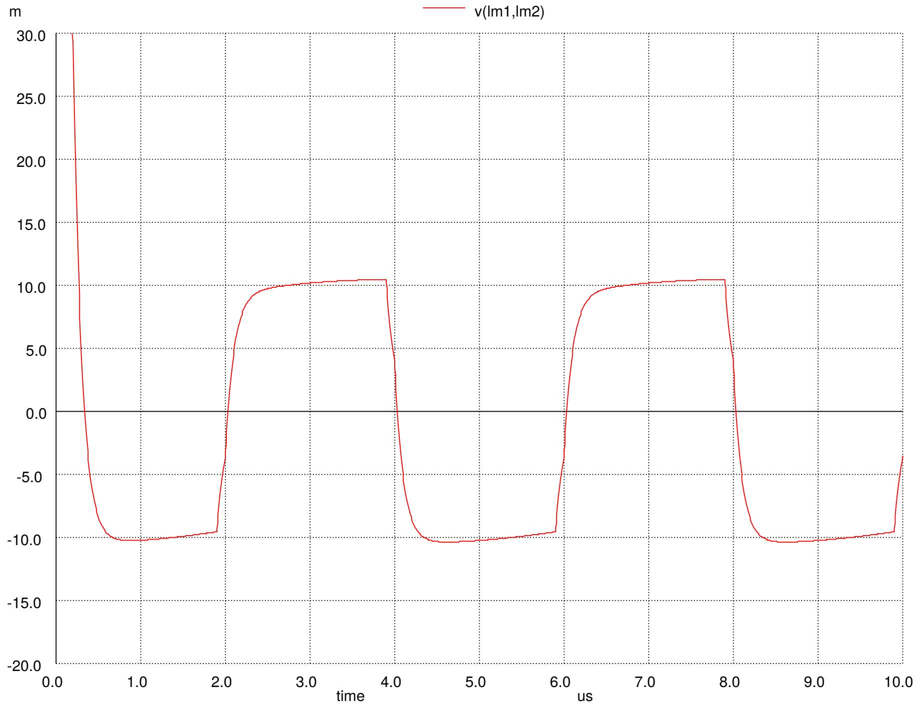

(**b**) $V(Lm1, Lm2)$ voltage, measured on R5.

Figure 4.19: Simulation Results of the Platiše Flux Sensor Core Model from Figure 4.15 for quasi-symmetrical openings with a cross-talk, simulated by a displacement of the branch by 0.2 mm.

4.5.2 Sensor, Modulator, and Demodulator

In the following we assume the same triangular modulation function $M(t)$ as shown in Figure 4.16. This modulation function and its first derivative for the n-th period can be expressed as follows:

$$M(t) = \begin{cases} k_{tri} \cdot (t - nT_s), & nT_s \leq t < (n+0.5)T_s \\ k_{tri} \cdot ((1-n)T_s - t), & (n+0.5)T_s \leq t < (n+1)T_s \end{cases} \tag{4.12}$$

$$M(t)' = \begin{cases} k_{tri}, & nT_s \leq t < (n+0.5)T_s \\ -k_{tri}, & (n+0.5)T_s \leq t < (n+1)T_s \end{cases} \tag{4.13}$$

The first derivative of $M(t)$, when saturated within the [+1, -1] boundaries, converts to a simple sign (symmetric square wave) demodulator function as presented in Chapter 4.4.3. Figure 4.20, which complements Figure 4.15, has added:

A5 a multiplier that calculates $M(t)^2$ replaces $|M(t)|$,

A1 a derivative with [-1, +1] boundary limits, the output that provides the demodulating function,

A3 a mixer that provides V_p as per Eq. 4.10

R11-C1 a 1st order low-pass filter that provides filtered result V_{pf}.

The simulation results as follows:

Figure 4.21a shows the modulating triangle $M(t)$ and the demodulating function $sign(|M(t)|')$

Figure 4.21b shows the demodulating function $sign(|M(t)|')$ and the $V(Lm1, Lm2)$ voltage under the same condition from the previous chapter, shown in figure Figure 4.19b at $I_p = 10$ mA,

Figure 4.22 shows the demodulated output VPF at $I_p = 10$ mA, yielding a sensitivity of about 20 mV/A, comparable with the FEM results in Chapter 4.3.2.1.

Figure 4.20, and ngspice generated Listing B.2, in addition includes a PULSE generator on the primary side to illustrate the AC performance. To overcome the cross-talk ripple at the VPF output, the integration period should equal the stimulus current period. For the sake of simplicity, the displacement was reset to 0, assuming an ideal core, and the output filter constant reduced by changing C1 from 200 nF to 1 nF. The demonstrative pulse response is shown in Figure 4.23.

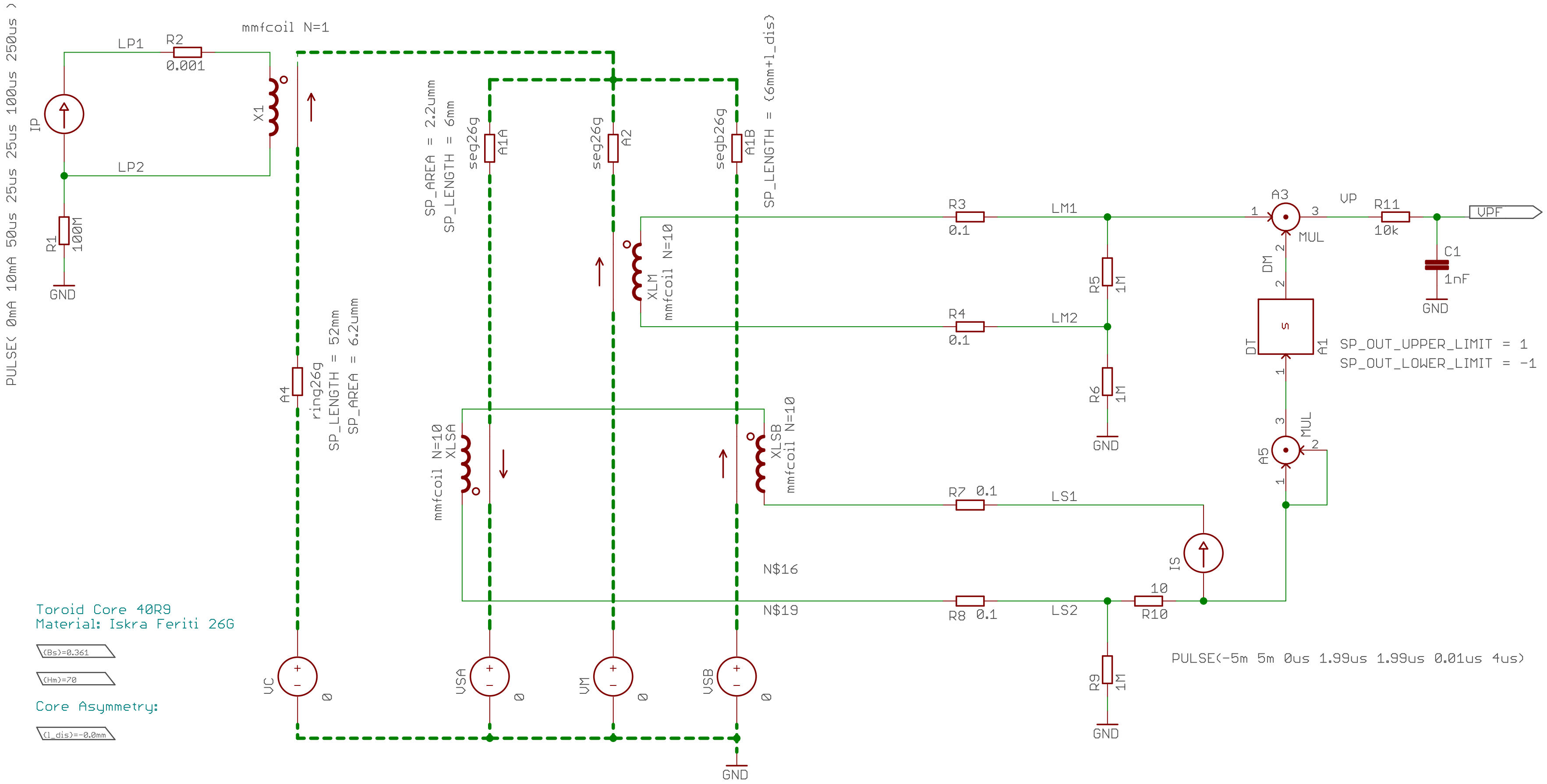

Figure 4.20: Complete Platiše Flux Sensor on a toroid core with a demodulator, see Listing B.2.

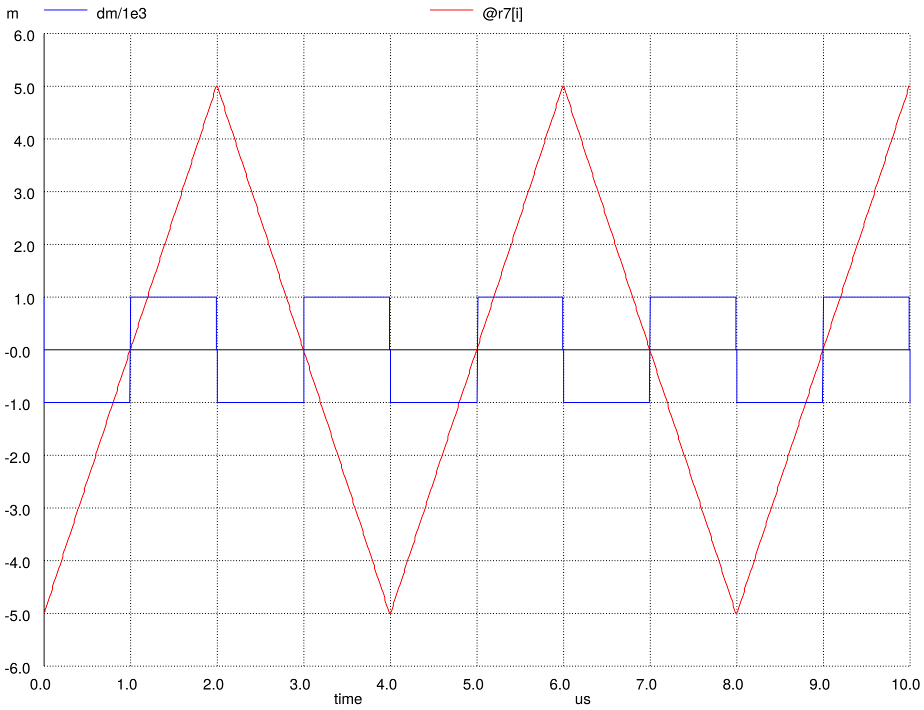

(**a**) Modulating triangle $M(t)$ stimulus current I_s in red and demodulating function $sign(|M(t)|')$ in blue.

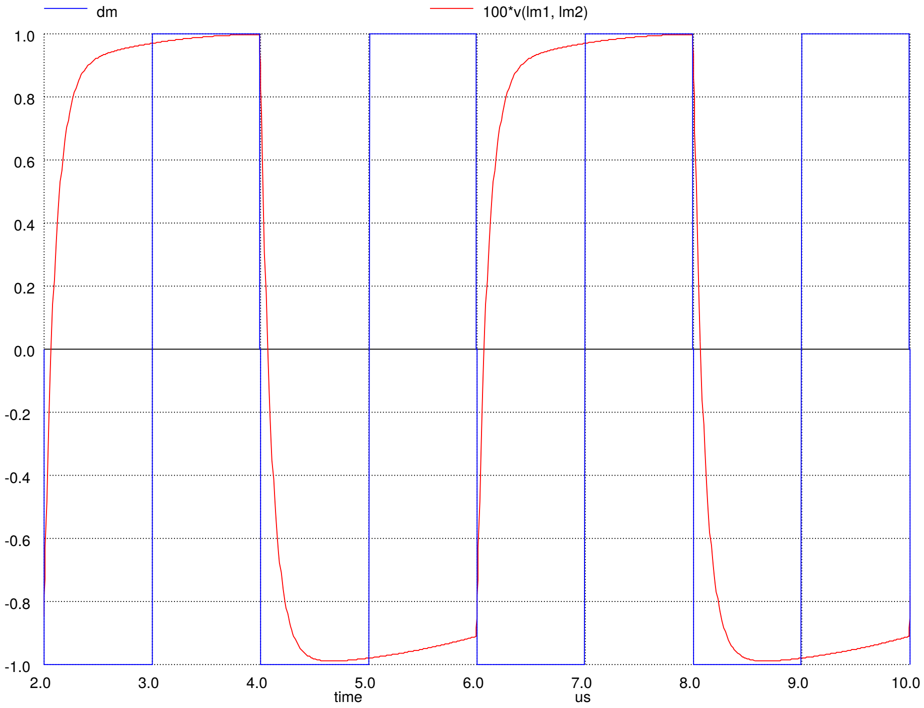

(**b**) $V(Lm1, Lm2)$ voltage for $I_p = 10$ mA measured on R5 in red, and demodulating function $sign(|M(t)|')$ in blue.

Figure 4.21: The simulation results of a complete Platiše Flux Sensor Core Model from Figure 4.20 for quasi-symmetrical openings with cross-talk, displacement of 0.2 mm.

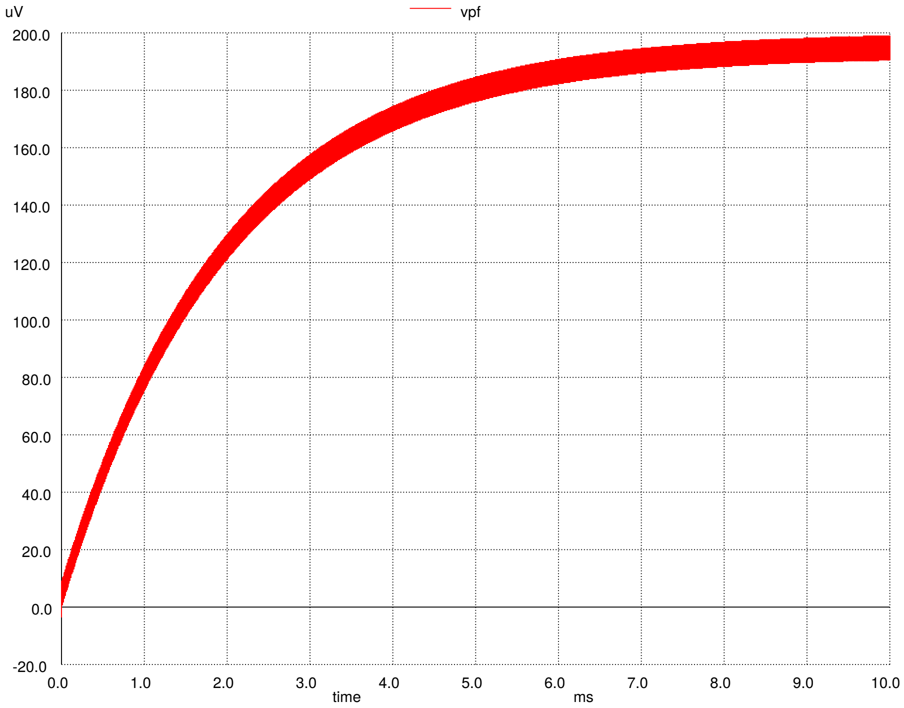

Figure 4.22: Demodulated VPF voltage, measured on R1 for $I_p = 10$ mA.

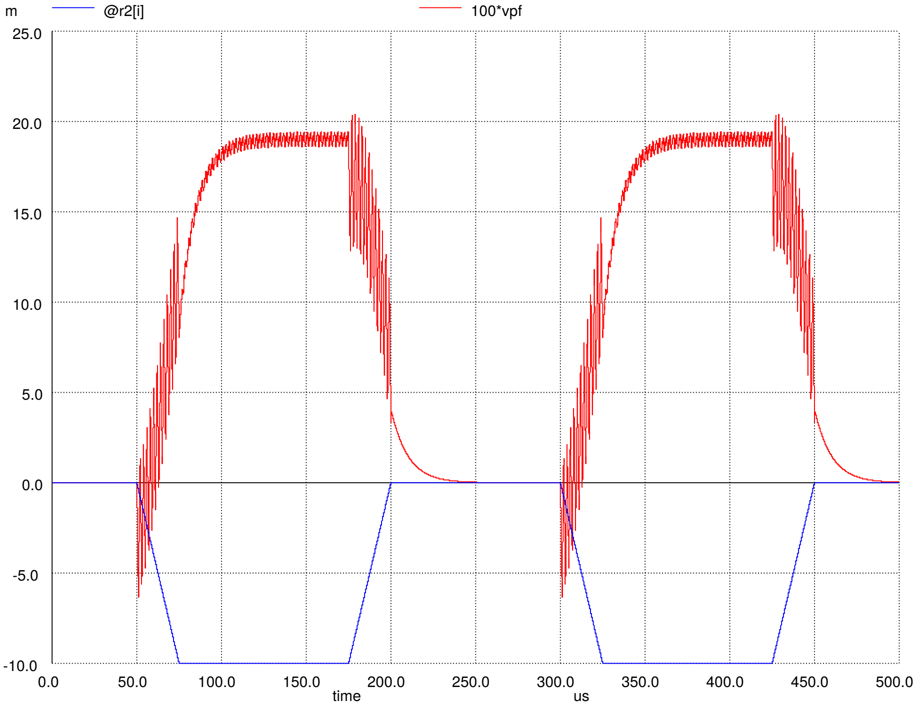

Figure 4.23: Pulse response of the PFS voltage in [V] magnified 100 times in red, for ideal symmetrical openings without cross-talk, and input current measured on R2 in [A] shown as inverted in blue.

4.6 Discussion

When designing the core with the Platiše Flux Sensor, the goal is to achieve high sensitivity S at the highest SNR for a core and a material defined by mechanical constraints and a trade-off between the minimal required stimulus current I_s, the minimal leakage into the core, at the minimal number of L_s and L_m turns to simplify the production process.

The accuracy of the sensor is typically defined by the gain stability, linearity, offsets and their drifts. In closed gapless cores, gain is a function of permeability $\mu(T)$ influenced by temperature changes. An air-gap reduces and thus stabilizes the permeability dependence on the temperature, i.e., $d\mu(T)/dT \to 0$, making the sensor also suitable for open magnetic field measurements.

The Platiše Flux Sensor design with a symmetric modulation cancels offsets that could have otherwise occurred due to the cross-talk and the electronics circuitry. This means the majority of the offsets come from the material itself as described in Chapter 4.3.3. Cross-talk also provides a higher ripple output (as per SNR), for whose output V_{pf} only a simple first order filter has been demonstrated. However, Eq. (4.11) suggests that demodulator should integrate over a complete cycle T_s to fully cancel the transients, and provide discrete output samples at a rate $\frac{1}{T_s}$ and signal bandwidth of $\frac{2}{T_s}$.

The output of the Platiše Flux Sensor can be treated in exactly the same way as the output of a Hall sensor, a magneto-resistance sensor, or a standard (single core) flux-gate sensor. There is one significant difference, however, in that the Platiše Flux Sensor does not have an air-gap, which allows the complete magnetic circuit to reach an effective permeability μ_e as high as 10k for soft-magnetic cores, 100k for nano-crystalline cores, and even higher for special composite materials. This superior magnetic amplification is directly comparable to zero-flux sensors and the simplicity of the implementation is comparable to standard flux-gate or Hall-based sensors.

Furthermore, high-permeability materials have very low coercivity forces (H_c), but are temperature-dependent and have a non-linear $B(H)$. For this reason, the best use of a Platiše Flux Sensor for current sensing applications is in a closed-loop null-method; the same as applies to Hall sensors, flux-gate sensors, and magneto-resistance closed-loop current transducers.

Chapter 5

Direct Current Current Transducer with the Platiše Flux Sensor

In this chapter, we review the already known principles of a closed-loop DC-CT null-method with the new Platiše Flux Sensor, followed by a complete system verification and extensively tested prototype implementation.

5.1 Principle of Operation

A block diagram of a closed-loop DC-CT is shown in Figure 5.1. With reference to Figure 4.14a, it adds:

- a compensation winding L_c,
- an integrator I with a feedback amplifier for driving the compensation winding L_c, and
- an optional trans-impedance amplifier G used to convert current into voltage via a low-impedance termination. It also decreases the cut-off frequency of the AC path and thus increases both the stability and the AC performance of a sensor, as described under the quasi-zero-field transformer in Chapter 3.2.4.

A simplified transfer function of the transducer can be derived from two parts. Firstly, there is a direct AC path through the transformer between the primary winding and secondary compensation winding L_c whose transfer function was derived in Eq. (3.17). The second part is the newly added DC compensation part, which drives the same compensation winding L_c and its series resistance R_c. As one terminal of the L_c is at a fixed potential, connected to the G, and the other terminal is driven by the voltage source I, the current through the winding is in its simplest form equal to:

$$I_i(s) = \frac{V_i(s)}{R_c + sL_c} \tag{5.1}$$

To keep the key concept equations comprehensive, we neglect the influence of the primary winding and the compensation winding leakage inductance and stray capacitance, the properties of the soft-magnetic material, and the almost zero-ohm input resistance of the trans-impedance amplifier G. According to the superposition theorem, the secondary current I_2 can be combined from Eq. (3.17) and Eq. (5.1) into the following Laplace form:

$$I_2(s) = I_1(s)\frac{N_1}{N_c} \cdot \frac{sL_c/R_c}{1 + sL_c/R_c} + \frac{V_i(s)}{R_c + sL_c}, \tag{5.2}$$

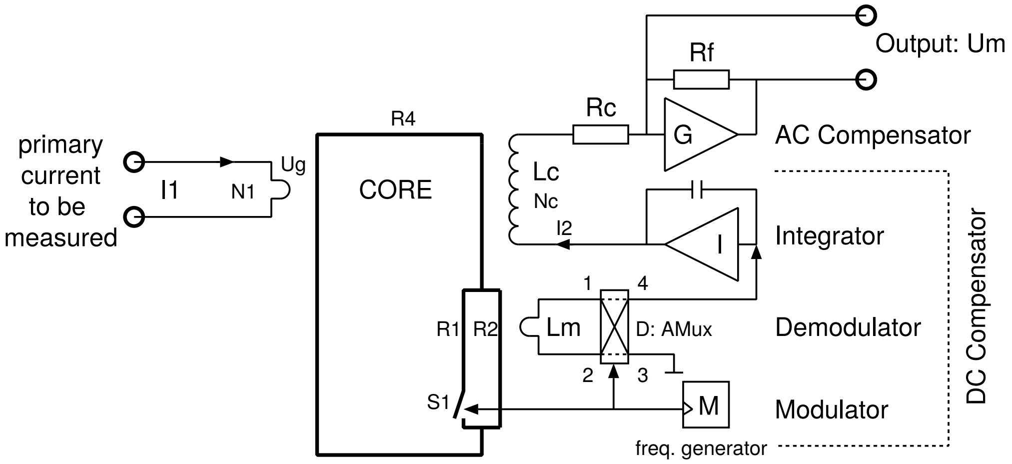

Figure 5.1: Block diagram of the DC-CT with the Platiše Flux Sensor.

where I_1 is the primary current through the primary winding of N_1 turns, I_2 the compensation current of the secondary winding of N_c turns with the inductance L_c and series resistance R_c, and V_i is the output voltage from the feedback amplifier I. Typically, the primary conductor has a single turn; however, more turns scale down the input current range, as well as the magnetic offset and hysteresis. To simplify the model, $N_1 = 1$ is used in the following text. In addition, Figure 5.1 provides a trans-impedance amplifier G, which converts and amplifies the I_2 current to a voltage U_m through the resistor R_f, i.e., $U_m = I_2 \cdot R_f$.

Due to the gapless core construction, the sensitivity of the sensor and inductance L_c is very high, as well as the time constant $\tau_c = L_c/R_c$ with cut-off frequencies below 100 Hz. This means the required gain of a Platiše Flux Sensor is low, although its sampling frequency is very high, making the DC-CT easily stable and characterised by low noise. In such a transducer, the wide bandwidth AC part of the I_1 flows directly through the core and the compensation winding L_c, while the output from the flux sensor compensates for the small errors starting at a few hundreds Hz down to DC. The ideal resulting current through the L_c is thus reduced by a factor N_1/N_c.

The DC compensation part represented in Figure 5.1 with the additional amplifier I offers a bidirectional operation from a single power supply. For stable operation, it also requires a proportional part of the regulation loop to be able to guarantee a sufficient phase margin for stability. Therefore:

$$V_i(s) = V_p(s)\left(K_p + \frac{K_i}{s}\right) \tag{5.3}$$

where K_p and K_i are PI regulator parameters and V_p is the residual flux in voltage as demodulated by the Platiše Flux Sensor. It can be simplified to a simple linear relation around the zero of the function and within the limited range of approximately ±250 mA to represent the difference between the primary and compensated currents:

$$V_p(s) = S \cdot \Big(I_1(s) - N_c I_2(s)\Big) = S\Delta I(s) \tag{5.4}$$

S in Eq. (5.4) is the sensitivity of the CCVR in V/A referred to input (RTI). Substituting Eq. (5.3) and Eq. (5.4) in Eq. (5.2) yields the basic, conceptual, input/output transform function of the DC-CT:

$$I_2(s) = \frac{I_1(s)}{N_c} \cdot \frac{s^2 Lc + sK_p N_c S + K_i N_c S}{s^2 L_c + s(R_c + K_p N_c S) + K_i N_c S} \tag{5.5}$$

In the null-method, we are interested in the difference ΔI that directly represents the error between the primary and compensation currents as well as the flux levels at which the core operates during the transients:

$$\Delta I(s) = I_1(s) \cdot \frac{sR_c}{s^2 L_c + s(R_c + K_p N_c S) + K_i N_c S} \tag{5.6}$$

Opening the regulation loop by setting $K_p = K_i = 0$, the equation reduces to the first order response with the time constant L_c/R_c, as was already shown in Eq. (3.13). A soft-ferrite material and gapless construction sensor is stable and linear within about the $\Delta I_{max} = \pm 250$ mA range, so a required condition for stable operation is:

$$|\Delta I| < |\Delta I_{max}| \tag{5.7}$$

The Eq. (5.6) may be re-organized in a typical form of a 2^{nd} order system with the additional zero at 0:

$$\Delta I(s) = I_1(s) \cdot \frac{sR_c/(K_i N_c S)}{s^2 L_c/(K_i N_c S) + s(R_c + K_p N_c S)/(K_i N_c S) + 1} \tag{5.8}$$

As the poles are typically away from the zero of the function, the self frequency and damping factors are sufficiently well approximated using well-known relationships as a starting point:

$$\omega_0^2 = \frac{K_i N_c S}{L_c} \tag{5.9}$$

$$\frac{2\zeta}{\omega_0} = \frac{R_c + K_p N_c S}{K_i N_c S} \tag{5.10}$$

Setting up the regulation loop may begin with the K_i taking into account the following (practical) considerations:

- soft-magnetic materials have large tolerances that vary with temperature and between lots, for which L_c may vary from -50% to $+100\%$,
- ω_0 should be at least a decade higher than the cut-off frequency of the AC transformer response, determined by the L_c/R_c time constant,
- ω_0 should be at least a decade below the sensor bandwidth sampling with frequency T_s and post-filtered, also considering the dead-time of the demodulator, possibly lowering the maximum ω_0 for another decade,
- $|\Delta I|$ error on step response can be minimized by increasing the ω_0,
- $|\Delta I| < |\Delta I_{max}|$ stability should be ensured under all normal operating conditions,
- feedback voltage V_i operates in a limited range,
- feedback amplifier operates with a limited slew rate,
- the noise provided by the sensor and other components that also limit the K_i and K_p should considered.

Once K_i is determined, a good start for ζ is 1, which in turn determines K_p. Sensitivity S as well as L_c are impacted by the temperature changes due to the material permeability $\mu(T)$ changes, however keeping the ratio S/L_c quasi constant. The R_c changes may be ignored as $K_p N_c S \gg R_c$ and thus the following simplification may be used:

$$K_p \approx \frac{2\zeta}{\omega_0} K_i \tag{5.11}$$

5.2 Verification

In Chapter 4.5.2, we modeled a basic Platiše Flux Sensor with the Modulator, and Demodulator, which has now been upgraded to a complete conceptual closed-loop DC-CT, as described in the previous chapter.

Eagle ngspice schematics are shown in Figure 5.2 with ngspice generated Listing B.3 in Appendix B. It consists of a core model TR1, a primary pulse excitation current (IP) and current sense (VP), the control circuitry representing a modulator and demodulator, a feedback path with a KI regulator (A2, A3), and a unity amplifier (A4) and a secondary current sense VC. With the aim to verify the complete core — the modulator and demodulator — regulator chain, a single and simple transfer function from Eq. (5.6) is represented by a Laplace block (A1), whose ΔI output is to be compared with the error between the primary and secondary currents of the core, referred to as input (RTI).

The core model with the Platiše Flux Sensor from Figure 4.15 is represented by a component named TR1, and valued 40r9, featuring 4 windings, a primary TR1LP, a secondary TR1LC, a stimulus winding TR1LS, and a measuring winding TR1LM. The TR1 40r9 Eagle ngspice component schematics are shown in Figure 5.3 with the ngspice generated Listing B.4 in Appendix B.

Similarly, the modulator and demodulator from Figure 4.20 are represented by a controller, the X1 component valued trimod, denoting the triangular modulation function $M(t)$ from Chapter 4.5.2. The component provisions connections that would be needed in more realistic schematics, such as VCC, GND, REF, and the ROK - Range OK signal, which may be ignored for now. The X1 trimod Eagle ngspice component schematics are shown in Figure 5.4 and the ngspice generated Listing B.5 in Appendix B, with the sensor output (SOUT) driving the PI regulator.

Model parameters of the 40A9R core are outlined in Table 5.1, which were used in the core model. The core is designed for ±40 A with secondary winding of $N_c = 1000$ turns. The sensitivity S has been obtained by FEM in Chapter 4.3.2.1 and ngspice simulation in Chapter 4.5.2, to be about 20 mV/A RTI.

The L_c/R_c time constant is ≈30 ms. We select ω_0 to be 100 times that frequency, thus 523 Hz (3286 rad/s), and 30 times below the demodulator filter bandwidth of 16 kHz (R11=10k and C1=1nF from Figure 5.4). From Eqs (5.9) and (5.11) and $\zeta = 1$, we get:

$$K_i = \frac{\omega_0^2 L_c}{N_c S} = 377857 \text{ [1/s]} \tag{5.12}$$

$$K_p = \frac{2 K_i \zeta}{w_0} = 229 \tag{5.13}$$

and the transfer function Eq. (5.6) becomes:

$$\Delta I(s) = I_1(s) \frac{23s}{0.7s^2 + 4623s + 7557143} \tag{5.14}$$

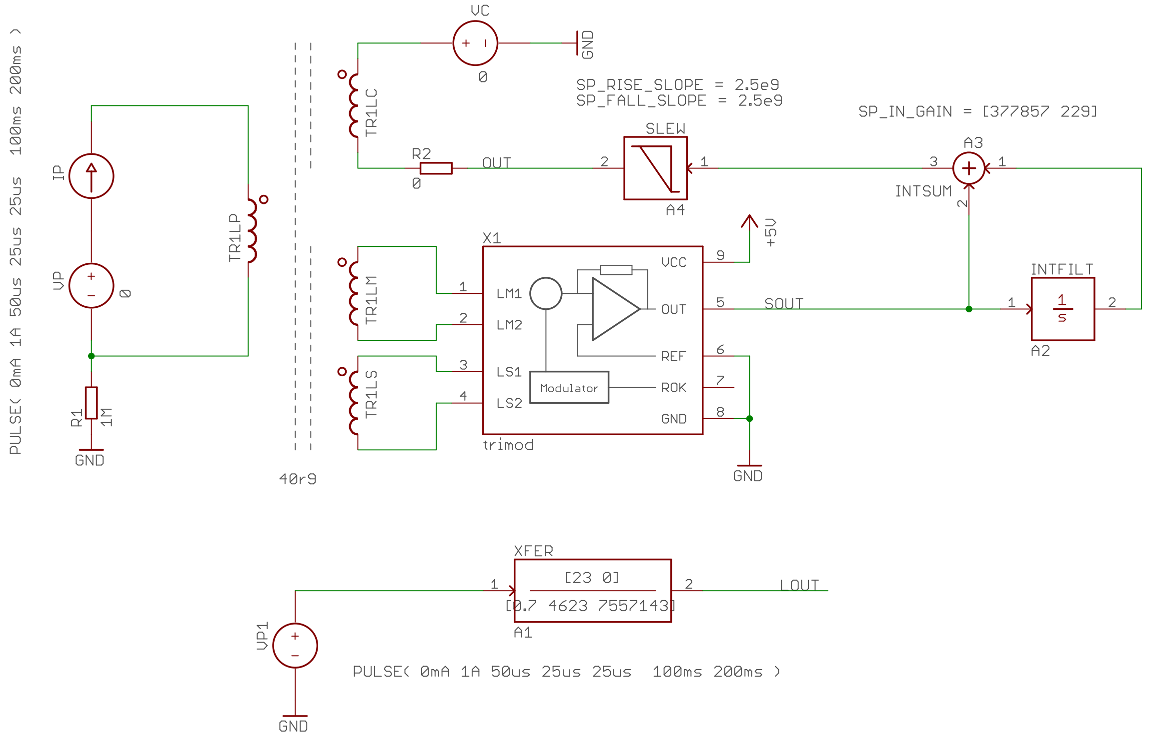

Figure 5.2: Concept simulation of the complete DC-CT with the Platiše Flux Sensor, see Listing B.3.

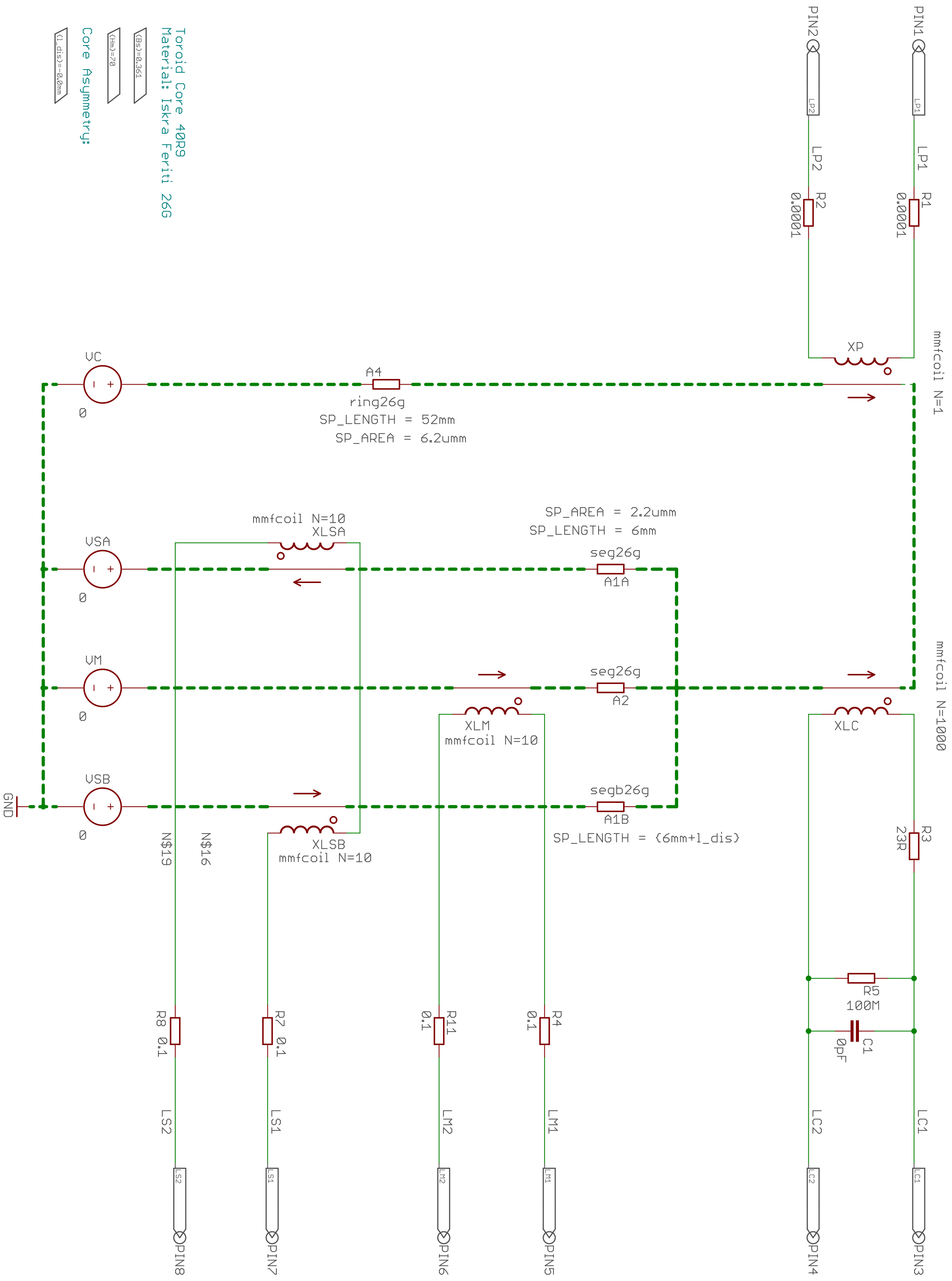

Figure 5.3: The 40r9 core model with the Platiše Flux Sensor, see Listing B.4.

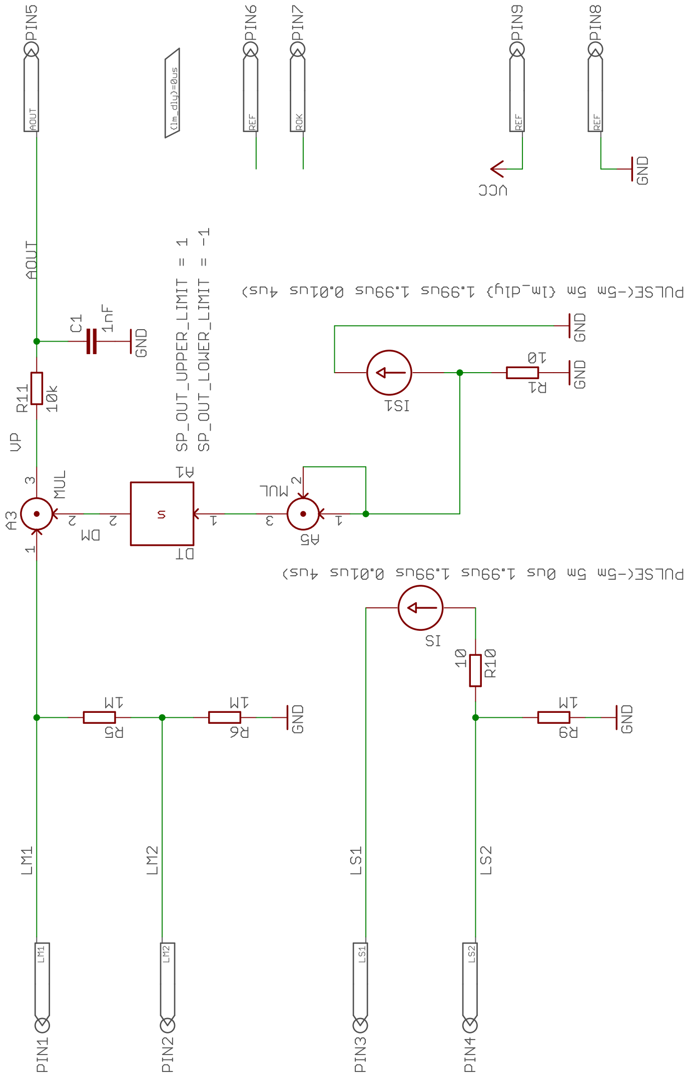

Figure 5.4: Modulator and demodulator for the Platiše Flux Sensor, see Listing B.5.

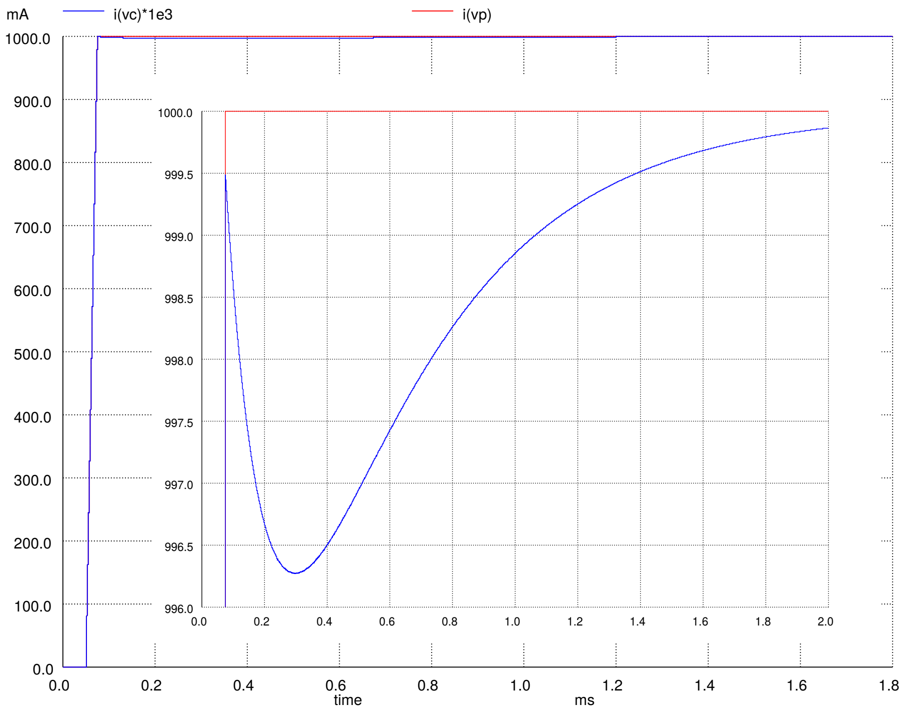

Figure 5.5: The step response of the output of the DC-CT on a unity input of 1 A. For easier comparison the secondary current is referred to input, thus multiplied by $N_c = 1000$.

5.2.1 Validation

The step response of the output of the DC-CT on a unity input of 1 A is shown in Figure 5.5 with the zoom-in, where secondary current is referred to input, multiplied by $N_c = 1000$. The proposed controller works by always requiring an *error* before the K_p and K_i can actually begin compensating the decaying response of an otherwise pure current transformer. From the zoom-in part of Figure 5.5, we may observe a steep initial response that belongs to the pure AC response of the current transformer, followed by slow decaying due to the L_c/R_c time constant and hence the rise of the signal from the sensor output (SOUT) in Figure 5.6, which with the K_i and K_p nullify the primary vs. secondary currents.

Stable operation is ensured by the condition $|\Delta I| < |\Delta I_{max}|$; this is why in the performance optimization the $|\Delta I|$ is the key function of our interest and is proportional to the sensor output (SOUT) as long as the core operates within the quasi-linear region. The $|\Delta I|$ may be obtained from a complete non-linear system as $(I_1 - N_c I_2)$ RTI or from a linearized and simplified Eq.(5.14), denoted by the signal LOUT in Figure 5.2. For validation purposes, both are shown in Figure 5.7. As they match sufficiently, further AC performance verification and optimization may rely on Eq.(5.14).

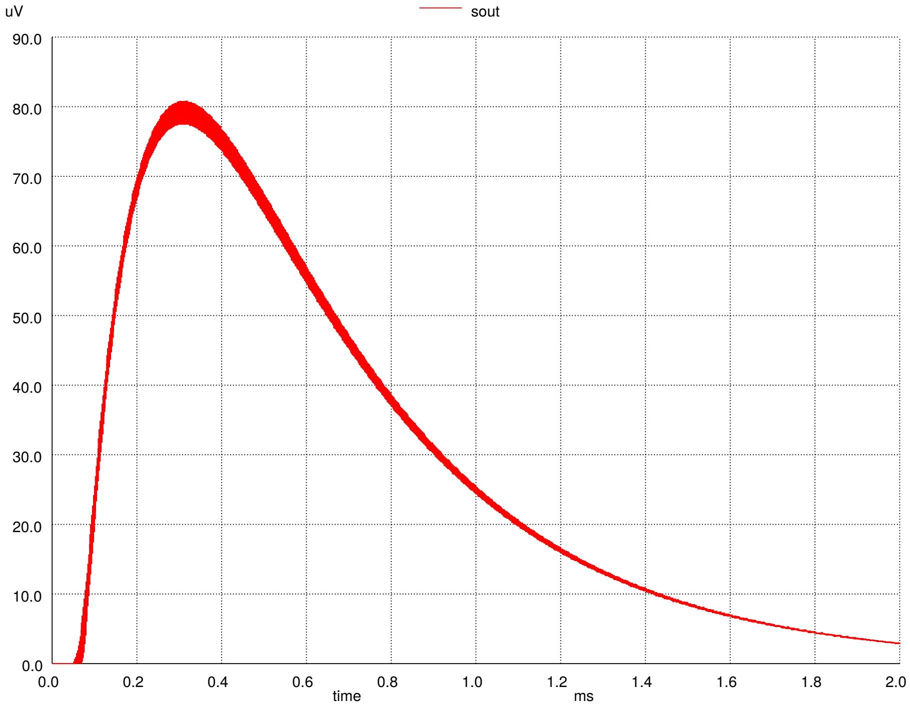

Figure 5.6: The Platiše Flux Sensor output signal (SOUT) on a unity step response.

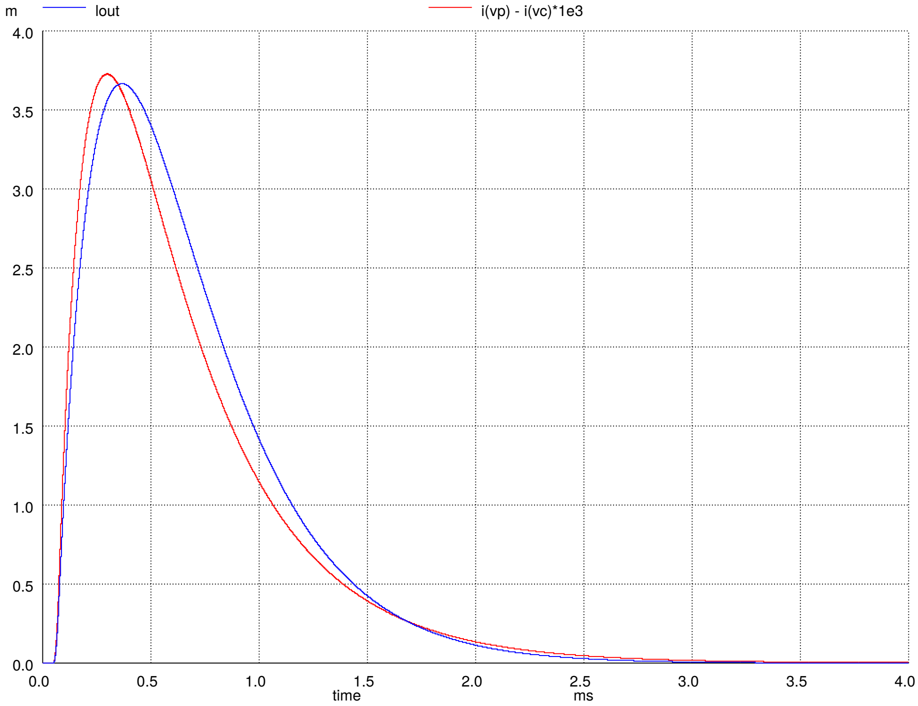

Figure 5.7: Comparison of the $I_1 - I_2 \times N_c$ and the ΔI from Eq.(5.14), signal LOUT.

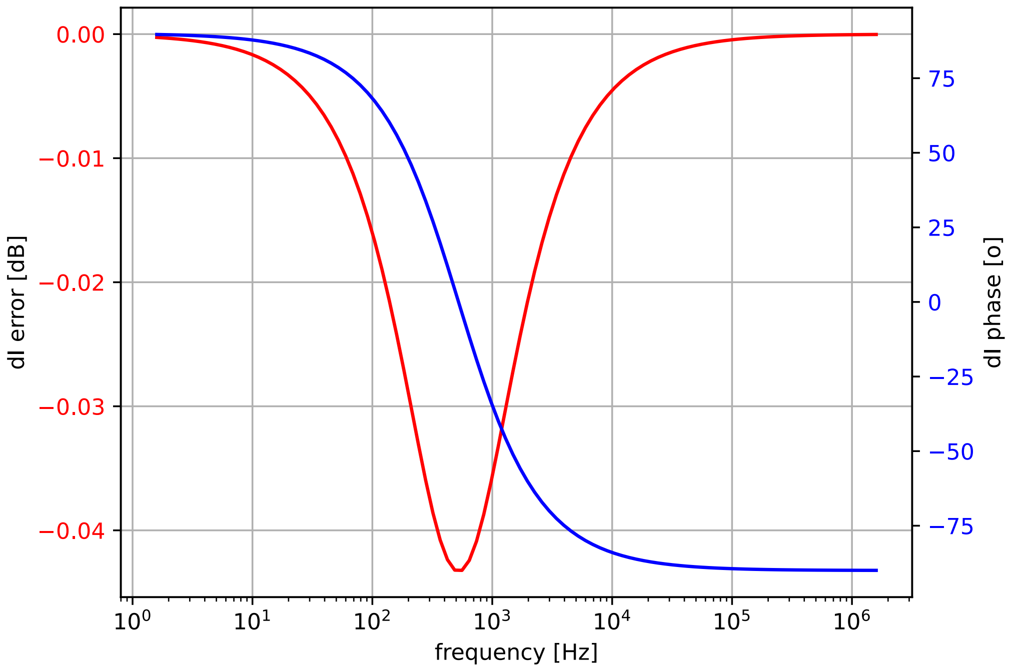

Figure 5.8: Frequency response of the Eq.(5.14) expressed as normalized current difference (dI) error RTI, calculated as $1 - |H(j\omega)|$ and its phase.

5.2.2 AC Performance

Figure 5.8 shows the frequency response of Eq.(5.14). The magnitude is plotted as $1 - |H(j\omega)|$ to represent the error (attenuation) with its phase in the secondary current I_2 normalized to the primary current I_1 in dB. The biggest error (attenuation) happens at the selected ω_0. Figure 5.9a shows magnitude plots at different damping factors ζ, i.e., 0.7, 1.0, and 2.0. The higher the ζ is, and consequently the K_p, the lower the maximum attenuation error. However, the increased ζ also increases the settling time as shown in Figure 5.9b, displaying the error referred to a primary for $I_1 = 1$ A. This same error equals to the magneto-motive force $\Theta = I_{error}$ and generates magnetic flux $\phi = B(H)$ in the core, and hysteresis loop as seen e.g. in Figure 3.2a. The greater the I_{error}, the larger the loop and thus the hysteresis effects that converts to an offset error. Overshots, for a given $\zeta < 1$, may act as small degaussing effects to a certain degree, however they resuls in higher peaking.

A simplified model as represented by Eq.(5.14) offers an easy control and tuning of the K_p and K_i parameters, along with the core parameters, for the best AC and DC performance as per the application requirements, as long as the conditions listed in Chapter 5.1 are met. Note that in the above derivation, none of the effects from the primary circuit were considered, including the air-coupling between the primary conductor and the Platiše Flux Sensor, which may alter the performance. A high performance transducer should also consider leakage inductance of the winding and stray capacitances that typically affect frequency characteristics above 100 kHz. The optimization of these application-specific parameters are beyond the scope of this dissertation.

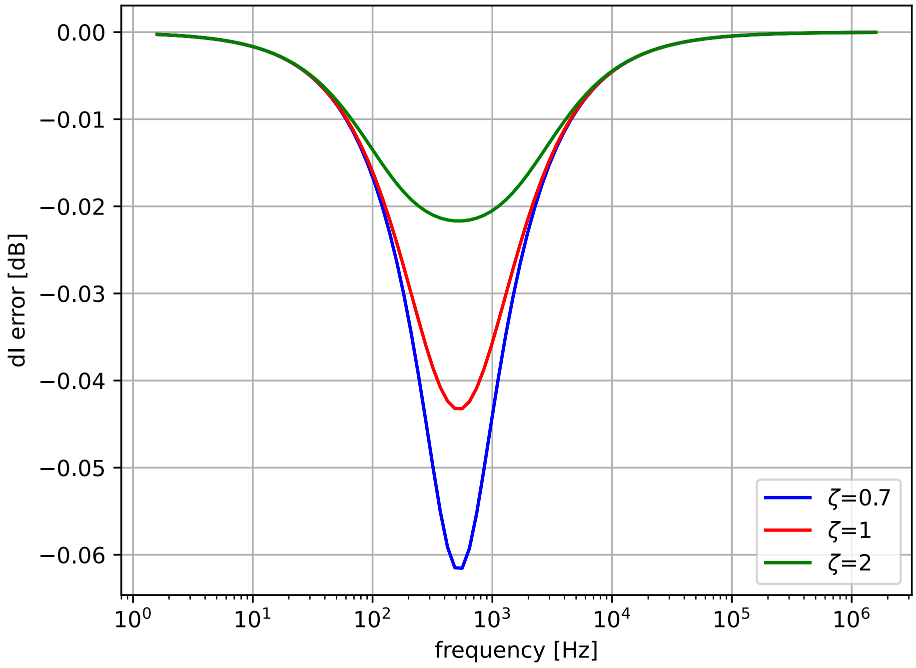

(**a**) Magnitude $|\Delta I(\omega)|$ response vs. frequency.

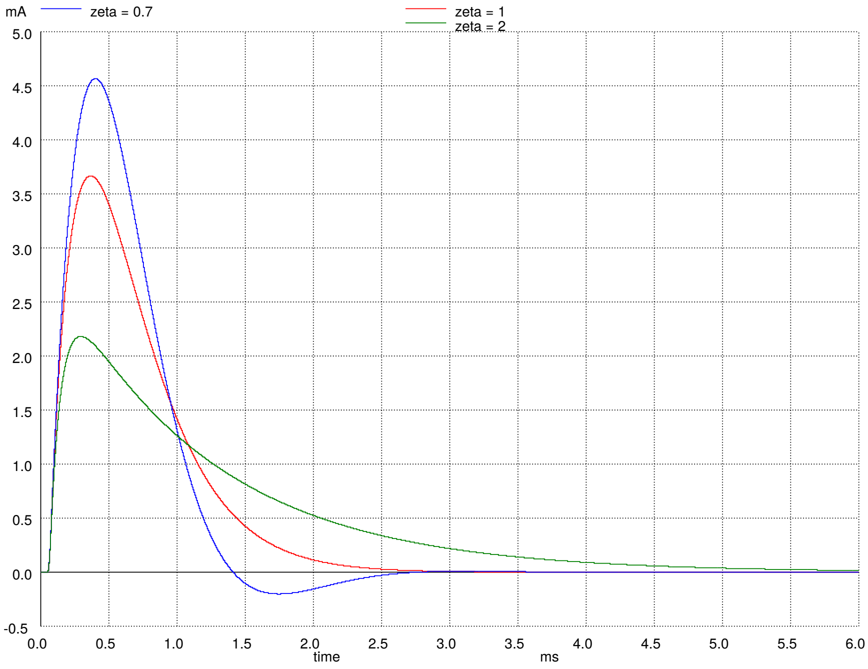

(**b**) Error ΔI on step response for primary current $I_1 = 1$ A.

Figure 5.9: AC performance of the Eq.(5.14) expressed as an error ΔI for different damping factor values ζ.

5.3 Implementation

The first proof-of-concept implementation of a ±40 A current transducer is shown in Figure 5.10a. It was implemented by using an existing off-the-shelf soft-ferrite core and a programmable analog chip in which a modulator and demodulator were implemented, with an external operational amplifer (OPAMP) as a driver. The electronics implemented with the two SO-8 silicons is placed on the PCB below the core.

After a successful evaluation, the first custom designed soft ferrite core rated for ±40 A was implemented, shown in Figure 5.10b. This core, named 40A9R, whose key core parameters are listed in Table 5.1 along with the core drawing already seen in Figure 4.8, is used as the reference core in this chapter and the previous Chapter 4. It is important to note that the implementation of such a small core 40A9R with additional openings required specially designed tools and technology processes to avoid cracking and stiffness of the soft ferrite material.

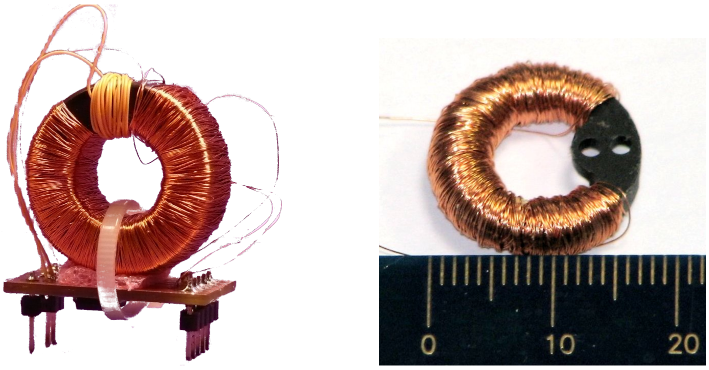

(**a**) The first proof-of-concept ±40 A DC-CT.

(**b**) The first custom-made toroid DC-CT core 40A9R.

Figure 5.10: The first soft ferrite core prototypes.

Around the time of the custom core development, a new series of powerful ARM M0 embedded micro-controllers came to the market and was used in subsequent designs. The analog electronics were upgraded with a fully digital control loop and 12-bit 1 MHz SAR ADC and 13-bit DAC signal interfaces, along the external OPAMP as a driver. The initial implementation of the DC-CT, used for extensive testing and evaluation results presented in the following chapters, used a low modulator frequency of about 20 kHz. With the progress of concepts and silicons, this frequency was risen to 222 kHz, and the regulator PI control loop reached a maximum of 111 kHz, on a low-cost M0+ ARM running at 48 MHz. Mixed signal simulations, as presented in Chapter 3.3 with embedded firmware, as presented in Chapter 3.4 have been employed in the design. However, these designs are far beyond the key concepts of the Platiše Flux Sensor, and thus out of the scope of this dissertation.

To simplify and reduce the component count, the modulator function $M(t)$ was chosen to be RC filtered square. It does generate slightly more noise but yields higher sensitivity if samples are taken on the steeply rising and falling edges. The reduction of the ripple generated by the stimulus winding L_s was successfully mitigated by a proper construction of winding and shielding. In addition, special attention was given to the shielding and molding process of the ferrite cores. Over 100 samples were built and tested to prove the feasibility of the new technology and for further engagement into the industrialization phase.

Table 5.1: Structural and electrical parameters of the 40A9R core according to Figure 4.8.

Parameter	**Value**	**Unit**
Diameter	18.3	mm
Thickness	2.6	mm
Width	2.3	mm
Cross-sectional area R_1, R_2	2	mm^2
Cross-sectional area R_4	6	mm^2
Effective length R_1 of L_s	10	mm
Effective length R_2 of L_m	6	mm
Effective length R_4 of L_c	40	mm
Material	26G by Iskra Feriti	-
Relative Permeability μ_r	2200	-
Coercivity H_c	12	A/m
Sensor winding L_s	20 | 560	turns | uH @ 100 kHz
Sensor winding L_m	10 | 254	turns | uH @ 100 kHz
Compensation winding L_c	1000 | 23 | 0.71	turns | Ω | H @ 10 kHz

5.4 Testing Environment

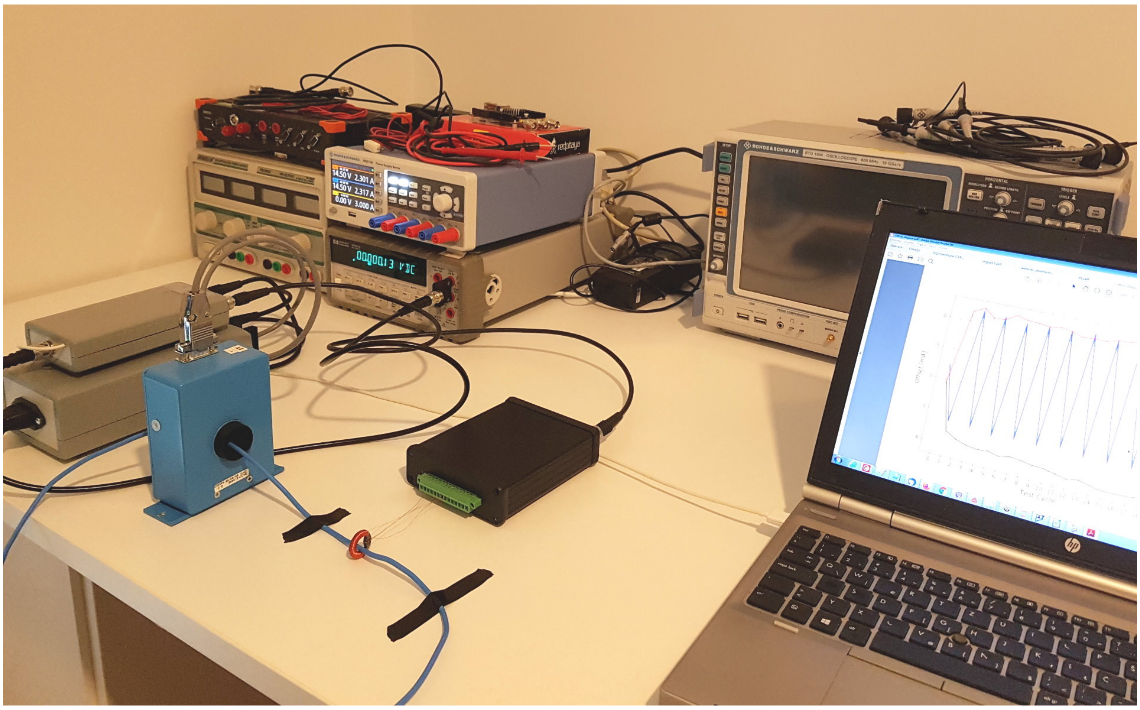

Figure 5.11: Test bench with 40A9R connected to the DC-CT evaluation controller, MACCplus 600A, HP334401A, RTO1004, NGE100, and HP66000A with the custom-developed 2 MHz generator under the table.

The testing and performance evaluation of the proposed DC current transducer based on the novel Platiše Flux Sensor was carried out in a purposely built development and automated test environment (ATE). To this end, a high-current digital linear low-noise DC/AC amplifier was developed that can handle up to 40 A at DC, 25 A up to 100 kHz, 4 A at 1 MHz, and a maximum bandwidth of 2 MHz. Multiple turns were used to achieve higher ampere-turns. To ease the firmware development, testing, and integration with ATE systems, the ISOTEL Device Manager[1] (IDM) software was used, which is freely available for download, together with the Python/Jupyter[2] integration. Further equipment used in the tests included a MACC^{plus} 600 A with a Vishay VFR S-series 2 ppm/K[3] reference shunt resistor, a modular power system HP66000A, a digital multimeter HP34401A, a data acquisition system Dewesoft Sirius for <100 kHz measurements, a digital oscilloscope R&S RTO1004 for all other measurements, various temperature chambers and supporting amplifiers, power supplies, and other accessories.

---

[1] `http://isotel.org/idm`

[2] `https://jupyter.org`

[3] `http://www.vishaypg.com/docs/63001/63001.pdf`

5.5 Performance Evaluation

The following chapters present the key performance measurements obtained for the first DC-CT prototype with the custom designed core 40A9R.

5.5.1 The Platiše Flux Sensor Operating Characteristics

Referring to Chapter 4.2, the key principle of the Platiše Flux Sensor is to redirect the flux between the paths inside the core. In Figure 4.7, we represented the static $B_{dc}(I_p, I_s)$ characteristics obtained with the FEM simulator. As constant magnetic fluxes cannot be measured with any instrument, an AC generator is applied to the core, and the frequency response is measured on L_m at different stimulus currents through the L_s. The measurement results are shown in Figure 5.12.

The sensitivity test S of the Platiše Flux Sensor is shown in Figure 5.13 as a function of the sensor output rectified, but not amplified voltage V_p for a given input current range I_p from -3 A up to +3 A, at a given peak-to-peak L_s stimulus current of 110 mAt.

Measurements in Figure 5.13 also represent the operational range of the Platiše Flux Sensor on a 40A9R core, which is perfectly linear to at least ±250 mA, giving an operational range of ±0.5 A beyond which the material begins entering the saturation region and the signal begins to fall. Sensitivity is $S = 50\,\frac{\mathrm{mV}}{\mathrm{A}}$ as per Eq. (5.4). The core can withstand an absolute maximum ΔI_{max} of ±3 A beyond which the regulation loop diverges.

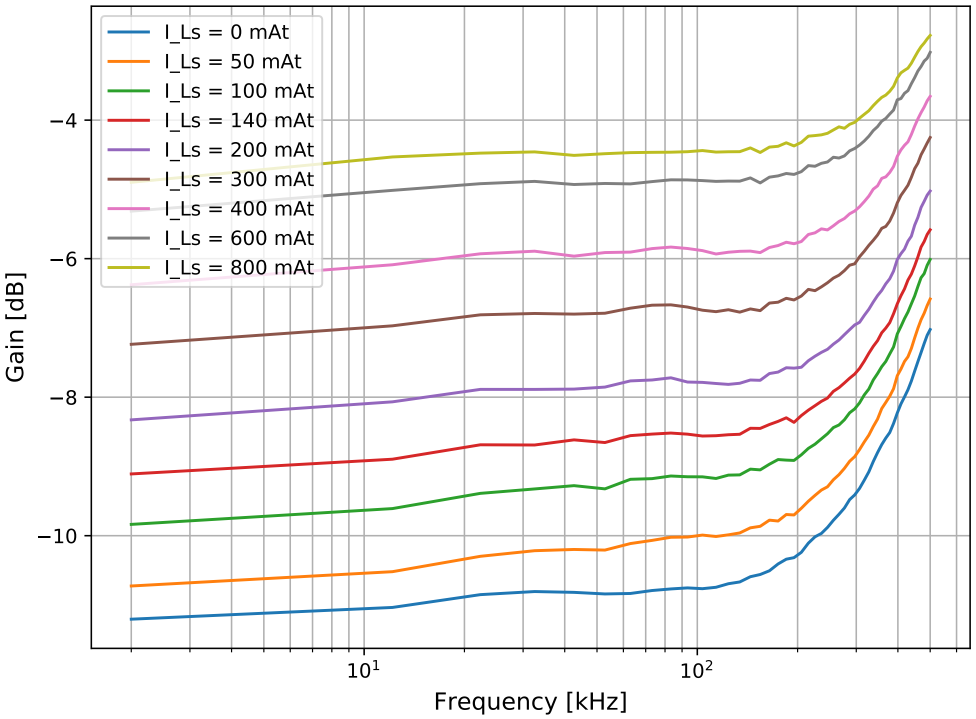

Figure 5.12: The CCVR characteristics as a function of I_s of the 40A9R core.

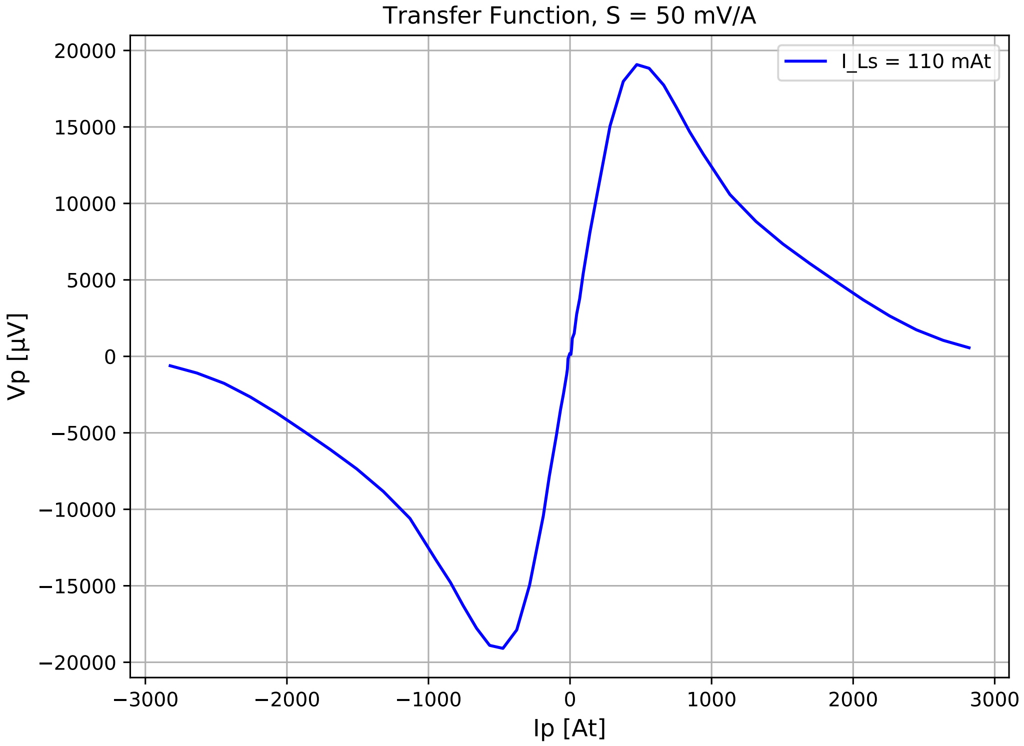

Figure 5.13: The Platiše Flux Sensor characteristics of the 40A9R core.

5.5.2 DC Linearity and Accuracy

In order to evaluate the linearity and accuracy of the prototype DC-CT, we used the testing setup depicted in Figure 5.11 with:

- HP66000A as a current source,
- MACCplus 600A as a reference instrument,
- Vishay VFR S-Series, S102K (50.000 Ω, 0.01%, 4.5 ppm/K) and S102CT (100.00 Ω, 0.01%, 3.5 ppm/K) in parallel as a burden resistor of value 33.333 Ω, and
- HP34401A as the 6.5 digit voltage meter.

The three major contributors of DC offset errors all relate to the core material:

- The initial offset due to the magnetization of the core H_c; this can be improved to a large extent using the degauss procedure of the form $A\sin(\omega t) \cdot e^{-t/T}$ to reset the core to its initial condition.
- The hysteresis of the core material as a result of non-zero ΔI due to the principle of operation of the PI regulation loop and a non-homogeneous distribution of the magnetic fields between the primary conductor and the core in a zero-flux configuration.
- The temperature drift, which is directly proportional to the remaining offset in the magnetic core due to the previous two error sources and the temperature-related changes of the material itself.

Table 5.2: Measurement uncertainty evaluated at 10 A and 40 A of the primary current, and coverage factor $k = 1$.

Standard Measurement Uncertainty	u_c **@ 10 A (ppm)**	u_c **@ 40 A (ppm)**
40A9R current reading (Type A, N = 10)	8	2
HP34401A as 6.5 digit volt meter from specifications and 90 days	98	34
MACCplus 600 A from specs with 10 °C temperature rise and 90 days	13	13
Uncorrected Vishay VFR S-series resistor from specs with 10 °C rise	84	84
Uncorrelated sum	**130**	**92**

The major source of gain error is introduced by the output trans-impedance amplifier attached to the secondary compensation winding, which converts the secondary current into a voltage output. In this prototype design, a long-term stable resistor with 0.2 ppm/K from the Vishay Z-Foil VSMP series 1206 [4] was used, which defines the gain stability. The measurement uncertainties of the entire setup are given in Table 5.2.

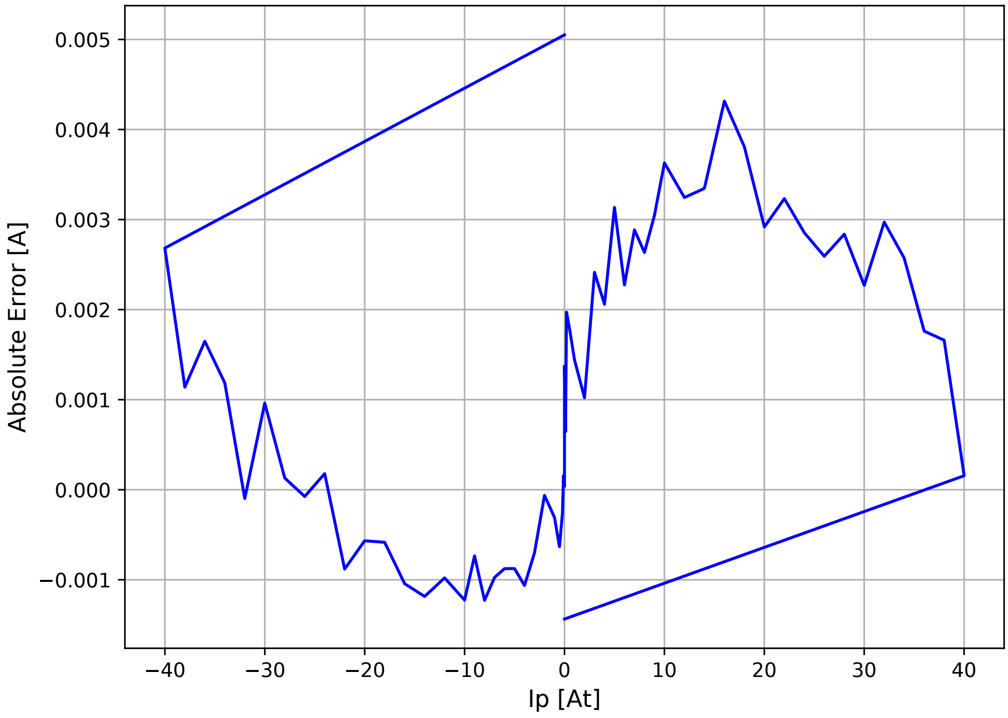

Figure 5.14: Hysteresis and linearity of the 40A9R.

Figure 5.14 illustrates the linearity and hysteresis loop of the corrected gain, calculated as the best fit straight line (BFSL) between the primary and secondary currents. The measurement was taken after applying degaussing in each direction to the rated range (X axis), while the Y axis represents the absolute error from the BFSL.

---

[4] `http://www.vishaypg.com/docs/63060/VSMP.pdf`

The closed-loop operation ensures a very high linearity, with a peak-to-peak of 6 mA within the entire 80 A range. The gain is slightly affected by the primary winding position and the asymmetrical winding due to additional openings in the core, which was to some extent elaborated in [56]. As the linearity is about 200 ppm at coverage factor $k = 2$ and by taking into account the stability part of the VFR uncertainty only (<45 ppm), the gain accuracy specification was adopted from the Vishay VSMP burden resistor specifications.

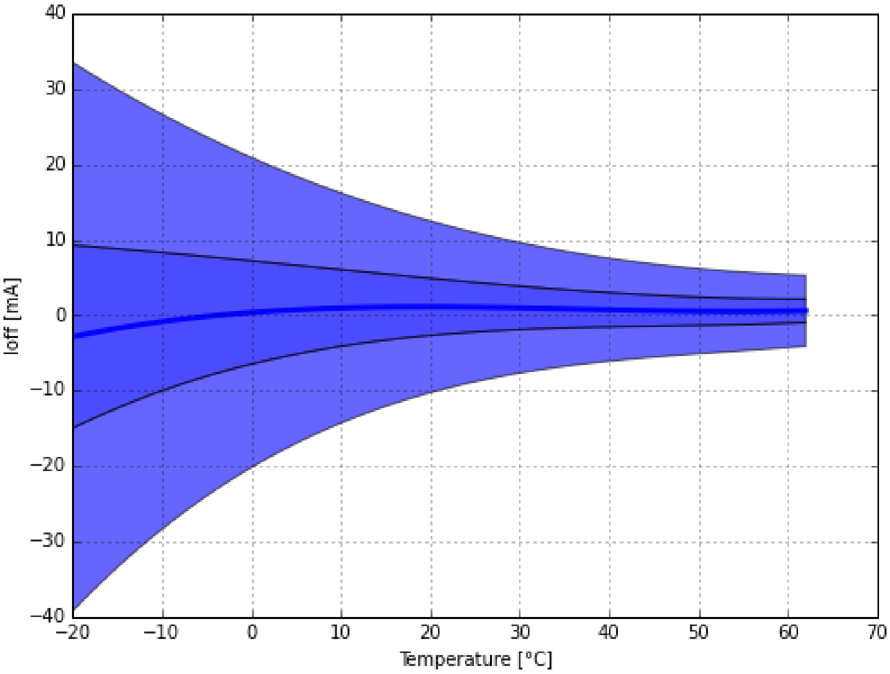

Figure 5.15: Temperature stability at 25 A.

The temperature stability at a continuous and constant current of 25 A applied after the degauss procedure was measured on 11 samples in a temperature chamber. The results are shown in Figure 5.15. The outer envelope represents the $\pm 3\sigma$ standard deviation, the inner the $\pm\sigma$ standard deviation, both interpolated with a polynomial, and the curve in the center shows the mean value. At lower temperatures, the offset accuracy is affected by the lower permeability of the soft ferrite magnetic core. The decreased magnetic gain and increasing H_c degrade the sensitivity S and thus the precision of the Platiše Flux Sensor.

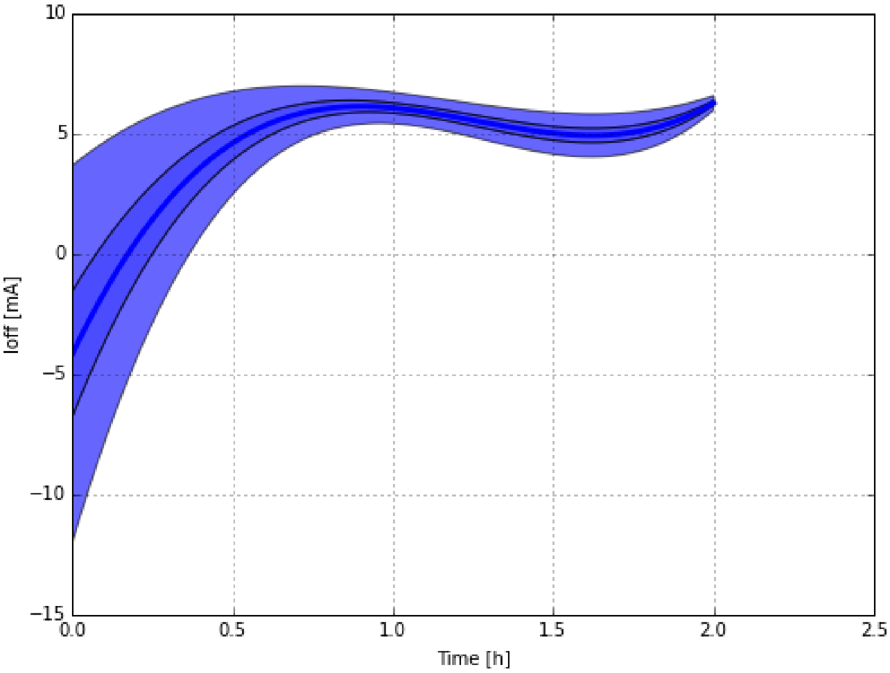

Figure 5.16: Stability over time at 25 A and $T_a = 25°\text{C}$.

A two-hour test was conducted with the same samples at a constant ambient temperature $T_a = 25°\text{C}$ and constant primary current of 25 A to observe stability over time. The result is shown in Figure 5.16. The initial drift is due to the (self-)heating effects, which then remains stable within a mA. The stability performance met the requirements of Eletra 20 A power supplies for use in their synchrotron, as extensively elaborated and described in [57].

Hysteresis changes and offset drifts versus the series of cycles from zero to positive and the negative maximum rated range and alternating between the minimum and maximum, are shown in Figure 5.17a after the degaussing is applied, and in Figure 5.17b without the degaussing.

The worst case measurements are summarized in Table 5.3.

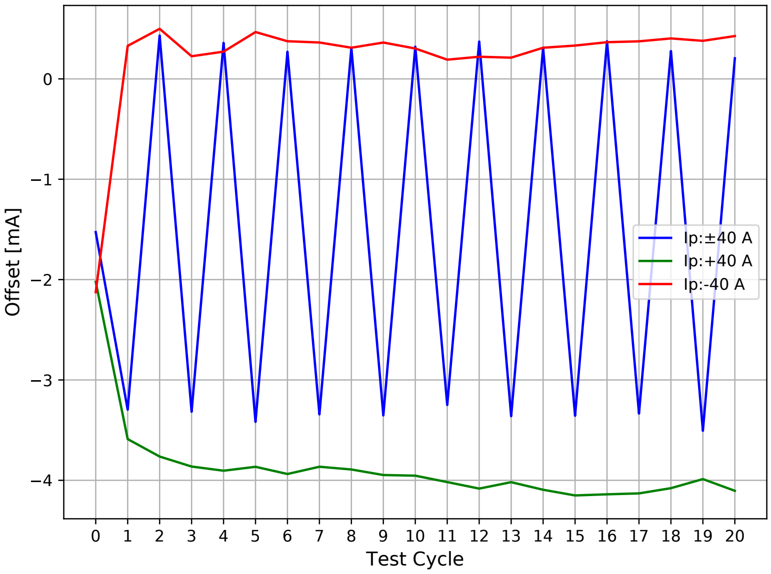

(**a**) Cycling at the rated range after degaussing is applied.

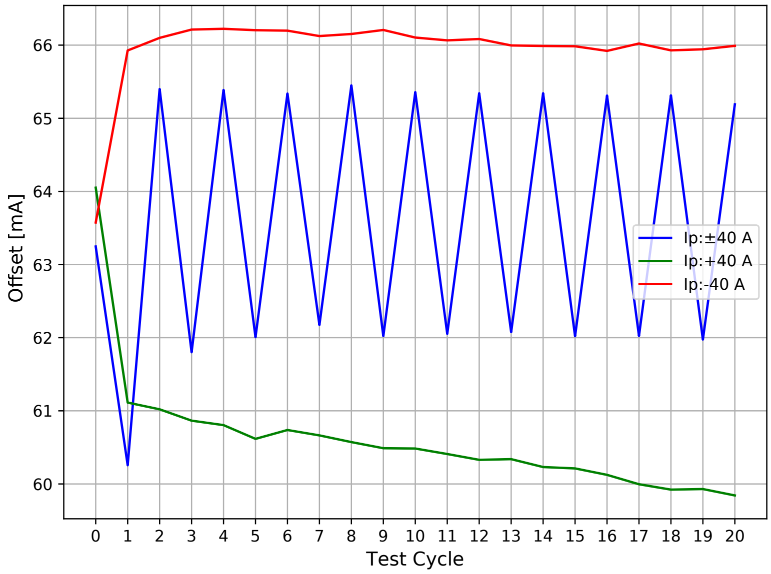

(**b**) Cycling at the rated range without degaussing.

Figure 5.17: Hysteresis changes and drifts versus the series of cycles.

5.5.3 Immunity to External Magnetic Fields

During both development and testing, we paid special attention to the shielding with mu-metal and its negative effects on the curvature of the magnetic field of the primary conductor. The design of the primary conductor winding must cancel its own magnetic field to minimize interference with the mu-metal. Strong currents can saturate it and nullify the shielding properties of the mu-metal shield. Our goal was to use the DC-CT near higher current DC /DC switching power supplies, which generate significant electromagnetic noise with their chokes and must be suppressed. Figure 5.18a shows the immunity to the external magnetic field measured in a Helmholtz coil, and Figure 5.18b shows the reference orientation of the DC-CT device during these measurements. The immunity on the Y-direction is worse than in the X- and Z-directions due to the opening on the bottom side of the housing with the primary conductor and the connecting pins of the electronics.

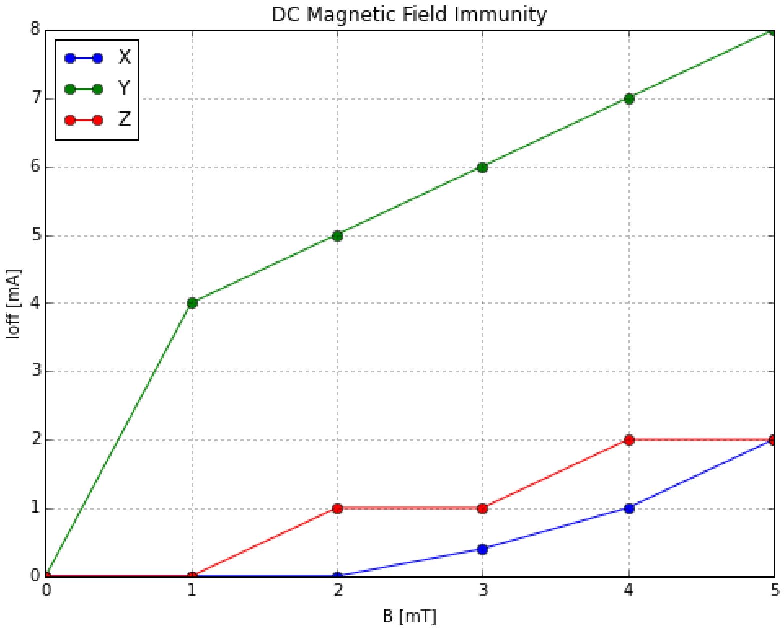

(a) Immunity expressed as offset in all 3 axis.

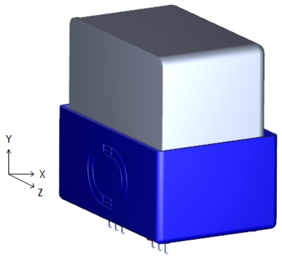

(b) Orientation.

Figure 5.18: Immunity to external magnetic fields.

5.5.4 Noise

The noise of the prototype DC-CT was evaluated by using the RTO1004 oscilloscope and a direct connection of the core 40A9R to a burden resistor of 8 Ω. The system noise floor of the measurement setup without DC-CT was 83 μA_{rms} at 10 kHz, 283 μA_{rms} at 100 kHz, and 972 μA_{rms} at 1 MHz bandwidth.

The operation of the proposed DC-CT identified three major sources of noise:

1. Periodic excitation used in CCVR, which is seen as a ripple at a constant frequency and its harmonics above 100 kHz.
2. A compensation regulation loop with the amplitude depending on the sensitivity of the sensor and loop parameters below 10 kHz.
3. Output electric noise.

Table 5.3 lists the noise of the 40A9R core with the CCVR driven by a purely digital output driver operating at 220 kHz measured on the Vishay VSMP shunt resistor of 33.2 Ω and a bandwidth-controlled (limited) voltage input.

5.5.5 AC Performance

The practical AC bandwidth limits of the DC-CT are defined by the core material, the electronics circuitry, and the wiring methods of the compensation winding, as well as the complete primary winding circuit. Note that one meter of a straight wire of 4 mm in diameter already has a self-inductance of 1.2 μH and a resistance of 1.4 mΩ. The time constant of such a wire $\tau = L/R$ is nearly 1 ms and limits the excitation rise times. For this reason, the primary loop needs to be minimized and the wire twisted in the test setup.

A non-ideal compensation winding includes the parasitic capacitance between the winding to the core and the leakage inductance that distorts the flatness and may show up as resonances at certain frequencies. In this setup, we used:

- a custom made 2 MHz generator with integrated RedPitaya[5] as the DAQ, and
- the RTO1004 oscilloscope.

The Bode diagram was calculated by cross-correlating the reference input current with the output of the DC-CT. The flatness accuracy was not evaluated specifically in this case.

Figure 5.19 shows large signal step responses, representing the typical use in DC/DC switching applications. Slightly higher frequency damping is observed in transient response, resulting in a timing response (measured at 90%) of about 1.5 μs, while the response time (measured at 10%) is less than 100 ns for a maximum current slope of 30 A/μs reached with our test setup.

Figure 5.20 shows the bandwidth of the 40A9R transducer, separately for magnitude and phase. In this particular test, the AC current at 100 kHz was more than 6 A and gradually decreased to about 1.5 A at 1 MHz. The flatness between 1 kHz and 200 kHz is a shortcoming of the filter design used in this prototype. As one approaches the MHz frequencies, the capacitive coupling between the primary and secondary winding comes into effect, which suddenly drops due to the limitations of the soft ferrite core material.

---

[5] `https://www.redpitaya.com/`

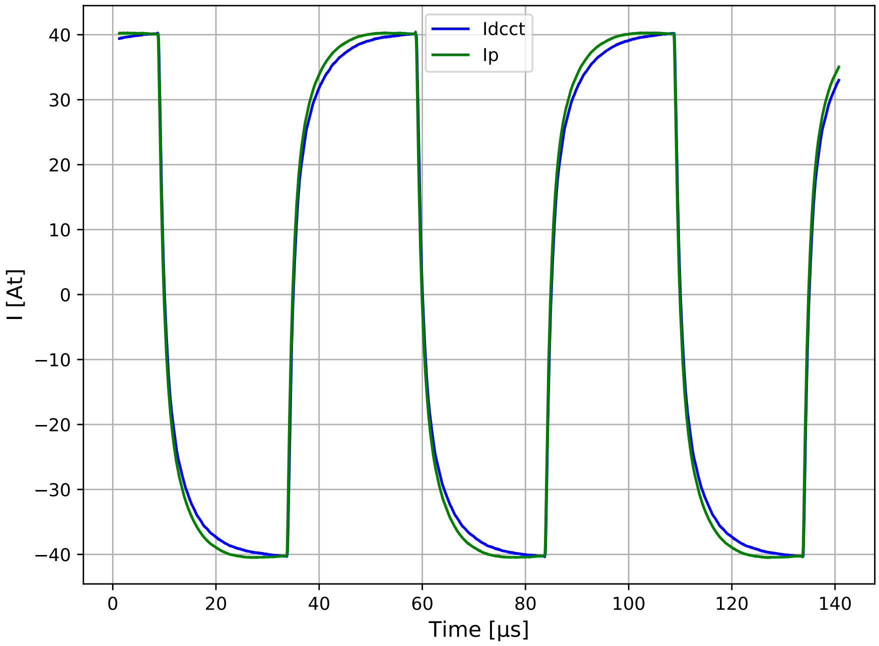

Figure 5.19: Large step response of the 40A9R core.

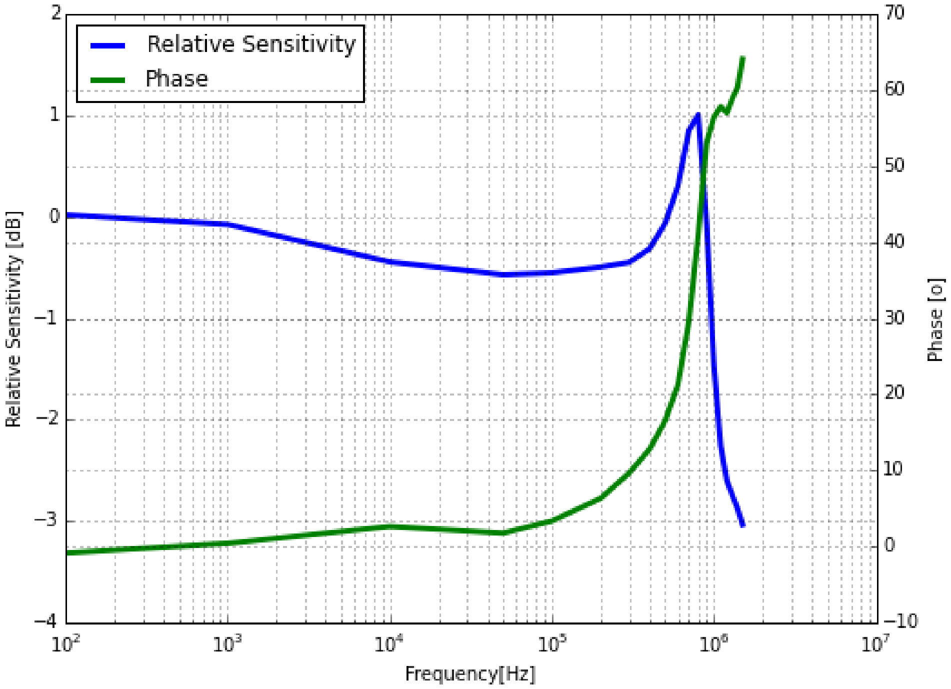

Figure 5.20: Small signal bandwidth, 15% I_p until 100 kHz, and 3% I_p at 1 MHz.

5.6 Summarized Results and Comparison with LEM DC-CTs

Table 5.3 summarizes the performance results for the prototype DC-CT based on 40A9R core and compares them with widely used DC-CTs of different performance classes and technologies. LEM IT represents the highest performance LEM transducers based on a tri-core flux-gate. LKSR family is a low cost family based on a single-core flux-gate, and the LZSR is based on a Hall sensor.

The new DC-CT with Platiše Flux Sensor significantly outperforms the single core flux-gate technology and with the lower current consumption and wide bandwidth competes with the LEM IT technology. The evaluation of the 40A9R shows the market potential in the proposed accuracy classes, i.e., 0.1% for lower amps, such as is 40A9R, and down to 0.01% for high current transducers.

Further developments continue in the direction of using higher permeability materials, which will further reduce the magnetic offset and hysteresis, and D-class design of the secondary winding amplifier to further reduce power consumption.

Table 5.3: Performance comparison of current transducers of different technologies.

	DC-CT 40A9R	**LEM IT 60A** [1]	**LKSR-50NP** [2]	**LZSR-80P** [3]
Technology	Platiše-Flux	3-Flux-Gate	S-Flux-Gate	Closed-Hall
Turn Ratio	1000	600	1600	2026
Rated Primary Current I_p (A)	40	60	50	80
Linearity (ppm)	<200	20	1000	-
Voltage Out Gain Accuracy (%)	0.1	-	0.8	0.8
Voltage Out Gain Drift (ppm/K)	10	-	40	75
Total Worst Offset RTI (mA)	±27	±15	±140	±414
... without degauss and starting at $I_p \neq 0$	±90	-	-	-
Offset Drift RTI (uA/K)	50	150	<700	240
Step Response to 90% (us)	1	1	0.4	>3
Bandwidth at 0.5% I_p, −3 dB (kHz)	>800	800	300	200
Reaction time, 0 to 10% of I_p (μs)	0.1 @ 30 $\frac{\text{A}}{\mu\text{s}}$	-	0.3 @ 50 $\frac{\text{A}}{\mu\text{s}}$	1 @ 50 $\frac{\text{A}}{\mu\text{s}}$
Time Response, 0 to 90% of I_p (μs)	1.5 @ ≈15 $\frac{\text{A}}{\mu\text{s}}$	1 @ 25 $\frac{\text{A}}{\mu\text{s}}$	0.4 @ 50 $\frac{\text{A}}{\mu\text{s}}$	≈3 @ 50 $\frac{\text{A}}{\mu\text{s}}$
Noise RTI < 10 kHz (mArms) [4]	0.2	0.4	29	6
Noise RTI < 100 kHz (mArms) [4]	0.5	0.9	38	10
Noise RTI < 1 MHz (mArms) [4]	1.6	-	58	29
Power Min ... Max (W)	0.13 ... 0.33	2.4 ... 3.9	0.1 ... 0.24	0.1 ... 0.2

---

[1] LEM IT 60, `https://www.lem.com/sites/default/files/products_datasheets/it_60-s_ultrastab.pdf`; [2] LKSR, `https://www.lem.com/sites/default/files/products_datasheets/lksr_series.pdf`; [3] LZSR-80P, `https://www.lem.com/sites/default/files/products_datasheets/lzsr_80-p.pdf`; [4] the RMS noise of LEM products was calculated as peak-to-peak/6.6.

Chapter 6

Conclusion

In a single century, electricity has become essential to our lives and activities, and monitoring its use via the measuring of electrical current is now vital for the operation of various devices, systems, and processes. The development of current measurement principles and technologies has included a number of significant achievements. The first galvanometers were discovered by André-Marie Ampère and developed by Jacques-Arsène d'Arsonva in 1882. Shunts based on Georg Simon's Ohm Law from 1827 were initially used to extend the current range of galvanometers. AC transformers were invented in 1880-1884 by inventors Sebastian Ziani de Ferranti, Ottó Bláthy, Károly Zipernowsky, and Miksa Déri, followed by the Rogowski Coil in 1912 and the first Edwins Hall sensors in 1950. The magnetoresistance effect developed by Lord Kelvin in 1856 led to tunnel magnetoresistance by Julliere in 1975, and later in 2007, Albert Fert and Peter Grünberg discovered giant magnetoresistance. In 1936, Hans Aschenbrenner and Georg Goubau invented the fluxgate magnetometer, which led to the development of the most accurate and precise current sensors today. This was followed by the latest fiber optics current sensors. This dissertation describes a novel principle for isolated, precise, and accurate current measurements using a flux measurement sensor. It was invented in 2006 by Uroš Platiše and worldwide patent applications were granted in 2018-2021.

6.1 The Novelties: CCVR and PFS

This dissertation presents a novel type of active magnetic element embedded into the magnetic material that acts as a magnetic transistor, capable of modulating the passing-by magnetic flux by controlling the (external) electric current. Since the term magnetic transistor has already been used for a bipolar junction transistor with one or more magnetic regions [58], an alternative term Current Controlled Variable Reluctance (CCVR) has been introduced.

With an active element embedded inside a magnetic circuit, a flux redirection principle was applied, analogous to zero-drift operational amplifiers with a modulation/demodulation scheme that created a new type of flux sensor, the Platiše Flux Sensor (PFS) (named after the inventor), thoroughly described in Chapter 4.

Since the PFS is embedded into the magnetic core without the need for an air-gap, the core retains the original highest possible permeability, sensitivity, and immunity to external magnetic fields. Evaluated and thoroughly verified in a zero-flux closed-loop DC Current-Transducer (DC-CT), as described in Chapter 5, the innovation shows superior performance compared to other widely used DC current transducers based on different key principles, such as Hall, magnetoresistance, and single core fluxgate, approaching the performances known to the high-end fluxgate implementations. The performance results have been presented, tested on over 100 prototype samples, and verified in a representative testing environment.

6.2 Technology Readiness

The evaluation prototypes of PFS used in this dissertation were implemented by using soft ferrite magnetic materials of a relative permeability of only $\mu_r = 2200$. The lower permeability material was mechanically stronger and thus better suited to implement the innovation in a prototype series.

As the PFS element is relatively small, its energy consumption, including the electronics, is also relatively low, below 10 mW, making this technology suitable for lower power applications and applications in battery management systems where the low standby and quiescent currents are of particular importance. The size of the element and the energy consumption directly imply that the novel sensor does not produce a lot of noise to the primary and secondary windings, so it can operate at higher frequencies and provide a sensitivity over 100 mV/A.

The accuracy of the sensor depends on the gain linearity, long-term stability, and offset. The offset was identified as the key contributor to the overall accuracy, which mainly depends on the magnetic core material itself. Recalling Eq. (4.5), stating the worst case offset of a magnetic material without an air-gap is proportional to the coercitivity H_c and the effective length l_e. We have shown that the maximum offset of the prototype toroid core 40A9R using the 26G material by Iskra Feriti is about ±0.5 A. The degaussing techniques reduced the offset below 30 mA in the 40 A operational range, which equals 0.1% of the full-scale. Other performance parameters, such as linearity below 200 ppm, sensitivity of over 0.5 mA, bandwidth of over 800 kHz, very low noise of 0.5 mArms below 100 kHz, and 1.6 mArms up to MHz reach the performances of costly, higher power consumption, and much larger high-end fluxgate devices. In the scope of this development, a process was developed for small volume production and automated testing.

The latest research and developments have made significant progress with very high permeability and mechanically stronger materials, such as amorphous and nanocrystalline materials [59], [60] with relative permeability μ_r up to and over 100k, and H_c around 1 and below, reducing the worst case offsets by a factor of 10; with the degauss techniques, the offsets may be reduced below 10 mA. Especially due to this progress, the Platiše Flux Sensor technology becomes highly competitive and ready for mass market deployments in DC-CTs and low-cost implementations. Miniature implementations on a chip could use embedded ferromagnetic technology [61].

The last decade has seen significant progress in the semiconductors industry. Low-cost programmable analog and digital micro-controllers with increasing computing power and very low active power have enabled the prototyping and product industrialization of the concept that was initiated over a decade ago. The presented innovation with the state of the art materials and silicons enables compact and rigid DC current sensors that are also able to address harsh automotive environments and other critical application areas.

Even-though this dissertation was focused on the development of DC-CTs, the use of CCVR as an active element embodied into a magnetic material may find other uses and appear in different forms, as micro and nano-structures. For instance, it can be used to implement current controlled variable inductors. The PFS is a composition of the CCVR, a measuring winding and associated electronics circuitry. As such, it can be applied to any application that requires magnetic flux measurement inside a magnetic material structure without introducing an air-gap, i.e. potentially interesting for electric drives, valves, position sensors, or as general magnetic flux sensors. The CCVR as an active magnetic element and PFS as a sensing element thus represent the basic elements with which a complex magnetic circuits can be formed.

6.3 Designed for Emerging Applications

Emerging applications, such as renewable energy sources, electric vehicles, Industry 4.0, and the Internet of Things, use current sensors as part of a larger system. The analog signals are quantized using 16-24 bits analog to digital converters (ADC) at sample rates from 10 kSa/s (samples per second) and over 10 MSa/s.

In the scope of this dissertation, the requirements of modern data acquisition systems have been considered by providing DC accuracy in the 0.1% accuracy class, flat wide bandwidth AC response with good response times, and a low noise PFS closed loop system. To be suitable for integration in the emerging applications, the overall solution was designed to be as compact as possible, with low power consumption, very low quiescent/idle current consumption, and low cost.

Further research and developments are following these requirements in several directions. Recently, we have developed a high performance DC-CT with a measurement range of 1 kA and a peak range of 2 kA, linearity < 100 ppm, typical offset ±50 mA, with a core of outer diameter size of only 47 mm, which was integrated in a high performance data acquisition system (DAQ) with a sample rate of 15 MSa/s. Other lines of activities are focusing on lower power consumption, by employing D-class amplifiers, and digital networked sensors, by including DAQ and standard network interfaces, such as LAN with Time Sensitive Networking[1] (TSN) and Power over Ethernet (PoE), the latest Single Pair Ethernet (SPE) with Power over Data Lines[2] (PoDL), and industry standard network protocols, such as OPC/UA[3] and others.

6.4 The Future, Peer to Peer Energy

The existing legacy power grids have been designed to source energy from powerful centralized power plants and deliver it to large industrial consumers and numerous households, which at the end represent over 30% of total electric energy consumption. Recently, the power grids have been faced with the large amount of distributed renewable sources, whose generation is limited by grid sinking capabilities, and electrical cars. The latter consume between 15 and 20 kWh per 100 km, which is comparable to a typical daily household usage, which is around 10 kWh. These changes directly affect the power grids by the increasing energy demand and energy flows that are no longer unidirectional. Grids have not been designed for such bidirectional flows and because the future is about decentralized energy sources, we aim to make DC-CT technology to support true decentralized peer to peer energy provision, recently also approved by European energy directives [11].

Peer to peer energy could represent a major shift towards DC sub-kV systems between households, simplifying conversions, improving efficiency, and providing compatibility with electric vehicles whose batteries are also in sub-kV voltage ranges. This was impossible at the time the AC grid was being developed due to the lack of semiconductors and lower-cost DC metering technologies. Therefore, to achieve this, an inevitable element of such a system is an accurate and precise networked Direct Current Current Transducer.

---

[1] `http://1.ieee802.org/tsn`

[2] `https://standards.ieee.org/standard/802_3bu-2016.html`

[3] `http://opcfoundation.org`

Appendix A

ngSpice/Xspice Upgraded Code-Model: Core

Listing A.1 shows the excerpt from the file `src/xspice/icm/xtradev/core/cfunc.mod` which has been added to support the PLATISE soft-ferrite core model. The specification file `ifspec.ifs` has been altered to allow for the array of a single value for B and H, and option 3 has been added to the mode. Only the part that has been modified is shown in Listing A.2.

Listing A.1: cfunc.mod.

```
...

/* Retrieve mmf_input value. */
mmf_input = INPUT(mc);

/* Calculate H_input value from mmf_input... */
H_input = mmf_input / length;

    /* Platise model based on B_sat in B[0] and H_m in H[0]*/

if (size == 1 || mode == PLATISE) {
    double H2        = H_input*H_input;
    double Hm2       = H[0].rvalue*H[0].rvalue;
    double HHm2      = H2 + Hm2;
    double HHm2sqrt = sqrt( HHm2 );

    dout_din = B[0].rvalue * Hm2 * HHm2sqrt / (HHm2 * HHm2);
    B_out    = B[0].rvalue * H_input / HHm2sqrt;
}

    /* Determine segment boundaries within which H_input resides */

else if (H_input <= (H[1].rvalue + H[0].rvalue) / 2.0) {

...
```

Listing A.2: ifspec.ifs.

```

PARAMETER_TABLE:

Parameter_Name:     h_array                      b_array
Description:        "magnetic␣field␣array"       "flux␣density␣array"
Data_Type:          real                         real
Default_Value:      -                            -
Limits:             -                            -
Vector:               yes                          yes
Vector_Bounds:        [1 -]                        [1 -]
Null_Allowed:       no                           no


PARAMETER_TABLE:

Parameter_Name:     mode
Description:        "mode␣switch␣(1␣=␣pwl,␣2␣=␣hyst,␣3␣=␣platise␣(auto))"
Data_Type:          int
Default_Value:      1
Limits:             [1 3]
Vector:               no
Vector_Bounds:        -
Null_Allowed:       yes
```

Appendix B

Eagle ngSpice ULP Generated Netlists

The following Listings are automatically generated from the electric circuits in Chapters 4 and 5 by the *ngspice.ulp* user-language program, developed to support mixed domain simulation of analog, digital (verilog), embedded firmware, and more complex simulation circuits. See Chapter 3.5 for more information.

Listing B.1: Generated spice netlist from Figure 4.15.

```
* 40r9 Platise Flux Sensor on a Toroid Core

.param  Bs =0.361
.param  Hm =70
.param  l_dis =-0.2mm

.model seg26g core(H_array=[{Hm}] B_array=[{Bs}] area=2.2umm
+                  length=6mm)
A1A (3 10) seg26g

.model segb26g core(H_array=[{Hm}] B_array=[{Bs}] area=2.2umm
+                   length={6mm+l_dis})
A1B (3 9) segb26g
A2 (3 8) seg26g

.model ring26g core(H_array=[{Hm}] B_array=[{Bs}] area=6.2umm
+                   length=52mm)
A4 (6 5) ring26g
I1 lp1 lp2 DC 0.010
I2 ls1 ls2 PULSE(-5m 5m 0us 1.9us 1.9us 0.1us 4us)
R1 0 lp2 100Meg
R2 lp1 2 0.001
R3 13 lm1 0.1
R4 4 lm2 0.1
R5 lm2 lm1 1Meg
R6 0 lm2 100Meg
R7 16 ls1 0.1
R8 19 ls2 0.1
R9 0 ls2 100Meg
VC 6 0 0
VM 12 0 0
VSA 1 0 0
VSB 11 0 0

.include mmfcoil.mod
X1 2 lp2 3 5 mmfcoil N=1
X2 19 15 1 10 mmfcoil N=10
X3 13 4 8 12 mmfcoil N=10
X4 15 16 9 11 mmfcoil N=10
.end
```

Listing B.2: Generated spice netlist from Figure 4.20.

```
* 40r9 Platise Flux Sensor on a Toroid Core with Modulator/Demodulator

.param Bs =0.361
.param Hm =70
.param l_dis =-0.0mm

.model DT d_dt(gain=1 out_offset=0 out_lower_limit=-1
+ out_upper_limit=1 limit_range=1e-6)
A1 14 dm DT

.model seg26g core(H_array=[{Hm}] B_array=[{Bs}] area=2.2umm
+ length=6mm)
A1A (3 10) seg26g

.model segb26g core(H_array=[{Hm}] B_array=[{Bs}] area=2.2umm
+ length={6mm+l_dis})
A1B (3 9) segb26g
A2 (3 8) seg26g

.model MUL mult(out_gain=1 out_offset=0)
A3 [lm1 dm] vp MUL

.model ring26g core(H_array=[{Hm}] B_array=[{Bs}] area=6.2umm
+ length=52mm)
A4 (6 5) ring26g
A5 [7 7] 14 MUL
C1 vpf 0 1nF
IP lp1 lp2 PULSE( 0mA 10mA 50us 25us 25us 100us 250us )
IS ls1 7 PULSE(-5m 5m 0us 1.99us 1.99us 0.01us 4us)
R1 0 lp2 100Meg
R2 lp1 2 0.001
R3 13 lm1 0.1
R4 4 lm2 0.1
R5 lm2 lm1 1Meg
R6 0 lm2 1Meg
R7 16 ls1 0.1
R8 19 ls2 0.1
R9 0 ls2 1Meg
R10 7 ls2 10
R11 vp vpf 10k
VC 6 0 0
VM 12 0 0
VSA 1 0 0
VSB 11 0 0

.include mmfcoil.mod
X1 2 lp2 3 5 mmfcoil N=1
XLM 13 4 8 12 mmfcoil N=10
XLSA 19 15 1 10 mmfcoil N=10
XLSB 15 16 9 11 mmfcoil N=10

* Spice Control Directives from Sheet
.options savecurrents
.end
```

Listing B.3: Generated spice netlist from Figure 5.2.

```
* Complete DC-CT Control Loop

.model XFER s_xfer(in_offset=0 gain=1 num_coeff=[23 0]
+ den_coeff=[0.7 4623 7557143] int_ic=[0 0 0] denormalized_freq=1)
A1 7 lout XFER

.model INTFILT int(in_offset=0 gain=1 out_lower_limit=-10
+ out_upper_limit=10 limit_range=1e-6 out_ic=0)
A2 sout int INTFILT

.model INTSUM summer(in_offset=[0 0] in_gain=[377857 229]
+ out_gain=1 out_offset=0)
A3 [int sout] cout INTSUM

.model SLEW slew(rise_slope=2.5e9 fall_slope=2.5e9 )
A4 cout out SLEW

IP vlp1 3 PULSE( 0mA 1A 50us 25us 25us  100ms 200ms )
R1 0 4 1Meg
R2 5 out 0

.include 40r9.mod
XTR1 vlp1 4 lc 5 lm1 lm2 2 ls2 40r9
VC lc 0 0
VP 3 4 0
VP1 7 0 PULSE( 0mA 1A 50us 25us 25us  100ms 200ms )

.include trimod.mod
X1 lm1 lm2 2 ls2 sout 0 null 0 dcp5v trimod

* Auto Generated Sources
Vdcp5v dcp5v 0 DC +5V

.end
```

Listing B.4: Generated spice netlist from Figure 5.3.

```
.subckt 40r9 lp1 lp2 lc1 lc2 lm1 lm2 ls1 ls2 Bs=0.361 Hm=70 l_dis=-0.0mm

.model seg26g core(H_array=[{Hm}] B_array=[{Bs}] area=2.2umm
+ length=6mm)
A1A (3 10) seg26g

.model segb26g core(H_array=[{Hm}] B_array=[{Bs}] area=2.2umm
+ length={6mm+l_dis})
A1B (3 9) segb26g
A2 (3 8) seg26g

.model ring26g core(H_array=[{Hm}] B_array=[{Bs}] area=6.2umm
+ length=52mm)

A4 (6 5) ring26g
C1 lc1 lc2 0pF
R1 lp1 2 0.0001
R2 lp2 7 0.0001
R3 17 lc1 23
R4 13 lm1 0.1
R5 lc1 lc2 100Meg
R7 16 ls1 0.1
R8 19 ls2 0.1
R11 4 lm2 0.1
VC 6 gnd 0
VM 12 gnd 0
VSA 1 gnd 0
VSB 11 gnd 0

.include mmfcoil.mod
XLC 17 lc2 14 3 mmfcoil N=1000
XLM 13 4 8 12 mmfcoil N=10
XLSA 19 15 1 10 mmfcoil N=10
XLSB 15 16 9 11 mmfcoil N=10
XP 2 7 14 5 mmfcoil N=1

.ends
```

Listing B.5: Generated spice netlist from Figure 5.4.

```
.subckt trimod lm1 lm2 ls1 ls2 aout ref rok ref ref lm_dly=0us

.model DT d_dt(gain=1 out_offset=0 out_lower_limit=-1
+out_upper_limit=1 limit_range=1e-6)
A1 14 dm DT

.model MUL mult(out_gain=1 out_offset=0)
A3 [lm1 dm] vp MUL
A5 [7 7] 14 MUL
C1 aout gnd 1nF
IS ls1 2 PULSE(-5m 5m 0us 1.99us 1.99us 0.01us 4us)
IS1 gnd 7 PULSE(-5m 5m {lm_dly} 1.99us 1.99us 0.01us 4us)
R1 gnd 7 10
R5 lm2 lm1 1Meg
R6 gnd lm2 1Meg
R9 gnd ls2 1Meg
R10 2 ls2 10
R11 vp aout 10k

.ends
```

References

[1] P. Ripka, K. Draxler, and R. Styblikova, “Measurement of dc currents in the power grid by current transformer,” *IEEE Transactions on Magnetics*, vol. 49, no. 1, pp. 73–76, 2013.

[2] P. Ripka, K. Draxler, and R. Styblíková, “Dc-compensated current transformer,” *Sensors*, vol. 16, no. 1, p. 114, Jan. 2016, ISSN: 1424-8220. DOI: `10.3390/s16010114`. [Online]. Available: `http://dx.doi.org/10.3390/s16010114`.

[3] J. Turner and L. Austin, “A review of current sensor technologies and applications within automotive and traffic control systems.,” *Proc. Inst. Mech. Eng. Part D J. Automob. Eng.*, vol. 214, pp. 589–614, 2000. DOI: `10.1243/0954407001527475`.

[4] A. Patel and M. Ferdowsi, “Current sensing for automotive electronics—a survey,” *IEEE Transactions on Vehicular Technology*, vol. 58, no. 8, pp. 4108–4119, 2009. DOI: `10.1109/TVT.2009.2022081`.

[5] Y. Ouyang, J. He, J. Hu, and S. Wang, “A current sensor based on the giant magnetoresistance effect: Design and potential smart grid applications,” *Sensors*, vol. 12, no. 11, pp. 15 520–15 541, Nov. 2012, ISSN: 1424-8220. DOI: `10.3390/s121115520`. [Online]. Available: `http://dx.doi.org/10.3390/s121115520`.

[6] F. Zavoda and C. Yakymyshyn, “Sensors for smart grids: Smart grids technologies.,” in *In Proceedings of the 3rd International Conference on Smart Grids, Green Communications and IT Energy-Aware Technologies (ENERGY 2013)*, D. Petelin, A. Tavčar, and B. Kaluža, Eds., Lisbon, Portugal: Jožef Stefan International Postgraduate School, 2013.

[7] J. Qureshi, T. Lie, K. Gunawardane, N. Kularatna, and W. Qureshi, “Ac source vs dc source: Charging efficiency in battery storage systems for residential houses,” in *2017 IEEE Innovative Smart Grid Technologies - Asia (ISGT-Asia)*, 2017, pp. 1–6. DOI: `10.1109/ISGT-Asia.2017.8378378`.

[8] D. A. Aponte-Roa, G. D. G. Cabarcas, and W. W. Weaver, “Ac vs dc power efficiency comparison of a hybrid wind/solar microgrid,” in *2020 IEEE Conference on Technologies for Sustainability (SusTech)*, 2020, pp. 1–5. DOI: `10.1109/SusTech47890.2020.9150514`.

[9] A. Kirakosyan, E. F. El-Saadany, M. S. E. Moursi, A. H. Yazdavar, and A. Al-Durra, “Communication-free current sharing control strategy for dc microgrids and its application for ac/dc hybrid microgrids,” *IEEE Transactions on Power Systems*, vol. 35, no. 1, pp. 140–151, 2020.

[10] S. M. Lisy and M. Smrekar, “Three case studies of commercial deployment of 400v dc data and telecom centers in the emea region,” in *2015 IEEE International Telecommunications Energy Conference (INTELEC)*, 2015, pp. 1–6. DOI: `10.1109/INTLEC.2015.7572360`.

[11] H. van Soest, “Peer-to-peer electricity trading: A review of the legal context systems.,” *Competition and Regulation in Network Industries*, vol. 1–20, 2019. DOI: `10.1177/1783591719834902`.

[12] L. Atzori, A. Iera, and G. Morabito, “The internet of things: A survey.,” *Computer Networks*, no. 54, pp. 2787–2805, 2010.

[13] A. Caramizaru and A. Uihlein, “Energy communities: An overview of energy and social innovation,” *Joint Research Centre*, 2020. DOI: `10.2760/180576`.

[14] D. Management, “The bridge initiative and project fact sheets,” BRIDGE Horizont 2020, Tech. Rep., 2020. [Online]. Available: `https://www.h2020-bridge.eu/wp-content/uploads/2020/06/Brochure-of-BRIDGE-projects_2020_VF_web3.pdf`.

[15] D. Zhu, S. Chikkannanavar, and J. Tao, “Soc estimation error analysis for li ion batteries,” in *2021 IEEE Transportation Electrification Conference Expo (ITEC)*, 2021, pp. 479–483. DOI: `10.1109/ITEC51675.2021.9490137`.

[16] D. Tingting, L. Jun, Z. Fuquan, Y. Yi, and J. Qiqian, “Analysis on the influence of measurement error on state of charge estimation of lifepo4 power battery,” in *2011 International Conference on Materials for Renewable Energy Environment*, vol. 1, 2011, pp. 644–649. DOI: `10.1109/ICMREE.2011.5930893`.

[17] U. Platiše, “Device for the insulated measurement of current and a method for the insulated determination of current,” US9927464B2, JP6305419B2, MX342727B, CN104871014B, and India 336089; the applications in progress include EP2914967A1, WO2014067660A1, DE102012021364A1, and BR112015009522A2, 2018.

[18] G. Fernqvist, P. Dreesen, G. Hudson, and J. Pickering, “Characteristics of burden resistors for high-precision dc current transducers,” in *2007 IEEE Particle Accelerator Conference (PAC)*, 2007, pp. 317–319. DOI: `10.1109/PAC.2007.4440197`.

[19] “Current sensing power mosfets,” Onsemi, Tech. Rep. AND8093/D. [Online]. Available: `https://www.onsemi.com/pub/Collateral/AND8093-D.PDF`.

[20] “Components and methods for current measurement,” Vishay, Tech. Rep. 30304, p. 4. [Online]. Available: `https://www.vishay.com/docs/30304/currentmeasurement.pdf`.

[21] C. Bastos, “High precision current measurement for power converters,” *CERN Accelerator School: Power Converters, Baden, Switzerland, 7-14 May 2014*, 2016. DOI: `10.5170/CERN-2015-003.353`.

[22] B. V. Cordingley and D. J. Chamund, “Some observations on the performance of modern wideband current transformers in pulse current measurement applications,” 2001.

[23] N. Kondrath and M. K. Kazimierczuk, “Bandwidth of current transformers,” *IEEE Transactions on Instrumentation and Measurement*, vol. 58, no. 6, pp. 2008–2016, 2009. DOI: `10.1109/TIM.2008.2006134`.

[24] D. Slomovitz, L. Trigo, and C. Faverio, “Error compensation of capacitive effects in current transformers,” in *2012 Conference on Precision electromagnetic Measurements*, 2012, pp. 158–159. DOI: `10.1109/CPEM.2012.6250721`.

[25] L. Kojovic, R. Beresh, M. T. Bishop, R. Javora, B. Magruder, P. McLaren, B. Mugalian, and A. Offner, “Practical aspects of rogowski coil applications to relaying,” *IEEE PSRC Special Report*, 2010.

[26] Y. Xue, J. Lu, Z. Wang, L. M. Tolbert, B. J. Blalock, and F. Wang, "A compact planar rogowski coil current sensor for active current balancing of parallel-connected silicon carbide mosfets," in *2014 IEEE Energy Conversion Congress and Exposition (ECCE)*, 2014, pp. 4685–4690. DOI: `10.1109/ECCE.2014.6954042`.

[27] W. G. I-24, "Use of hall effect sensors for protection and monitoring applications," *IEEE Power Energy Society*, 2018.

[28] S. Lee, S. Hong, W. Park, W. Kim, J. Lee, K. Shin, C.-G. Kim, and D. Lee, "High accuracy open-type current sensor with a differential planar hall resistive sensor," *Sensors*, vol. 18, no. 7, p. 2231, Jul. 2018, ISSN: 1424-8220. DOI: `10.3390/s18072231`. [Online]. Available: `http://dx.doi.org/10.3390/s18072231`.

[29] "Hall effect sensing and application," Honeywell, Tech. Rep. [Online]. Available: `https://sensing.honeywell.com/hallbook.pdf`.

[30] "Isolated current and voltage transducers, characteristics - applications - calculations," LEM, Tech. Rep. [Online]. Available: `https://www.lem.com/images/stories/files/Products/1-3_applications/CH24101.pdf`.

[31] M. Chojowski, A. Dziadecki, M. Baszyński, R. Dudek, A. Stobiecki, and J. Skotniczny, "Wide bandwidth and inexpensive current sensor for power electronics—an augmented lem current sensor," *Energies*, vol. 14, no. 14, 2021, ISSN: 1996-1073. DOI: `10.3390/en14144194`. [Online]. Available: `https://www.mdpi.com/1996-1073/14/14/4194`.

[32] C. Reig and M.-D. Cubells-Beltrán, "Giant (gmr) and tunnel (tmr) magnetoresistance sensors: From phenomena to applications," *Magnetic Sensors and Devices: Technologies and Applications (1st ed.)*, Chapter 2, p35–59, 2017. DOI: `10.4324/9781315119595`.

[33] P. Ripka, "Review of fluxgate sensors," *Sensors and Actuators A: Physical*, vol. 33, no. 3, pp. 129–141, 1992. DOI: `10.1016/0924-4247(92)80159-Z`.

[34] H. C. Appelo, M. Groenenboom, and J. Lisser, "The zero-flux dc current transformer a high precision bipolar wide-band measuring device," *IEEE Transactions on Nuclear Science*, vol. 24, no. 3, pp. 1810–1811, 1977.

[35] C. Berriaud and A. Donati, "A device for measuring high current at cryogenic temperatures," *IEEE Transactions on Applied Superconductivity*, vol. 12, no. 1, pp. 1264–1268, 2002.

[36] "The basic principle of zero-flux," PM Special Measuring Systems B.V., Tech. Rep. [Online]. Available: `http://www.pm-sms.com/?page_id=12`.

[37] M. Harano, H. Yoda, K. Seki, K. Hayashi, T. Komiyama, and S. Yamada, "Development of a wideband high-precision current sensor for next generation power electronics applications," in *2018 IEEE Energy Conversion Congress and Exposition (ECCE)*, 2018, pp. 3565–3571. DOI: `10.1109/ECCE.2018.8557599`.

[38] S. Schoinas, A.-M. El Guamra, F. Moreillon, and P. Passeraub, "Fabrication and characterization of a flexible fluxgate sensor with pad-printed solenoid coils," *Sensors*, vol. 20, no. 8, p. 2275, Apr. 2020, ISSN: 1424-8220. DOI: `10.3390/s20082275`. [Online]. Available: `http://dx.doi.org/10.3390/s20082275`.

[39] D. Huang, S. Srinivasan, and J. E. Bowers, "Compact tb doped fiber optic current sensor with high sensitivity," *Opt. Express*, vol. 23, no. 23, pp. 29 993–29 999, Nov. 2015. DOI: `10.1364/OE.23.029993`. [Online]. Available: `http://www.osapublishing.org/oe/abstract.cfm?URI=oe-23-23-29993`.

[40] J. Zubia, L. Casado, G. Aldabaldetreku, A. Montero, E. Zubia, and G. Durana, "Design and development of a low-cost optical current sensor," *Sensors*, vol. 13, no. 10, pp. 13 584–13 595, 2013, ISSN: 1424-8220. [Online]. Available: `https://www.mdpi.com/1424-8220/13/10/13584`.

[41] K. H. Han, W. J. Lee, and B. Y. Kim, "Fiber-optic sensor array based on sagnac interferometer with stable phase bias," *IEEE Photonics Technology Letters*, vol. 13, no. 2, pp. 148–150, 2001. DOI: `10.1109/68.910517`.

[42] H. Cao, N. Shi, and J. Xu, "A novel design of fiber-optic sagnac current sensor," in *2012 Fifth International Symposium on Computational Intelligence and Design*, vol. 2, 2012, pp. 89–92. DOI: `10.1109/ISCID.2012.174`.

[43] R. Zakirov and A. Umarov, "Fiber optic gyroscope and accelerometer application in aircraft inertial system," in *2020 International Conference on Information Science and Communications Technologies (ICISCT)*, 2020, pp. 1–3. DOI: `10.1109/ICISCT50599.2020.9351385`.

[44] H. C. Beltran, J. L. Flores, J. A. Ferrari, G. García-Torales, and J. Cabrera, "Optical current sensor by self-compensating the Faraday effect," in *Infrared Remote Sensing and Instrumentation XIX*, M. Strojnik and G. Paez, Eds., International Society for Optics and Photonics, vol. 8154, SPIE, 2011, pp. 296–306. [Online]. Available: `https://doi.org/10.1117/12.894119`.

[45] S. Ziegler, R. C. Woodward, H. H. Iu, and L. J. Borle, "Current sensing techniques: A review," *IEEE Sensors Journal*, vol. 9, no. 4, pp. 354–376, 2009.

[46] D. Jiles and D. Atherton, "Theory of ferromagnetic hysteresis," *Journal of Magnetism and Magnetic Materials*, vol. 61, no. 1, pp. 48–60, 1986, ISSN: 0304-8853. DOI: `https://doi.org/10.1016/0304-8853(86)90066-1`. [Online]. Available: `https://www.sciencedirect.com/science/article/pii/0304885386900661`.

[47] ——, "Ferromagnetic hysteresis," *IEEE Transactions on Magnetics*, vol. 19, no. 5, pp. 2183–2185, 1983. DOI: `10.1109/TMAG.1983.1062594`.

[48] F. Liorzou, B. Phelps, and D. Atherton, "Macroscopic models of magnetization," *IEEE Transactions on Magnetics*, vol. 36, no. 2, pp. 418–428, 2000. DOI: `10.1109/20.825802`.

[49] J. Schliewe, S. Schefler, M. Koeppen, and S. Weber, "A frequency dependent magnetic material model based on the adapted jiles atherton model," in *PCIM Europe digital days 2020; International Exhibition and Conference for Power Electronics, Intelligent Motion, Renewable Energy and Energy Management*, 2020, pp. 1–8.

[50] F. Preisach, "Über die magnetische nachwirkung," *Zeitschrift für Physik*, vol. 94, no. 5-6, pp. 277–302, 1935.

[51] ——, "On the magnetic aftereffect," *IEEE Transactions on Magnetics*, vol. 53, no. 3, pp. 1–11, 2017. DOI: `10.1109/TMAG.2016.2548379`.

[52] Y. Bernard, E. Mendes, and F. Bouillault, "Dynamic hysteresis modeling based on preisach model," *IEEE Transactions on Magnetics*, vol. 38, no. 2, pp. 885–888, 2002. DOI: `10.1109/20.996228`.

[53] V. Chan, "Non-linear transformer model for circuit simulation," *IEEE Transactions on Computer Aided Design*, vol. 10, no. 4, pp. 476–482, 1991.

[54] M. Hodgdon, "Mathematical theory and calculations of magnetic hysteresis curves," *IEEE Transactions on Magnetics*, vol. 24, no. 6, pp. 3120–3122, 1988. DOI: `10.1109/20.92354`.

[55] ——, “Applications of a theory of ferromagnetic hysteresis,” *IEEE Transactions on Magnetics*, vol. 24, no. 1, pp. 218–221, 1988. DOI: `10.1109/20.43893`.

[56] G. Bao, X. Gao, R. Jiang, and K. Huang, “A novel differential high-frequency current transformer sensor for series arc fault detection,” *Sensors*, vol. 19, no. 17, p. 3649, Aug. 2019, ISSN: 1424-8220. DOI: `10.3390/s19173649`. [Online]. Available: `http://dx.doi.org/10.3390/s19173649`.

[57] R. Visintini, M. Cautero, C. Martins, G. Goransson, and M. Collins, “Power converters for the magnets of the linac warm units of ess,” in *IECON 2016 - 42nd Annual Conference of the IEEE Industrial Electronics Society*, 2016, pp. 3552–3557.

[58] J. Fabian, I. Zutic, and S. Das Sarma, “Theory of magnetic bipolar transistors,” Dec. 2002.

[59] G. Horia and V. Ionita, “Crystalline and amorphous soft magnetic materials and their applications - status of art and challenges,” *Journal of Optoelectronics and Advanced Materials*, vol. 4, Jun. 2002.

[60] G. Herzer, “Modern soft magnets: Amorphous and nanocrystalline materials,” *Acta Materialia*, vol. 61, no. 3, pp. 718–734, 2013, The Diamond Jubilee Issue, ISSN: 1359-6454. DOI: `https://doi.org/10.1016/j.actamat.2012.10.040`. [Online]. Available: `https://www.sciencedirect.com/science/article/pii/S1359645412007872`.

[61] J. Trites and K. Krone, “Embedded ferromagnetic technology,” in *Proceedings: Electrical Insulation Conference and Electrical Manufacturing and Coil Winding Conference*, 1997, pp. 665–672. DOI: `10.1109/EEIC.1997.651276`.

Bibliography

Publications Related to the Thesis

Journal Articles

U. Platiše, T. Kanalec, and M. Mohorčič, “High precision wide bandwidth dc current transducer based on the platiše flux sensor,” *Sensors*, vol. 20, no. 15, p. 4197, Jul. 2020, ISSN: 1424-8220. DOI: `10.3390/s20154197`. [Online]. Available: `http://dx.doi.org/10.3390/s20154197`.

Professional Articles

U. Platiše, “Introduction to open source spice mixed signal & verilog simulation,” *ISOTEL*, 2017. [Online]. Available: `https://www.isotel.org/mixedsim/intro/index.html`.

——, “Conceptual simulation of digital sine generator from eagle,” *ISOTEL*, 2017. [Online]. Available: `https://www.isotel.org/mixedsim/eagle/prssine/index.html`.

——, “The easiest way of simulating c/c++ code together with an analog & digital spice simulation,” *ISOTEL*, 2018. [Online]. Available: `https://www.isotel.org/mixedsim/embedded/motorforce/index.html`.

Patents

U. Platiše, “Device for the insulated measurement of current and a method for the insulated determination of current,” US9927464B2, JP6305419B2, MX342727B, CN104871014B, and India 336089; the applications in progress include EP2914967A1, WO2014067660A1, DE102012021364A1, and BR112015009522A2, 2018.

Trademarks

ISOTELpower d.o.o., “Dc-ct,” EUIPO 015057102, 2018.

Publications Related to the Technology

Journal Articles

U. Platiše and M. Mohorčič, “Sib : Sensor instrumentation bus for power and energy control units,” *Informacije MIDEM*, vol. 40, no. 1, pp. 53–59, 2010, ISSN: 0352-9045.

Conferences

R. Visintini, M. Cautero, C. Martins, G. Goransson, and M. Collins, “Power converters for the magnets of the linac warm units of ess,” in *IECON 2016 - 42nd Annual Conference of the IEEE Industrial Electronics Society*, 2016, pp. 3552–3557.

Products

ISOTELpower d.o.o., *Dc-ct official home page*, `http://dc-ct.com`, Accessed: 2020-09-31.

Dewesoft d.o.o., *Sirius xhs - high-speed data acquisition system*, `https://dewesoft.com/products/daq-systems/sirius-xhs`, Accessed: 2020-09-31.

Other Publications

Journal Articles

U. Platiše, U. Cvikl, and A. Žemva, “Efficient implementation of a three-channel ecg digital acquisition module,” *Informacije MIDEM*, vol. 35, no. 1, pp. 20–27, 2005, ISSN: 0352-9045.

Conferences

M. Mihelin, M. Smolnikar, M. Mohorčič, and U. Platiše, “Vsn - odprta platforma za brezžična senzorska omrežja,” in *19. mednarodna Elektrotehniška in računalniška konferenca ERK 2010*, 2010, pp. 269–272.

M. Smolej, B. Jeram, K. Kenda, I. Križnar, B. Lesjak, M. Perko, U. Platiše, and M. Pleško, “Accelerator control with the lonworks fieldbus,” in *7th International conference on accelerator and large experimental physics control systems (ICALEPCS/99)*, 1999, pp. 401–403.

H. Schieler, A. Weindl, B. Jeram, M. Juras, K. Kenda, I. Križnar, B. Lesjak, K. Mele, T. Milharčič, M. Perko, M. Peternel, U. Platiše, M. Pleško, M. Smolej, R. Sabjan, G. Tkacik, I. Verstovšek, B. Zorko, and K. Žagar, “First experiences with the control system for the accelerator of anka,” in *IEEE Particle Accelerator Conference 1999*, 1999, pp. 658–660.

M. Dach, S. Hunt, B. Jeram, M. Juras, K. Kenda, I. Križnar, B. Lesjak, K. Mele, T. Milharčič, M. Perko, M. Peternel, U. Platiše, M. Pleško, R. Sabjan, H. Schieler, M. Smolej, G. Tkacik, I. Verstovšek, B. Zorko, and K. Žagar, “A control system based on web, java, corba and fieldbus technolgies,” in *The Second International Workshop on Personal Computers and Particle Accelerator Controls (PCaPAC’99)*, 1999, p. 4.

K. Kenda, I. Križnar, M. Perko, U. Platiše, M. Pleško, and M. Smolej, “I/o control with pc and fieldbus,” in *The Second International Workshop on Personal Computers and Particle Accelerator Controls (PCaPAC’99)*, 1999, p. 4.

B. Jeram, M. Juras, K. Kenda, T. Milharčič, G. Mavrič, M. Peternel, U. Platiše, M. Pleško, R. Sabjan, M. Smolej, and G. Tkacik, "The control system for the accelerator of anka," in *Sixth European Particle Accelerator Conference (EPAC'98)*, 1998, pp. 1691–1693.

Biography

Uroš Platiše is a senior researcher and developer, innovator, and entrepreneur, founder of high-tech company ISOTEL and owner of the DC-CT brand. He has over 25 years of experience in mixed signal electronics and firmware research and development, mostly in the areas of data acquisition, digital control, sensors, and sensor network protocols.

He spent his childhood years in Kranj, Slovenia, at the time a center of high-tech and electronics industry of Yugoslavia, where he already enjoyed access to some of the most advanced companies and engineers in his early teens. Showing high interest and an eagerness to learn, he quickly adopted the latest state of the art technologies of programmable logic that were on the rise at the time. It was this background and knowledge that helped him become an absolute winner in electronics project competitions in Slovenia in consecutive years during his secondary technical school in electronics, SESŠ in Kranj. He continued with his formal education in electronics by attending a 5-year university study at the Faculty of Electrical Engineering, University in Ljubljana, where he obtained his Bachelor's degree in 2003, and enrolled in a PhD program at the Jožef Stefan International Postgraduate School in 2008.

Uroš Platiše's notable working experience started in 1997 with the ANKA synchrotron project at the Jožef Stefan Institute. Inspired by high-current sensing technologies, he triggered advanced research and development activities in the new direct current sensor technology already as early as in 2005 with Iskra Feriti. This was followed in 2015 by a collaboration with SiEVA and Kolektor, when DC-CT patent application was filed as well and subsequently granted in 2018. After the ANKA project, his research and development interest was also drawn to heterogeneous sensors, sensor networks, and control devices. The main activities of his research therefore continued in two main directions: sensors and power control, and autonomous distributed communication between these heterogeneous sensors and control devices. The first direction led to an innovation of a new type of a sensor for magnetic flux and high current measurements, while the second direction resulted in a new communication protocol stack supporting rapid hardware development as well as its deployment into IoT systems.

Other early works include an integrated resolver for hybrid permanent-magnet synchronous machines (PMSM), power inverters, the first open-source assembler (ava) and programmer (uisp) linux/windows support for the Atmel AVR micro-controllers, wireless ECG monitoring and sensing system in sport, HVAC drive control (Danfoss), reduced component-count PFC/LLC chip design (Infineon), designs and implementations of large scale FPGAs and CPLDs for telecommunication systems (Iskratel), an improved version of Wishbone specifications, and a high-speed zero-wait-state transaction bus. Recent projects include patented Smart Circuit Breaker (ISOTEL), and high-performance Data Acquisition (DAQ) systems (Dewesoft), and innovative modulation scheme for higher speed clock tolerant serial communications (ISOTEL). Research and development of mixed domain systems led to the creation of integrated open-source mixed domain simulation tools, also used extensively in this PhD dissertation and published openly on the Internet.